IECO

Volume 6 No 2 Year 2023

■ Volume 6

■ No 2

■ Year 2023

International Journal Of
Industrial Electronics Control and Optimization
IECO

University of Sistan and Baluchestan

Iranian Association of Electrical and Electronics Engineers

International Journal Of

Industrial Electronics Control and Optimization

In This Issue:

Research Artivles:

- Model Predictive Voltage Balance Control of Single-Phase Half-Bridge Active Front End Rectifier
  Mehran Safdari, Mohammad Reza Alizadeh Pahlavani, Arash Dehestani 81-88
- ptimization and Placement of DG Resources in the Network to Reduce Line Loading
  Farhad Zishan, Ehsan Akbari, Abdolreza Sheikholeslami, Nima Shafaghatian 89-100
- Fractional-Order Variable Struture Equations in Robust Control
  Ebrahim Abbaszadeh-Soorami, Mohammad Haddad-Zarif 101-113
- Synchronization Control Strategy of Inverted Pendulums using Control Law Partitioning and Contraction Theory
  Rogayyeh Soltani, Bashir Naderi, Saeed Nezhadhossein, Aghileh Heydari 113-122
- A Cascaded Multilevel Inverter Based on a New Basic Unit
  Roya Naderi, and Ebrahim Babaei 123-131
- Four-Switch Inverter-Based Hybrid Power Filter Optimized By Meta-Heuristic Algorithm of SPEA-II
  Poorya Rahmati-kahkha, Alireza Hosseinpour, Ahmad Khajeh 133-141
- Thermal Comfort-Based Heat Pumps Utilization for Wind Power Uncertainty Management
  Mohammadmehdi Sedaghatzadeh, Mohsen Gitizadeh, Saeed Hasanvand 143-159

International Journal Of
Industrial Electronics Control and Optimization
Print ISSN: 3517-2645
Online ISSN: 3568-2645
Homepage: https://ieco.usb.ac.ir/

About Journal

The University of Sistan and Baluchestan entered into strategic partnership with Iranian Association of Electrical and Electronic Engineers (IAEEE) to publish the **International Journal of Industrial Electronics Control and Optimization (IECO)**. The IECO is a refereed international journal which presents to the international scientific community important results of work in these fields, whether in the form of modeling simulation, analysis, fundamental research, development, application, design or real-time implementation. The scope of IECO is broad, encompassing all aspects of Industrial Electronics, Control and Optimization.

Note: International Journal of Industrial Electronics, Control and Optimization (IECO) has qualified to **ACADEMIC RESEARCH JOURNAL (ELMI-PAJOHESHI)** status certified by the ministry of Science, Research and Technology of Iran (No. 231566/3/18 dated 1396/10/09), and is published by the University of Sistan and Baluchestan through a formal partnership (No. 952/2/1500 dated 1395/11/04) with Iranian Association of Electrical and electronic Engineers (IAEEE) in order to develop scientific and research cooperation.

Aims and Scope

International Journal of Industrial Electronics, Control and Optimization (IECO) is a Peer reviewed journal of advanced and state-of-the-art in the science and engineering of Industrial Electronics, Control and Optimization. Its Scope encompasses the applications of Industrial Electronics, power systems, control, optimization and computational intelligence for the enhancement of industrial and manufacturing system and processes. The scope of the journal include the following:

I. Industrial Electronics

- Low and high-power converters
- Renewable energy
- Drive control techniques
- Techniques for advanced power semiconductor devices
- Power quality and utility applications
- Communications
- Flexible AC Transmission Systems (FACTS)
- Control in power electronics
- Electromagnetic and thermal performance of electronic power converters
- Motion control, robotics, sensors and actuators
- Fault detection and diagnosis
- Power systems
- Factory automation, communication, and computer networks

II. Control

- Adaptive control
- Control of process systems
- Control theory
- Data processing

- Design of control systems
- Hybrid systems
- Identification and observation
- Intelligent systems
- Model-predictive control
- Optimal control
- Robust control
- Fractional order systems

III. Optimization

- Ant Colony
- Chaos Theory
- Evolutionary Computing
- Fuzzy Computing
- Hybrid Methods
- Immunological Computing
- Neuro Computing
- Particle Swarm
- Probabilistic Computing
- Rough Sets
- Wavelet

International Journal Of
Industrial Electronics Control and Optimization
Print ISSN: 3517-2645
Online ISSN: 3568-2645
Homepage: https://ieco.usb.ac.ir/

Model Predictive Voltage Balance Control of Single-Phase Half-Bridge Active Front End Rectifier

Mehran Safdari[1] | Mohammad Reza Alizadeh Pahlavani[2] | Arash Dehestani Kolagar[2]

Department of Electrical Engineering, Ferdowsi University of Mashhad, Mashhad, Iran.[1]
Faculty of Electrical & Computer Engineering, Malek Ashtar University of Technology, Tehran, Iran.[2]
Corresponding author's email: mr_alizadehp@mut.ac.ir

Article Info

Article type:
Research Article

Article history:
Received: 2022-November-01
Received in revised form: 2023-March-04
Accepted: 2023-April-10
Published online: 2023-May-5

Keywords:
Active Front End (AFE),
Half-Bridge Boost Converter,
Model Predictive Control,
Single-Phase Rectifier.

ABSTRACT

Single-phase rectifiers are one of the most practical instruments with various applications. Among them, active front-end (AFE) rectifiers are introduced with bidirectional power transfer capability for power factor correction and the elimination of current harmonics. This paper proposes an adaptive model predictive control (MPC) for a single-phase AFE rectifier. The AFE topology used in this paper is a half-bridge boost converter. This topology has higher efficiency than other single-phase AFEs due to the fewer number of active semiconductor devices. Considering the presence of one leg of capacitors in this topology, balancing the voltages of these capacitors is a challenge, along with other control objectives. Also, this paper benefits from an MPC approach by which the switching signal for every switching state is chosen such that the defined cost function is minimized in the operation state to achieve all control goals based on the predefined model of the rectifier. Furthermore, an adaptive algorithm for the inductor current estimation is presented to robustify the control system against any unwanted disturbance in the control system. As a demonstration of the superior performance of the proposed method, a 1kW rectifier setup with 700Vdc output voltage fed from a 230Vrms/50Hz grid is built in the laboratory. The applicability of the MPC controller is verified and all operation waveforms of the test setup are presented. The proposed method offers a high-quality input current with total harmonic distortion (THD) below 5% and a high-power factor (PF) close to one. Also, the efficiency is comparable with the available commercialized rectifiers

I. Introduction

Switch-mode power supplies and rectifiers have high demand in various industrial applications and home appliances such as telecom power supplies, uninterruptible power supplies (UPSs), chargers, motor drive systems, and LED drivers. Diode and thyristor bridge-rectifiers are the simplest AC-DC circuits. But, these rectifiers suffer from many problems including a poor quality input current with high harmonic contents and a low power factor. Therefore, new rectifier circuits are proposed for reducing the grid current harmonic content and improving its quality, which are known as power factor correction (PFC) rectifiers. These rectifiers can be categorized into active and passive groups. The passive PFC rectifiers include boost PFC rectifiers and Vienna rectifiers, while the active type includes active front-end (AFE) rectifiers presented in [1]-[11].

The AFE rectifiers have a wide range of applications from low-power systems to high-voltage DC transmission systems and UPSs. Unlike diode rectifiers, AFE rectifiers offer bidirectional power flow with a high control capability and waveform quality. Therefore, these rectifiers are suitable to be employed for energy recovery braking systems, wind turbines, variable speed drives, and active power filters. Also, they are used in electrolysis, transportation, controlled power supplies, and many other appliances. However, regulating the output voltage of AFE rectifiers and their input current PFC need a multi-closed-loop control process, which complicates its implementation.

The predictive control method is widely used in power electronics due to its design simplicity, flexibility, and robust operation with various types of multi-variable and nonlinear systems. Besides, the high computational burden is no longer a negative point for implementing predictive control methods since powerful processors have been commercialized in recent years [12]. The main concept of predictive control methods is to use the present system state and its model for predicting the next state of the system. This data is used to follow the future behavior of the controlled variables in an optimized and predefined way. Predictive control methods are mainly known as deadbeat control, hysteresis-based, trajectory-based, and model predictive control (MPC) methods [13].

The deadbeat predictive control method is a model-based method that calculates the controlled variable such that the error of the reference value and the measured one become as close to zero as possible in each sampling period. This method has been successfully employed for inverters [14]-[16], rectifiers [17], active power filters [18], and PFC converters [19]. The basic concept of the hysteresis-based predictive control method is trying to maintain the controlled variables within the boundaries of a region or hysteresis space [20], while in the trajectory-based predictive control method, the controlled variable follows a predefined trajectory [21]. MPC is known as the most powerful method in which a cost function is defined and the controlled variables are calculated for optimizing the cost functions. The continuous control set MPC and finite control set MPC are the most well-known types in the literature. The main difference between these two types is in modeling, implementation, and complexity [22]-[25]. The main drawback of the MPC method is that its switching frequency is not fixed, which incurs higher switching losses compared to the deadbeat predictive control method, which uses a modulator with a constant frequency.

In this paper, a half-bridge boost AFE converter with one capacitors leg is used as the output voltage filter. This topology offers a high efficiency due to its fewer number of semiconductor devices. However, balancing the voltages of its output capacitors has always been a serious challenge. Two approaches have been discussed in the literature for balancing the voltages of the capacitors. The first method is to measure the unbalance of the capacitors' voltages and add it to the current reference as a DC value [26]-[29]. The main drawback of this method is that the PI controller coefficients need to be updated after every parameter change, e.g. load current, which leads to the unbalance of the capacitors' voltages. This means that for the sake of maintaining the fast dynamic performance of the converter, the PI controller should operate like an adaptive controller, resulting in a more complicated control process. The second approach is to replace the circuit topology with a full bridge converter, which is not desirable due to its higher power loss and cost with more switching devices [30]-[33].

This paper studies the performance and advantages of the predictive controller for balancing the voltages of the capacitors in a conventional converter, along with regulating its output voltage and maintaining an input current power factor close to one.

The paper is organized as follows. Section II describes the topology and its operating principles. Section III introduces the proposed controller, and Section IV presents the simulation and experimental results.

II. Selected Topology and Performance Analysis

Fig. 1 shows the topology. In this circuit, the grid current can only be controlled if the voltage of each of the output capacitors is higher than the grid peak voltage. Two possible states in Fig. 1 are shown in Fig. 2 and 3, where S1(S2) is ON(OFF) and S1(S2) is OFF(ON). In the following, the circuit equations are derived in each of the two so-called states, and the model is discretized by using the Forward-Euler method.

According to Fig. 2, the inductor voltage can be obtained by KVL in the loop including the input source and capacitor C1. Accordingly, one can write,

$$V_{L_S}(t) = V_S(t) - R_s i_{L_S}(t) - V_{C1}(t) \tag{1}$$

$$\frac{di_{L_S}(t)}{dt} = \frac{1}{L_s}(V_S(t) - R_S i_{L_S}(t) - V_{C1}(t)) \tag{2}$$

where V_{Ls} is the inductor voltage, V_S is the input source voltage, L_S is the input inductor, R_S is the equivalent series resistor (ESR) of the inductor, V_{C1} is the voltage of the capacitor C_1, and i_{Ls} is the input source current. According to the predictive controller nature, the continuous-time domain equations should be converted to the discrete-time domain. For this purpose, this paper uses the Forward-Euler method. Therefore, (2) is written as,

$$i_{L_s}(k+1) = \frac{\Delta t}{L_S}(V_S(k) - V_{C1}(k)) + i_{L_s}(k)(1 - \frac{R_s \Delta t}{L_S}) \quad (3)$$

where Δt is sampling period, k is the current sample, and (k+1) is the next sample. By using (3) and the input voltage, capacitor C_1 voltage, and input current in the k-th sampling period, the input current in the next sample can be derived. Also, the voltages of the output capacitors in the next sample can be obtained using the follwong equations.

$$V_{C1}(k+1) = \frac{\Delta t}{C} i_{L_s}(k) + V_{C1}(k) - \frac{\Delta t}{C \times R_{Load}}(V_{C1}(k) + V_{C2}(k)) \quad (4)$$

$$V_{C2}(k+1) = V_{C2}(k) - \frac{\Delta t}{C \times R_{Load}}(V_{C1}(k) + V_{C2}(k)) \quad (5)$$

where C=$C1$=$C2$, R_{Load} is the resistance of the load, and V_{C2} is the voltage of the capacitor C_2.

Following the same procedure for the circuit shown in Fig.3, (1)-(5) can be rewritten as follows,

$$V_{L_s}(t) = V_S(t) - R_s i_{L_s}(t) + V_{C2}(t) \quad (6)$$

$$\frac{di_{L_s}(t)}{dt} = \frac{1}{L_s}(V_S(t) - R_S i_{L_s}(t) + V_{C2}(t)) \quad (7)$$

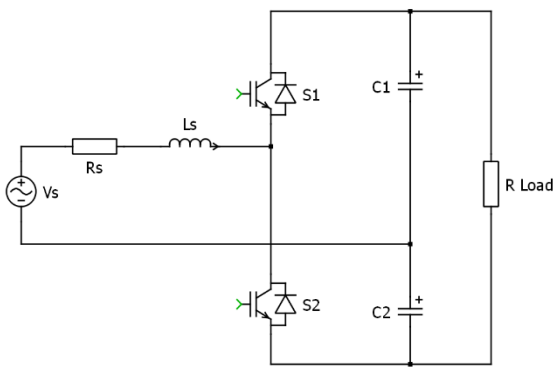

Fig. 1. Single-phase half-bridge AFE rectifier.

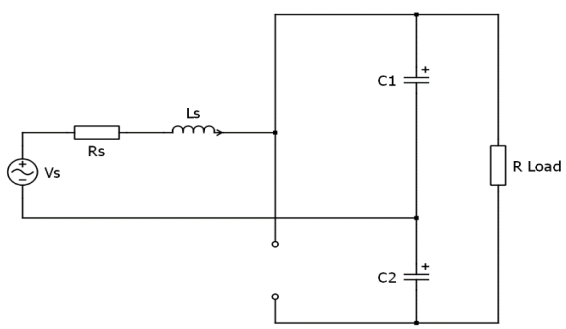

Fig. 2. Converter structure when S1 is on.

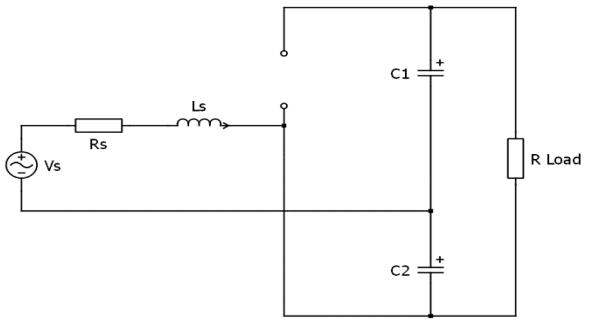

Fig. 3. Converter structure when S2 is on.

$$i_{L_s}(k+1) = \frac{\Delta t}{L_S}(V_S(k) + V_{C2}(k)) + i_{L_s}(k)(1 - \frac{R_s \Delta t}{L_S}) \quad (8)$$

$$V_{C1}(k+1) = V_{C1}(k) - \frac{\Delta t}{C \times R_{Load}}(V_{C1}(k) + V_{C2}(k)) \quad (9)$$

$$V_{C2}(k+1) = \frac{-\Delta t}{C} i_{L_s}(k) + V_{C2}(k) - \frac{\Delta t}{C \times R_{Load}}(V_{C1}(k) + V_{C2}(k)) \quad (10)$$

III. Proposed Control Algorithm

According to the discretized model of the converter and based on the MPC requirements, the predefined cost function is derived as,

$$g = \alpha \left| i_{L_s}(k+1) - i_{L_s}^{\mathrm{Ref}} \right|^2 + \beta \left| V_{C1}(k+1) - V_{C2}(k+1) \right|^2 \quad (11)$$

where g is the cost function, i_{Ls}^{Ref} is the input current reference, and α and β are the weight factors of the cost function. As is seen in the cost function, balancing the voltages of the capacitors is added as a penalty in addition to input current control. Moreover, the squared error is selected for each term of the cost function since (11) is a binomial cost function. Obviously, by appropriately selecting the weight factors, a tradeoff can be made between the control objectives.

Fig. 4 shows the proposed flowchart of the control algorithm. As shown, the input current reference is calculated by a PI controller with the measured values. Then, given that in each instance, one can decide which power switch should conduct. The input current and capacitors voltages are calculated for every possible switching operation, along with its corresponding cost function output. Finally, the power switch with the lower cost function output should conduct in the next instance.

IV. Simulation And Experimental Results

A. Simulation Result

To analyze the performance of the proposed method, the power and control stages are first simulated in PLECS with parameters given in Table I. Fig. 5 shows the steady-state input current and voltage of the converter. The input current harmonic spectrum is shown in Fig. 6 in comparison with the IEC61000-3-2 standard. According to Fig. 6, the total harmonic distortion (THD) of the input current is 2.7%. Also, the power factor is close to unity (Fig. 5). The output voltage of the converter and the voltages of the output capacitors are

also shown in Fig. 7. According to this fig., the output ripple is about 2%, and the voltages of the capacitors are balanced. It should be noted that balancing the voltages of the capacitors depends on the control method, load current, capacitance of the capacitors, etc. [26], [27], [30]. The output power changes are shown in Fig. 8 where the mean value of the power is 1kW.

In the second stage, the converter is constructed in the laboratory. The system parameters are listed in Table I.

B. Experimental Result

This paper used the MSOGI-FLL technique to detect the input voltage phase and derive its fundamental components (without distortion). Phase-locked loop (PLL) is a common method of voltage phase detection. The MSOGI-FLL technique is replaced with the conventional PLL for the following reasons:

- The control goals considered can be affected by uncontrollable factors such as input voltage distortion and harmonics;
- The delay in the conventional PLL causes moving away from control goals;
- MSOGI-FLL has faster and more accurate than the conventional PLL;
- MSOGI-FLL is an appropriate approach to getting the frequency and reference phase in power system frequency fluctuations and input voltage harmonics conditions.

Fig. 9 shows the MSOGI-FLL structure. According to this fig., by harmonic analysis of the input voltage and determining the desired harmonic number, MSOGI-FLL extracts this harmonic component in the output. In this paper, we considered fundamental, third, and fifth harmonic components in the MSOGI-FLL structure [34]-[36].

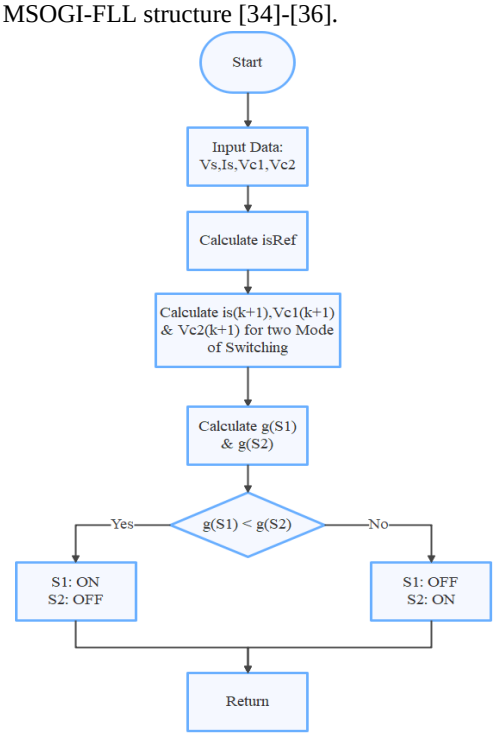

Fig. 4. The proposed flowchart of the control algorithm.

TABLE 1
SIMULATION AND EXPERIMENTAL PARAMETERS

Description	Values
Rated Power (P_o)	$1kW$
Input AC Voltage (V_S)	$220V_{rms}$
Frequency (f)	$50Hz$
Output DC Voltage (V_{DC}^{Ref})	$700V$
Capacitor (C_1, C_2)	$1200\mu F$
Input Inductor (L_S)	$8mH\ (ESR = 0.2\Omega)$
IGBT Switch (S_1, S_2)	FGL40N120AND
Sampling Time (Δt)	$25\mu S$
Microcontroller	STM32F407

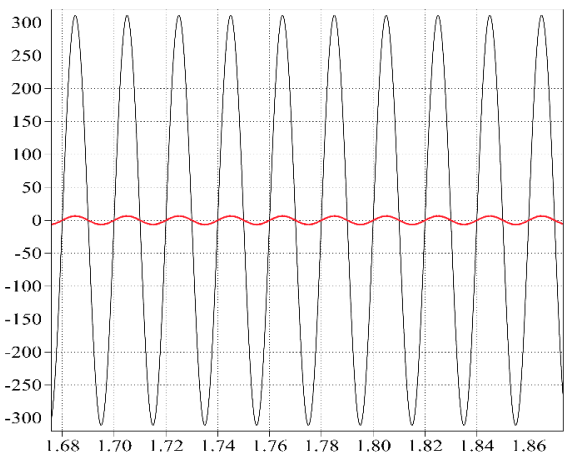

Fig. 5. Simulation results: input voltage (black) and input current (red).

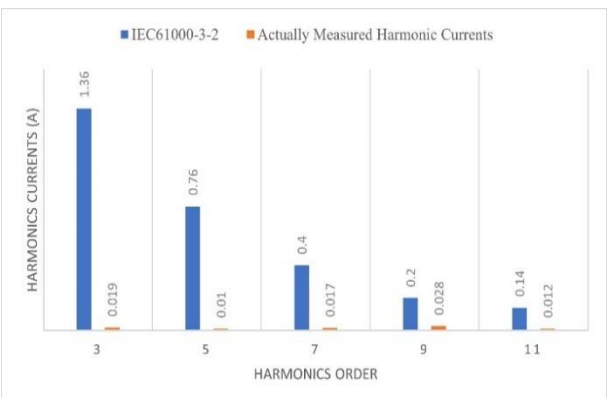

Fig. 6. Comparison between the converter input current harmonic spectrum with the standard spectrum.

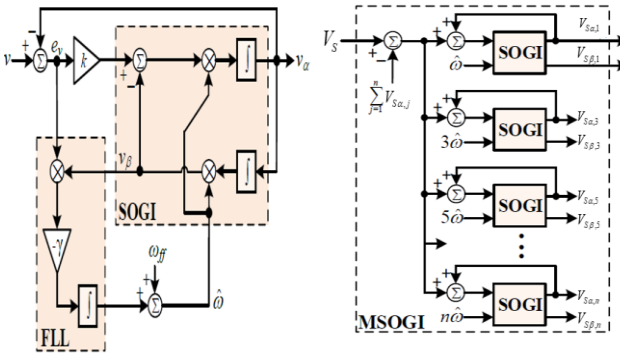

Fig. 9. MSOGI-FLL structure [34]-[36].

Fig. 10. Laboratory setup.

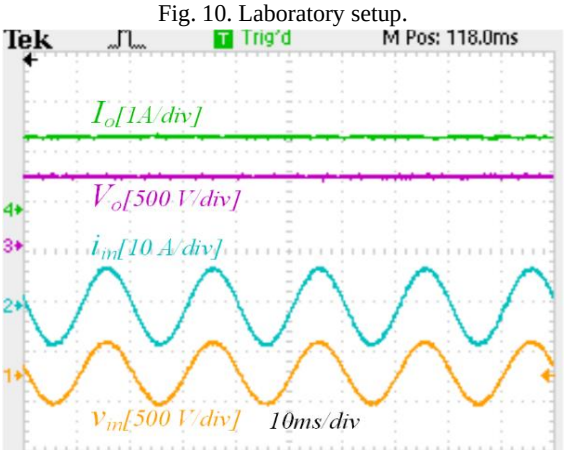

Fig. 11. Experimental results: CH1: input voltage (yellow), CH2: input current (cyan), CH3: output voltage (purple) and CH4: output current (green).

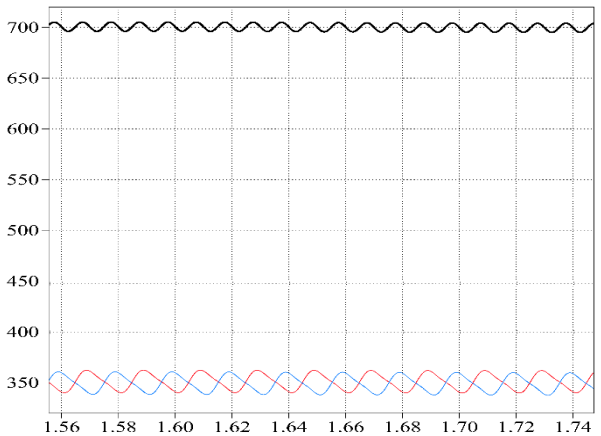

Fig. 7. Simulation results: output voltage (black), capacitor C1 voltage (blue) and capacitor C2 voltage (red).

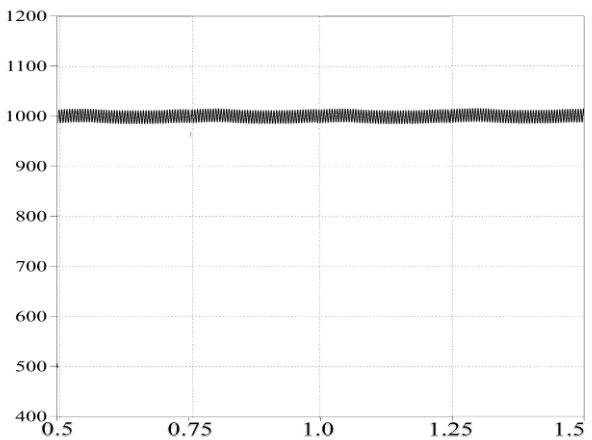

Fig. 8. Simulation results: output power.

To confirm the theoretical and simulation results, a laboratory setup of the proposed method is built, which is shown in Fig. 10. The setup parameters are listed in Table I.

The steady-state input voltage and current, and output voltage and current are shown in Fig. 11. As can be seen, the input current has a sinusoidal waveform with THD<5%, and the output voltage reaches its reference value with a voltage ripple lower than 2%. The steady-state output voltage with capacitors voltages is also shown in Fig. 12.

The capacitors voltages are balanced at the same DC voltage (350V), and the output voltage ripple is lower than 2%.

The steady-state output voltage, current, and power are shown in Fig. 13. According to this fig., the output power is 1kW with a very low ripple. Therefore, the successful performance of the proposed method is confirmed.

The THD and the PF of the proposed method are measured by using a FLUKE-435 power analyzer. The results show that THD is lower than the standard limits at nominal power. The power factor and THD at different output powers are also shown in Fig. 14 and 15. The power factor is almost always near unity.

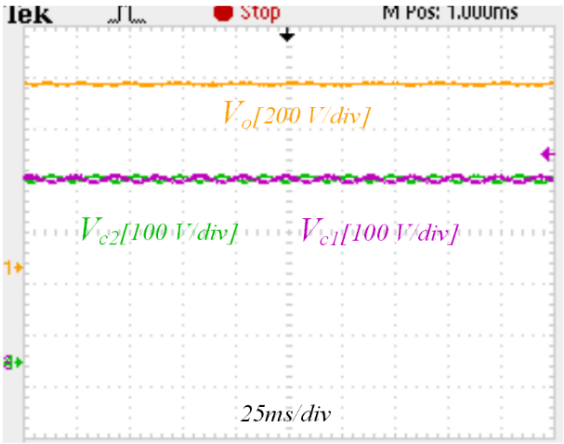

Fig. 12. Experimental results: CH1: output voltage (yellow), CH3: capacitor C1 voltage (purple) and CH4: capacitor C2 voltage (green).

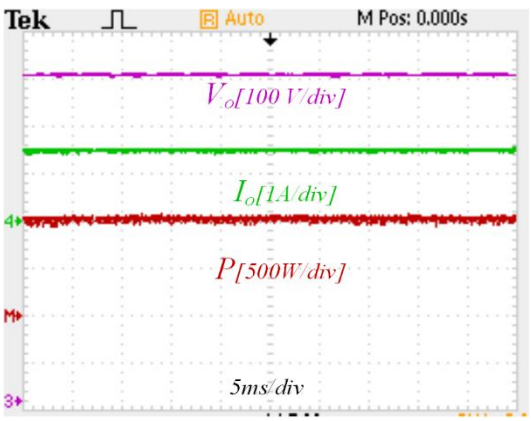

Fig. 13. Experimental results: CH3: output voltage (purple) and CH4: output current (green) and CH-M: output power (red).

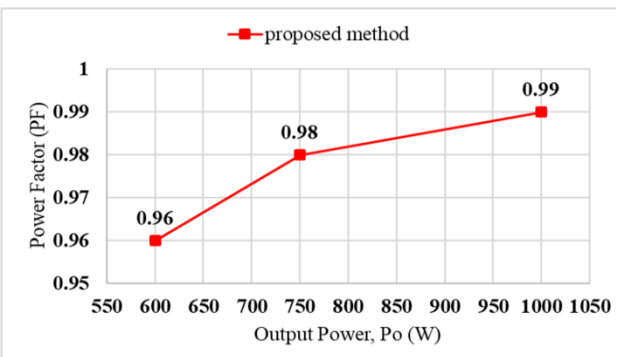

Fig. 14. Measured converter power factor at different output power.

Table II presents previous studies in which the controller structure has been modified to help achieve a balance in the voltage of the capacitors. As can be seen, some studies were limited to proving their results in the simulation environment. Considering the difference between the simulation results and experimental results, the studies with experimental results are more reliable. The output voltages of the works mentioned in Table II are not more than 530V. Meanwhile, the voltage unbalance of the capacitors will be higher at high voltages.

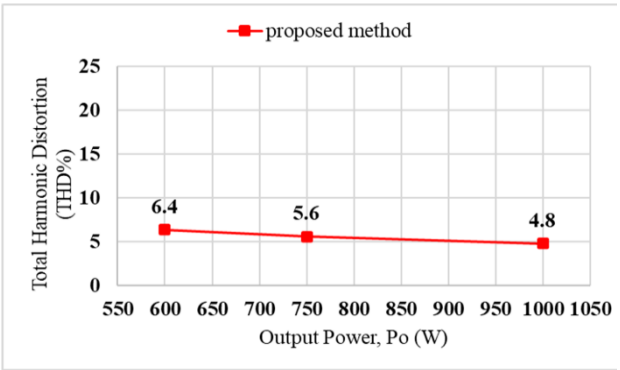

Fig. 15. Measured grid current THD at different output power.

As a result, the effectiveness of the methods used in past research for the high output voltage and output power of the converter is ambiguous. Also, according to Table II, references 6 and 7, which have considered a higher output power for the converter, used analog control to balance the voltage of the output capacitors. The experimental results of this paper show the effectiveness and appropriate performance of the controller in reducing input current THD and balancing output capacitors voltage in higher output voltage and power versus the previous works.

V.Conclusion

In this paper, a single-phase AFE rectifier with predictive control and output power of 1 kW was designed and built in order to verify the feasibility of the proposed control method. Simulation and laboratory results show that the predictive controller accurately balance the voltage across the capacitors while regulating the output voltage. Also, this method has the ability to maintain the high quality of the grid current in a wide range of load change.

Therefore, this method is a suitable alternative for previous solutions. The single-phase AFE circuit is a more advantageous topology than other well-known counterparts, especially in terms of cost and power loss.

References

[1] H. Y. Kanaan and K. Al-Haddad, “Boost Preregulators for Power Factor Correction in Single-Phase Rectifiers,” Power Electronics for Renewable Energy Systems, Transportation and Industrial Applications. pp. 503–533, 2014. ch16.

[2] B. N. Singh, B. N. Singh, A. Chandra, K. Al-Haddad, A. Pandey, and D. P. Kothari, “A review of single-phase improved power quality ac-dc converters,” IEEE Trans. Ind. Electron., vol. 50, no. 5, pp. 962–981, Oct. 2003.

[3] J. R. Rodriguez, J. W. Dixon, J. R. Espinoza, J. Pontt, and P. Lezana, “PWM regenerative rectifiers: state of the art,” IEEE Trans. Ind. Electron., vol. 52, no. 1, pp. 5–22, Feb. 2005.

[4] A. R. Prasad, P. D. Ziogas, and S. Manias, “An active power factor correction technique for three-phase diode rectifiers,” IEEE Trans. Power Electron., vol. 6, no. 1, pp. 83–92, Jan. 1991.

TABLE 2
COMPARISON BETWEEN THE PRESENT WORK WITH PREVIOUS RESEARCHES

Ref.	Controller	Vin (V)	Vout (V)	Pout (W)	THD (%)	Simulation / Experimental Result
[37]	Linear Control	120	450	80	2.5	EXPERIMENTAL
[28]	Hysteresis Current Control	90	300	300	1.7	EXPERIMENTAL
[23]	Hysteresis Current Control	100	260	130	N A	EXPERIMENTAL
[38]	PWM Average Model	70	150	375	13	SIMULATION
[29]	Dead Beat	170	400	80	2	SIMULATION
[39]	Analog Control	220	530	800	3.6	EXPERIMENTAL
[40]	Analog Control	150	400	1000	N.A	EXPERIMENTAL
Present Work	Model Predictive Control	220	700	1000	4	EXPERIMENTAL

[5] O. Stihi and Boon-Teck Ooi, "A single-phase controlled-current PWM rectifier," IEEE Trans. Power Electron., vol. 3, no. 4, pp. 453–459, Oct. 1988

[6] R. W. Erickson and D. Maksimovic, Fundamentals of Power Electronics. Boston, MA, USA: Springer, 2001.

[7] M. H. Rashid, Power Electronics Handbook. 2007.

[8] M. Monfard, M. Babaei and S. Sharifi, "A Z-Source Network Integrated Buck-Boost PFC Rectifier", International Journal of Industrial Electronics, Control and Optimization (IECO), Vol. 2, No. 4, pp. 289-296, Oct. 2019.

[9] M. Babaei and M. Monfared, "High Step-Down Bridgeless Sepic/Cuk Rectifiers With Improved Efficiency and Reduced Current Stress," IEEE Trans. Ind. Electron, Vol. 69, No. 10, pp. 9984-9991, Oct. 2022.

[10] M. Babaei, M. Monfared, S. Sharifi and H. Rezazadeh, "Z-Source Flyback PFC Rectifier for Energy Storage Systems", 2020 11th Power Electronics, Drive Systems and Technologies Conference (PEDSTC), Tehran, Iran, 2020, pp. 1-5.

[11] S. Sharifi, M. Babaei and M. Monfared, "A High Gain Buck PFC Synchronous Rectifier," Electrical Engineering (ICEE), Iranian Conference on Mashhad, Iran, 2018, pp. 1185-1190.

[12] C. R. D. Osorio, G. S. da Silva, J. C. Giacomini and C. Rech, "Comparative analysis of predictive current control techniques applied to single-phase grid-connected inverters," Brazilian Power Electronics Conference (COBEP), Jan. 2018.

[13] J. Rodriguez and P. Cortes, PREDICTIVE CONTROL OF POWER CONVERTERS AND ELECTRICAL DRIVES, Handbook, 2012.

[14] H.-T. Moon, H.-S. Kim, and M.-J. Youn, "A discrete-time predictive current control for PMSM," IEEE Trans. Power Electron., vol. 18, no. 1,pp. 464–472, Jan. 2003.

[15] G. Bode, P. C. Loh, M. J. Newman, and D. G. Holmes, "An improved robust predicitive current regulation algorithm," IEEE Trans. Ind. Appl. ,Vol. 41, No. 6, pp. 1720-1733, Nov. 2005.

[16] Q. Zeng and L. Chang, "An advanced SVPWM-based predictive current control of voltage source inverters," IEEE Trans. Ind. Electron. Vol. 55, No. 3, pp. 1235-1246, Mar. 2008.

[17] L. Malesani, P. Mattavelli and S. Buso, "Robust dead-beat current control for PWM rectifier and active filters," IEEE Trans. Ind. Appl., Vol. 35, No. 3, pp. 613-620, May/Jun. 1999.

[18] M. S. Karbasforooshan, M. Monfared, "An Improved Reference Current Generation and Digital Deadbeat Controller for Single-Phase Shunt Active Power Filters", IEEE Transactions on Power Delivery, Vol. 35, No. 6, Dec. 2020.

[19] P. Mattavelli, G. Spiazzi and P. Tenti, "Predictive digital control of power factor preregulators with input voltage estimation using disturbance observers," IEEE Trans. Power Electron., Vol. 20, No. 1, pp. 140-147, Jan. 2005.

[20] P. Cortes, M. P. Kazmierkowski, R. M. Kennel, D. E. Quevedo, J. Rodriguez, "Predictive Control in Power Electronics and Drives", IEEE Trans. Ind. Electron,, Vol. 55, No. 12, pp. 4312-4324, Dec. 2008.

[21] A. J. Sonawane, S. P. Gawande, S. G. Kadwane, M. R. Ramteke, "Nearly constant switching frequency hysteresis-based predictive control for distributed static compensator applications," IET Power Electronics, Vol. 9, No. 11, pp. 2174-2185, Sep. 2016.

[22] E. E. Espinosa, P. E. Melin, H. O. Garces, C. R. Baier, J. R. Espinoza, "Multicell AFE Rectifier Managed by Finite Control Set-Model Predictive Control", IEEE Access, Vol. 9, pp. 137782-137792, Oct. 2021.

[23] D. Park, M. Zadeh, "Modeling and Predictive Control of Shipboard Hybrid DC Power Systems", IEEE Transactions on Transportation Electrification, Vol. 7, No. 2, pp. 892-904, Jun. 2021.

[24] H. Radmanesh, M. Saeidi, "Linear Modelling of Six Pulse Rectifier and Designee of Model Predictive Controller with Stability Analysis", International Journal of Industrial Electronics, Control and Optimization (IECO), Vol. 3, No. 4, pp. 491-501, Sep. 2020.

[25] M. Ehsani, M. Saeidi, H. Radmanesh and A. Abrishamifar, "Comparisons between Generalized Predictive Control and Linear Controllers in Multi-Input DC-DC Boost Converter", International Journal of Industrial Electronics, Control and Optimization (IECO), Vol. 1, No. 3, pp. 27-34, Jan. 2020.

[26] Yu-Kang Lo, Sheng-Yuan OU and Shang-Chin YEN, "The Analysis and Elimination of Voltage Imbalance between the Split Capacitors in Half-Bridge Boost Rectifiers," IEEE Trans. Ind. Electron,, Vol. 49, No. 5, pp. 1175-1177, Oct. 2002.

[27] Ming-Fa Tsai, Kuo-Lung Chai and Ying-Yu Tzou, "CPLD Realization of a Digital Programmable PFC Control IC for Single-Phase Half-Bridge Boost AC-DC Converters," 35th Annual IEEE Power Electronics Specialists Conference, pp. 1134-1139, 2004.

[28] R. Srinivasan, R. Oruganti, "A Unity Power Factor Converter Using Half-Bridge Boost Topology", IEEE Transactions on Power Elec., Vol. 13, No. 3, May. 1998.

[29] Bayona, J.F., Guarnizo J.G., Gelvez, N., "Pulse width Prediction Control Technique Applied to a Half-Bridge Boost", TECCIENCIA, Vol. 13 No. 25, 47-54, Aug. 2018.

[30] Yu-Kang Lo, Chin-Tse Ho and Jian-Min Wang, "Elimination of the Output Voltage Imbalance in a Half-Bridge Boost Rectifier," IEEE Trans. Power Electron., Vol. 22, No. 4, July 2007.
[31] Wen-Long Ming, Qing-Chang Zhong, "Single-Phase Voltage-doubler with mismatched Capacitor for Balanced Output Voltages and Reduced DC-bus Voltage ripples", 2013 IEEE Energy Conversion Congress and Exposition, pp. 4830-4836, Sept. 2013.
[32] Sheng-Yuan Ou, Cheng-Yu Tang and Zih-Jian Chen, "Design and Implementation of a ZCS-PWM Half-Bridge Boost Rectifier with Output Voltage Balance Control", IEEE Trans. Ind. Electron. Vol. 59, No. 12, 2012.
[33] T. Hornik, Q. Zhong, "Parallel PI Voltage - H∞ Current Controller for the Neutral Point of a Three-Phase Inverter", IEEE Trans. Ind. Electron. Vol. 60, No. 4, 2013.
[34] S. Golestan, M. Monfared and J. M. Guerrero, "Second order generalized integrator based reference current generation method for sing-phase shunt active power filters under adverse grid conditions," in 4th Power Electron. Drive Syst. Technol. Conf. (PEDSTC), pp. 510-517, Feb. 2013.
[35] P. Rodriguez, A. Luna, I. Candela, R. Mujal, R. Teodorescu and F. Blaabjerg, " Multiresonant frequency-locked loop for grid synchronization of power converters under distorted grid conditions," IEEE Trans. Ind. Electron., Vol. 58, No. 1, pp. 127-138, Jan. 2011.
[36] P. Rodriguez, A. Luna, R. S. Munoz-Aguilar, I. Etxeberria-Otadui, R. Teodorescu, and F. Blaabjerg, "A stationary reference frame grid synchronization system for three-phase grid-connected power converters under adverse grid conditions," IEEE. Trans. Power. Electron., Vol. 27, No. 1, pp. 99-112, 2012.
[37] J. F. Bayona, H. R. Chamorro, A. C. Sanchez, J. A. Garcia and D. A. Rubio, "Linear Control of a Power Factor Correction Rectifier in Half-bridge Configuration", IEEE CACIDI – IEEE Conference on Computer Sciences, pp. 1-6, Dec. 2016.
[38] F. J. C. Padilha, M. D. Bellar, "Modeling and Control of the Half-Bridge Voltage-Doubler Boost Converter", 2003 IEEE International Symposium on Industrial Electronics, pp. 741-745, Mar. 2004.
[39] R. Ghosh, G. Narayanan, "A Simple Analog Controller for Single-Phase Half-Bridge Rectifier," IEEE Trans. On Power Elec., Vol. 22, No. 1, pp. 186-198, Jan. 2007.
[40] M. T. Tsai, C. F. Wang, Z. H. Yu, "Single-Phase Half-Bridge Rectifier with a Novel DC BUS Balance Controller," The 33rd Annual Conference of the IEEE Industrial Electronics Society (IECON), pp. 1956-1961, Nov. 2007.

Mehran Safdari was born in Mashhad, Iran, in 1993. He received B. Sc. Degree (with honors) from the Sadjad University of Technology, Mashhad, Iran in 2015 and M. Sc. Degree from the Ferdowsi University of Mashhad, Iran in 2019, respectively all in Electrical Power Engineering. Since 2015, he has been teaching at Sadjad University and Khayyam University. His research interests include micro-grid, optimization on power system, power system planning, power electronics, high power converters, power quality, active power filter, electrical machines.

M. R. Alizadeh Pahlavani was born in Iran in 1974. He received the B.Sc., M.Sc., Ph.D. degrees in Electrical Engineering from the Iran University of Science and Technology (IUST), Tehran, Iran, in 1998, 2002, and 2009, respectively. He is Professor of Malek Ashtar University of Technology, Tehran, Iran. He is the author of more than 400 journal and conference papers in field of electromagnetic systems, electrical machines, power electronic, FACTS devices, and pulsed power.

Arash Dehestani Kolagar was born in Babol, Iran, in 1983. He received B.Sc. degree from the University of Tehran in 2004, M.Sc. degree from the University of Isfahan, Iran in 2007, and Ph.D. degree from Iran University of Science and Technology in 2013, respectively all in Electrical Power Engineering. In 2014, he joined the Faculty of Electrical and Computer Engineering, Malek-Ashtar University of Technology, Tehran, Iran. His main areas of research interest are power electronics, high power converters, power quality, active power filter, DC and AC electric arc furnaces, and electromagnetic systems. (Malek-Ashtar University of Technology, Tehran, Iran, E-mail: a_dehestani@mut.ac.ir)

International Journal Of
Industrial Electronics Control and Optimization
Print ISSN: 3517-2645
Online ISSN: 3568-2645
Homepage: https://ieco.usb.ac.ir/

Optimization and Placement of DG Resources in the Network to Reduce Line Loading

Farhad Zishan[1] | Ehsan Akbari [2] | Abdolreza Sheikholeslami*[3] | Nima Shafaghatian [4]

Department of Electrical Engineering, Sahand University of Technology, Tabriz, Iran.[1]
Department of Electrical Engineering, Mazandaran University of Science andTechnology, Babol, Iran.[2]
Department of Electrical Engineering, Babol Noshirvani University of Technology, Babol, Iran.[3]
Electrical Engineering Department, Zanjan University, Zanjan, Iran.[4]
Corresponding author's email: asheiikh@nit.ac.ir

Article Info

Article type:
Research Article

Article history:
Received: 2023-April-27
Received in revised form: 2023-May-20
Accepted: 2023-June-06
Published online: 2023-june-24

Keywords:
Distributed Generations
Uncertainty of Resources
Optimization
PSO Algorithm
BSO Algorithm

ABSTRACT

Due to the high penetration coefficient of wind and solar energy in the grid and the uncertainty of these sources, we need a possible analysis. This paper contributes to the design, modeling, and planning a distributed generation (DG) network with wind and solar by means of the particle swarm algorithm (PSO) and backtracking search optimization (BSO) algorithm in the IEEE 33-bus network, aiming to minimize the results indicate an adequate performance in a variety of environments, and the presence of distributed wind/solar energy generators decreases network stress by feeding loads locally. These systems (wind and solar) can be used in remote areas without power networks, or even in areas where there is a tendency to use renewable energy despite the presence of a power network. They can also supply the output load for most of the day and night. Probability distribution functions are used, and the outputs are expressed as probability density distribution functions instead of absolute numbers. In addition, there is a high degree of uncertainty regarding the state of the system, which is an associated renewable energy source within the power system elements. By means of the MATLAB software, the proposed method is implemented in order to ensure effectiveness and validate the results**.** Finally, the superiority of the BSO algorithm over PSO will be seen.

NOMENCLATURE

Wind velocity	V_W	Ideality factor of a diode	n
Blade radius	R	Nominal thermal voltage of a cell	v
Blade angle	β	Beta distribution factors	$\alpha_\beta , \beta_\beta$
Air density	ρ	Sunlight intensity	R_C
Turbine power factor	C_P	Gamma function	Γ
Wind velocity scale parameter	K_t	Mean and standard deviation	μ_s^t and δ_s^t
Formation parameter	C_t	Open circuit voltage	Voc
Series resistance	R_S	Short circuit current	Isc
Parallel resistance	R_{SH}	Ambient temperature	Tc
Wind turbine output power	Pw	Weight function	w
Radiation-induced current	I_L	Resistance and reactance of airline feeder	X and R
Diode current	I_O	Active and reactive power	Q and P
Boltzmann constant	k		
Electric charge of an electron	q		

I. Introduction

To date, the issues of optimal operation with the presence of renewable resources and optimizing the production of these resources have become very relevant. Wind and solar power plants are among the most attractive opportunities for investors. The consolidation of a significant amount of power from renewable sources such as the wind and the sun in distribution networks poses significant operational challenges due to the degree of uncertainty involved [1-4]. In order to meet the increasing electricity demand, the most important task of energy distribution companies is to plan the development of sustainable power distribution networks [5-8]. The main goal of distribution network expansion planning is to provide consumers with an acceptable and affordable service [9] while keeping voltage levels and power quality within acceptable limits. In addition, the purpose of a distribution network is to provide power to customers and respond rapidly to changes in their demands. In this vein, it becomes necessary to assess the state of sustainable energy generation with regard to wind and solar (photovoltaic, PV) systems [10-14] in terms of transmission, distribution, and consumption conditions. A distribution network does not have a power plant, but it does have transmission lines that deliver electricity to it. Large power plants create electricity, which is then supplied to distribution networks through transmission lines. Given the urge to minimize coal/gas power plants and the increasing consumption of electricity, there is a need for new generation resources [15-19]. However, the privatization of the power industry has changed the status of power plants from regulative to competitive. The advent of small power plant technologies (clean generation and higher-efficiency power plants) has aided in meeting the current energy demands [20-22]. The conditions of energy markets and geographical conditions completely dictate investors' choices with regard to power plants [23, 24].

Many sectors of distribution networks are nowadays crowded due to the intervention various small scale renewable energy and coal/gas power plants. This, while investment in the generation sector declines [25] and the energy demand rises, as well as the price of electricity, particularly in western Asia, in countries such as in Iran [26]. The goal of the electrical sector is to provide residents and companies with clean, safe, and dependable energy, so it is critical to invest in new technologies that enhance current power systems and usher in a revolution in this industry [27-31]. This will not be possible unless the structure of the distribution network and its control system are fundamentally changed. One solution is the use of distributed generation (DG) resources [32-33]. In recent years, the utilization of DG resources in networks has contributed to improving effectiveness and reliability. Most classical point-to-point methods (e.g., direct methods and derivation-based methods) use computational techniques to arrive at the optimal solution [34]. However, as the problem size and search space increase, finding the solution via classical methods becomes more complicated. Computational intelligence optimization algorithms have been used in various fields, including science, business, and engineering, to solve complex optimization problems. This is due to their ease of use, wide execution capability, and overview. The most popular method is particle swarm optimization (PSO) [35, 36]. PSO is better in terms of solution quality and number of iterations, namely regarding the initial random population, particle upgrades, and the generation of new solutions. However, these methods of collective intelligence are limited by premature convergence and because they are often trapped in local minima. To overcome these issues, these algorithms have undergone different variations, aiming to improve their performance [37]. These methods' principles of operation are inspired by natural genetic evolution, which why they are the most famous example of a genetic algorithm.

In [38], the effect of influence of distributed generation with different technologies on annual energy losses is calculated. This includes combined cycles, wind energy, and photovoltaic and solar cells. It is shown that wind energy has the worst behavior with respect to reducing losses, and it is concluded that distributed generation units with reactive power control capabilities have a greater effect on improving the voltage profile and reducing losses in the network. The authors of [39] combine genetic algorithms and particle aggregation to optimize the size and location of scattered products.

In [40], an algorithm for determining the optimal location and size of DGs in distribution networks is introduced. This algorithm is based on a new index that examines the effects of energy sources. The work by [41] offers a way to optimally locate different DG technologies in order to reduce energy losses. Voltage limits, line load capacity, the maximum influence of DG, and steps to increase or decrease DG capacity are among the constraints of the problem. The authors of [42] propose an analytical method for minimizing system losses, which involves installing different types of DGs. To this effect, in addition to the resource capacity, the optimal power factor for the four types of distributed generation resources is determined in order to obtain the greatest reduction in losses. Thereupon, this method studies the types of DGs that can generate or absorb reactive power.

The authors of [43] present a probabilistic method to analyze the steady-state operating conditions of a distribution system with wind and photovoltaic power plants. This method is based on the uncertainty of power system loads and power generation from renewable systems, as well as on a combination of Monte Carlo simulation techniques and linear equations. In [44], the load distribution of a power system is analyzed using a new point estimation method while considering the system's uncertainty, which may arise from a variety of sources such as load or downtime. A new algorithm for the longitudinal differential protection of transmission lines

is described in [45], and the imperialist competitive algorithm is employed in [46] for determining the location and size of optimal multiple DGs in a distribution network. In [47], an optimal controlled strategy for multiple distributed generations in a micro grid island is presented. Below are some relevant applications of wind and solar systems in distribution networks [48]:

1. Increasing the average annual growth rate of energy consumption in the country and reducing oil exports
2. Expanding the influence of renewable energy on the energy supply
3. Introducing these technologies into the global energy supply market
4. Backing up the power supply in order to provide power to sensitive loads such as special industrial units during network power outages, as well as improving reliability
5. Reducing the costs associated with the power supply, which can be very expensive in remote areas or due to geographical obstacles
6. Providing the power required by the load during peak hours
7. Providing part of the power required by the base load
8. Reducing environmental pollution

The aforementioned solutions have limited control capabilities due to the lack of a communication infrastructure. Loading transmission lines with distributed generation sources is a common topic of discussion. This paper addresses their placement within the power system to reduce losses and keep the transmission lines free.

The aim of this research is to minimize the density of transmission lines and coordination in systems that integrate DG energy sources and wind and solar energy. The placement of these resources is studied using the PSO algorithm in an IEEE 33-bus network. This article first introduces wind and solar sources, and it delves into losses in networks with DGs. Then, the coordination of these sources and the use of the PSO and BSO algorithm for locating and reducing line loading are discussed. Finally, the results are reviewed and analyzed. Among the most important works of this article:

Results of losses with wind sources
Results of losses with solar sources
Results of losses with hybrid sources
Load rate of lines in optimal condition with wind resources
Load rate of lines in optimal condition with solar resources
Load rate of lines in optimal condition with wind and solar resources
Locating resources with PSO and BSO

II. Research Methodology

A. Wind turbine performance

A wind turbine first converts wind energy into mechanical energy, which is in turn converted into electrical energy by a generator. The active power output from the wind turbine and the input to the generator only depend on changes in the generator's optimum speed. Thus, the output power may be regulated by adjusting the generator's speed. The relation of wind power can be expressed as shown in Equation (1) [18].

$$P_W = \frac{1}{2}\rho\pi R^2 V w^3 C_P(\lambda, B). \quad (1)$$

Figure 1 show a diagram and power area in terms of wind turbine speed. Wind turbines start moving at cut in velocity and generate electricity up to cut out velocity. Where V_W is the wind speed, R is the blade radius, β is the blade angle, ρ is the air density, and C_P is the turbine power factor, which is a function of λ and β Figure 1 shows the power-speed curve of the wind turbine. Wind turbines start moving at a cut-in velocity and generate electricity up to a cut-out velocity. The type of wind turbine considered in this study is DFIG. Wind velocity is modeled with a Weibull distribution. The Weibull function is a specific state of the gamma distribution which is more flexible than other functions. Moreover, different time frames can be used for long-term measurements. Wind velocity can be characterized by its mode and by random events. The implemented Weibull distribution function is shown in Equation (2) [49]:

$$f(v) = \frac{Kt}{Ct}\left(\frac{V}{Ct}\right)^{Kt-1} * \exp\left[-\left(\frac{v}{Ct}\right)\right]^2 \quad (2)$$

Where Kw is the Weibull wind speed scale parameter, Cw is the Weibull wind speed formation parameter, and V is the wind speed. The turbine output capacity can be determined according to Equation (3) [50-54]:

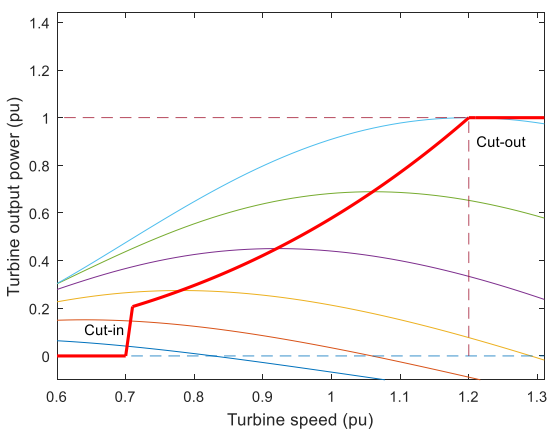

Fig. 1. Wind turbine performance in different areas

$$P_{WTG} = \begin{cases} 0 & \text{if} \quad v < Vi \text{ or } v > V0 \\ P_{rw}\frac{V-Vi}{Vr-Vi} & \text{if} \quad Vi < v < Vr \\ P_{rW} & \text{if} \quad Vr < v < Vo \end{cases} \qquad (3)$$

Where $Vi, Vo, and\ Vr$ are the starting speed (cut-in velocity), the cut-off speed (cut-out velocity), and the nominal velocity of the turbine, respectively. Note that v represents the wind velocity.

B. *Photovoltaic Cell Modeling*

Solar energy is converted into electrical energy by photovoltaic panels and converters. Photovoltaic technology uses semiconductor cells made up of diodes. By radiating light on the cell, voltage and current are produced. The cells combine to form a module that can be modeled as a current source parallel to a diode, as shown in Figure 2. Using the relationships of the solar cell, a general relation can be given, as shown in Equation (4):

$$I = I_L - I_O\left(E^{\frac{q(V+I.Rs)}{nkT}} - 1\right) - \frac{V+I.Rs}{R_{SH}} \qquad (4)$$

In this equivalent circuit, RS and RSH are series and parallel resistors, IL is the radiation current, IO is the diode current, k is the Boltzmann constant parameter, q is the electric charge of one electron, T is the cell temperature, n is the ideal coefficient of the diode, and v is the nominal thermal voltage of the cell. Solar radiation is modeled as a distribution function based on the model presented in [20]. The probability distribution function can show the probable state of the solar radiation phenomenon. Solar radiation has a high degree of uncertainty and changes as a function of several factors such as climate, time, day, month, season, and the orientation of solar cell generators (P_SCG). Sunlight is modeled with the beta distribution function, as shown in Equation (5) [20]:

$$f(R: \alpha_\beta, \beta_\beta) = \frac{\Gamma(\alpha_\beta + \beta_\beta)}{\Gamma(\alpha_\beta)\,\Gamma(\beta_\beta)} R^{\alpha_\beta - 1}(1-R)^{\beta_\beta} \qquad (5)$$

Here, α_(β) and β_(β)are beta distribution factors, and $PSCG$ is the output power is related to solar radiation, which is shown in Equation (6):

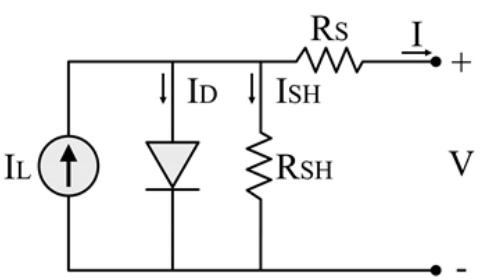

Fig. 2. Circuit equivalent to a solar cell

$$P_{SCG} = \begin{cases} P_{rs} & \text{if } v \le R < R_C \\ P_{rs}\frac{R}{R_{STD}R_C} & \text{if } RC \le R < RSTD \\ P_{rs} & \text{if } R_{STD} \le R \end{cases} \qquad (6)$$

RSTD is the radiation intensity under standard conditions (usually 150W/m2), P_rs (usually 1000 W/m2) is the output power of a solar cell, and $PSCG$ is the total output power.

C. *Modeling network losses*

Determine the number of changes in distribution network losses when DG re-sources are integrated, the load distribution of the network must first be calculated. The purpose determining the load distribution in this context is to analyze the voltage quality at each connection point. The increase in voltage due to the presence of the generator is obtained with Equation (7):

$$\Delta v = \frac{PR+QX}{V} \qquad (7)$$

For low-voltage networks, the effect of the resistance is greater than that of the reactance. Therefore, active power is more effective than reactive power in the network. For control purposes, the powers in the network are continuously measured. Implementing a power measurement period and running simulations can be an effective way to minimize losses. Figure 3 shows a part of the distribution feeder and power distribution path. The generators provide active power, but their reactive power capabilities are not used.

The reactive power at bus 1 (a load-bearing bus) can be obtained from Equation (8):

$$Q_{1j} = Q_{2j} + Q_{L1} \qquad (8)$$

In this equation, if the reactive power of generator G1 is equal to Q1j, equal to the sum of Q2j and QL1 according to the node law. The same procedure applies to other buses. To achieve optimal loss reduction [21], most operators cannot get the reactive power of DG resources.

A. *Resources Uncertainty*

There are several uncertainties throughout the distribution network, including changes in network load and the accidental output of power equipment. With the use of renewable energy sources, which have a variable nature, the uncertainty of power systems has increased even more. This poses many challenges with regard to the design and planning of these systems. Analytical load distribution can help to calculate the voltage of the nodes and the power of the branches under certain defined conditions, but it is not able to consider the uncertainty of the network parameters. Because wind and solar power are completely random and probabilistic, the amount of electrical power they generate during the day or night is completely variable. The optimal location of solar and wind resources in a distribution

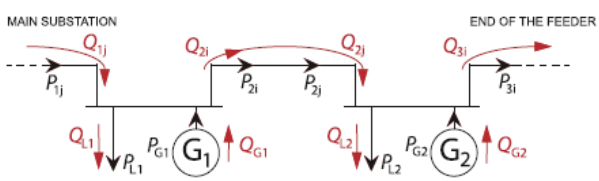

Fig. 3. Example of power distribution [21]

network is obtained by considering seasonal loads and changes in weather conditions, such as the solar radiation level and wind velocity. De-spite the uncertainty, the beta distribution for solar resources can be expressed as shown in Equation (9) [53-55]:

$$\begin{cases} f_s^t(s) = \frac{\Gamma(a^t+B^t)}{\Gamma(a^t).\tau(B^t)} * (s^t)^{a^t-1} * (1-s^t)^{B^{t-1}} \\ \text{for } a^t > 0 \quad , B^t > 0 \end{cases} \quad (9)$$

Where Γ represents the gamma function, a and B is parametric quantities, $f_s^t(s)$ i is the radiation intensity, and δ_s^t and μ_s^t are the mean and standard deviation, respectively. The wind distribution formulation is as follows:

$$\begin{cases} f_v^t(v) = \frac{k^t}{c^t} * \left(\frac{v^t}{c^t}\right)^{k^{t-1}} \\ \exp * \left(\frac{v^t}{c^t}\right)^{k^{t-1}} \quad \text{for } c^t > 0 \, , k^t > 0 \, , k^t > 0 \end{cases} \quad (10)$$

Where k^t , wind velocity scale parameter, and c^t is the formation parameter. These are calculated according to Equations (11). Generation capacity of the solar system is calculated, as according to Eq (12).

$$k^t = \left(\frac{\delta^t}{\mu_v^t}\right)^{-1.086} , c^t = \frac{\mu_v^t}{\Gamma(1+\frac{1}{k^t})} \quad (11)$$

$$P^t_{PV=\sum_{g=1}^{Ns} PG_{PV} * P_S(s_g^t)} \quad (12)$$

This equation is used to distribute the wind velocity and radiation level throughout the day and night by considering the variable daily load consumption and, as a result, the potential power generated by the solar cell or wind turbine. This is done by integrating the potential density function. Thus, ⟦PG⟧ _PV and P_(S) are calculated, as shown in Equation (13).

$$P_S(s_g^t) = \begin{cases} \int_0^{s_g^t + s_{g+1}^t)/2} f_s^t(s)ds & \text{for } g = 1 \\ \int_{s_{g-1}^t + s_g^t)/2}^{s_g^t + s_{g+1}^t)/2} f_s^t(s)ds & \text{for } g = 2 \ldots . (N_s - 1) \\ \int_{s_{g-1}^t + s_g^t)/2}^{\infty} f_s^t(s)ds & \text{for } g = N_s \end{cases} , \quad (13)$$

$$PG_{PVg(s_{ag})=NPvmodel*FF*Vg*Ig}$$

The current, voltage, and temperature of the panel are determined as follows:

$$\begin{cases} Ig = Sag((Isc + Ki(Tc - 25)) \\ Vg = Voc - Kv * Tcg \\ Tcg = T_A + Sag(\frac{Not-20}{.8}) \end{cases} \quad (14)$$

The efficiency of each solar panel is calculated according to (15):

$$FF = \frac{V_{MPP} * I_{MPP}}{Voc * Isc} \quad (15)$$

I_{MPP} and V_{MPP} are the maximum voltage and current of each panel. Losses P_{Loss} are calculated according to Equation (16):

$$PLoss = \frac{\sum_{t=1}^{Nt} \sum_{i=1}^{N1} \frac{r_i((P_{D,i+1}^t)^2 + ((Q_{D,i+1}^t)^2}{(V_{i+1}^t{}^2)}}{Nt} \quad (16)$$

$P_{D,i+1}^t$ and $Q_{D,i+1}^t$, are the active and reactive power, V_{i+1}^t is the bus voltage, and Nt is the number of bus lines.

B. Objective Function

For the sake of stability and security, as well as to improve the power quality, several limits are established for the voltage and current across the lines, as well as for the losses. Hence, the above-mentioned constraints imply an optimization problem. To solve the problem with the one-objective optimization method, the variable weighting technique is used (Equation (17)). The goals of the optimization problem are to minimize the average annual power losses, maximize the voltage stability index, and minimize the network security index. Traditionally, a multi-objective problem is reconstructed into a single-goal optimization one via the weight accumulation method, as the objective functions depend on the location, size, and type of renewable DGs. Thus, a multi-objective performance index can be formulated [55]:

(17)

$$F = f\left(\sum_{i=2}^{Nb} \sum_{j€type} PDG_{i,j} * ni * Li\right) = w1 * sPLos_a - w2 * VSF_a + w3 * NSIa \quad wi = [0 \, ,1]$$

$PDG_{i,j}$, is the bus injection capability and w is the weight function. Indicators are used to assess voltage stability. Buses in the transmission or distribution network are very fast And effective tools for measuring off-line voltage stability Status of buses Voltage stability index VSF proposed in for each bus-i in the time segment's' can be displayed as follows Nb is the total number of network buses. It is assumed that Bass-1 is located in the main distribution post. . The network will become more stable. VSF is calculated according to Equation (18):

$$SFa = \frac{\sum_{t=1}^{Nt} \sum_{i=2}^{Nb} VSF_{i+1}^t}{N_t(N_b-1)} \quad , VSF_{i+1}^t = (2_{i+1}^t - V_i^t) \quad (18)$$

The formulation of losses while considering generation and reactive power is expressed below [56]:

$$PG_{ss}^t + \sum_{i=2}^{Nb} \sum_{j€type} PDG_{i,j} * ni * Li - \sum_{i=2}^{Nb} P_{Di}^t - PLoss^t = 0 \, , QG_{ss}^t + - \sum_{i=2}^{Nb} Q_{Di}^t - QLoss^t = 0 \quad (19)$$

Eq. (23) is considered in the distribution network:

$$\sum_{i=2}^{Nb}\sum_{j\in type} PDG_{i,j} * ni * Li \le \sum_{i=2}^{Nb} P_{Di}^{t} \quad (20)$$

Where PG_{ss}^{t} and QG_{ss}^{t} are the active and reactive power fed by the substation at a given time, and Plosst and Qlosst are the active and reactive power losses at a given time PSO algorithm, whose full details are reported elsewhere [57], was implemented in this research.

C. *Backtracking search optimization algorithm (BSOA)*

Backtracking search optimization algorithm is introduced in [30-31]. This algorithm uses the jump operator during the search to avoid getting stuck in local optima during the first iterations while obtaining new solutions. The main components of BSOA-based design, i.e., initialization, selection, mutation, reproduction, and selection, are described. There will be a random generation (PoP) initialization phase at the edge boundaries:

$$\begin{aligned}&\text{for i} = 1\text{: PopSize}\\&\text{for j} = 1\text{: D}\\&\text{PoP(i, j)} = \text{PoPmax(j)} - \text{rand/}\\&\text{(PoPmax(j)} - \text{PoPmin(j))}\\&\text{end}\\&\text{end}\end{aligned} \quad (21)$$

In relation (21), Pop Size and D are the maximum population size and the dimensions of the population set. The algorithm with selection, mutation and reproduction is the following steps:

$$\begin{aligned}&\text{Define mixrate}\\&\text{oldPoP} = \text{oldPoP(randperm(PopSize), :);}\\&\text{map} = \text{zeros(PopSize, D);}\\&\text{if rand} < \text{rand,}\\&\text{for i} = 1\text{: PopSize,}\\&\text{u} = \text{randperm(D);}\\&\text{map(i, u(1: ceil(mixrate} * \text{rand} * \text{D))) = 0;}\\&\text{end}\\&\text{else}\\&\text{for i} = 1\text{: PopSize,}\\&\text{map(i, randi(D)) = 0;}\\&\text{end}\end{aligned} \quad (22)$$

III. The System under Study and result

The single-line diagram of the studied system (IEEE 33-bus network) [58-59] is shown in Figure (4), and the model information is shown in the Appendix. The set under study comprises a combination of the aforementioned resources, along with their quantity and location. There are several Properties in power systems, including changes in network load and the accidental output of power equipment.

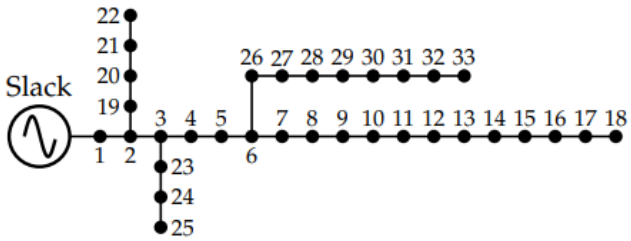

Fig. 4. IEEE standard model of a 33-bus distribution network

With regard to the performance of the system for a 24-hour period, the probability distribution program of solar and wind power plant is shown in Figures 5 and 6, and the information of these models is given in Tables 1 and 2. Due to the relatively small asymmetry, the probability distribution of the resources is relatively symmetric and may be approximated by a normal distribution. If it has a relatively large and positive symmetry, the probability distribution will tend to be in one direction (left or right). In this case, it cannot be approximated to a normal distribution. Data sometimes creates a curve that does not have a natural distribution, i.e., its two ends are not symmetrical. When there is no fit between the two ends of the curve, the curve is skewed.

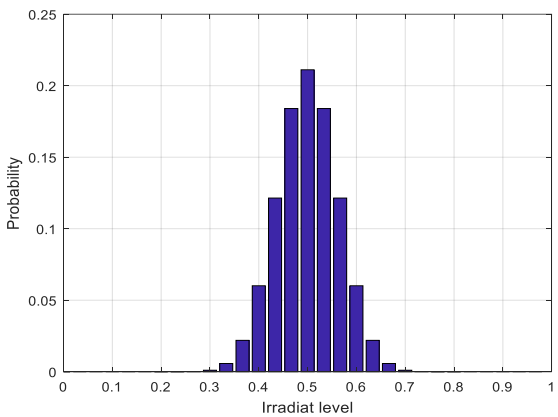

Fig. 5. Probability distribution of solar power (monte carlo methods) [59]

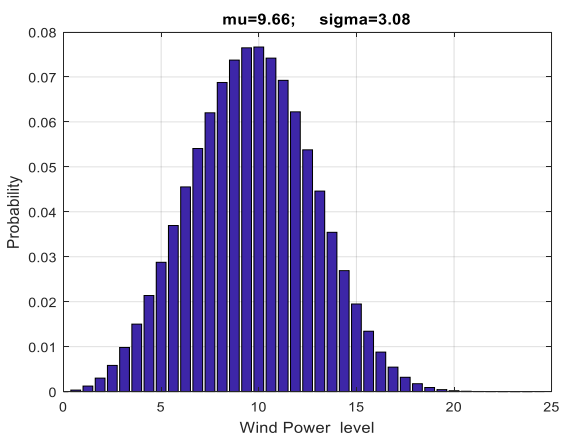

Fig. 6. Probability distribution of wind power (monte carlo methods) [59]

In Table 1, a comparative summary of the literature on the protection of smart grids and MGs has been presented. The summarized literature review shows that a research gap exists in developing a new study for MG protection using the DS-DOCRs that takes into account N-1 contingency-based network topologies and corresponding selectivity constraints. This research aims to fill this gap. Indeed, using the DS-DOCRs, as a specified characteristic, would be useful to mitigate the challenges of the protection system's speed in [4].

TABLE 1
PARAMETERS STUDIED IN THE SOLAR SYSTEM

Photovoltaic system power	200W
Maximum voltage	$28.36V$
Maximum current	7.76 A
Open circuit voltage	36.96V
Short circuit current	8.38 A
Flow on temperature factor	$Ki = 0.00545$
Voltage on temperature factor	$Kv = -0.1278$

TABLE 2
WIND SYSTEM INFORMATION [59]

Minimum wind speed	5 m/s
Maximum wind speed	20 m/s
Average wind speed	9 m/s
Generation capacity	250 kW

Figure 7 shows the proposed per-unit load value for the four seasons. Note that the load peaks occur many times at noon and during the night.

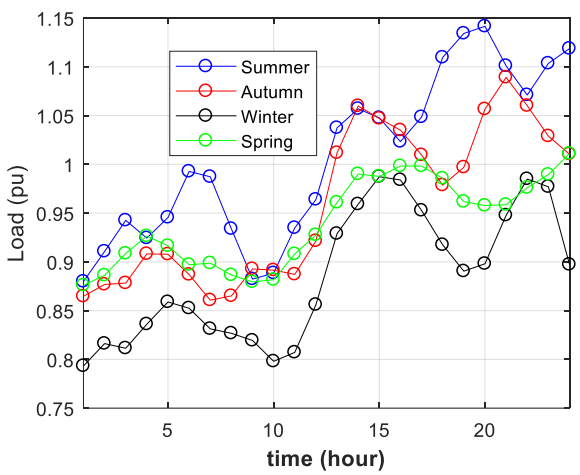

Fig.7. Load for a season of the year for DG resources

In the first stage, the PSO algorithm is used to find locate wind power plants. As an optimization issue, the mode estimation problem requires deliberate and restricted performance. Figure 8 shows the power generation of wind and solar power plants throughout a day. The variable loads and generators are considered to be fixed variables, and the distributed generation resources are regarded as variable modes. The results regarding losses with wind, solar, and hybrid sources are shown in Figures 9, 10, and 11, respectively. Figure 12 shows the convergence diagram for locating three wind power plants.

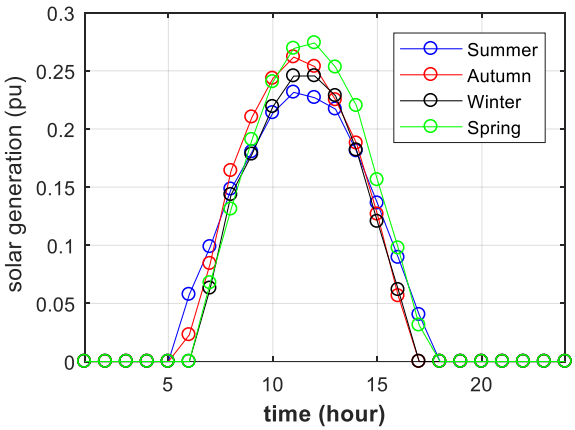

(a)

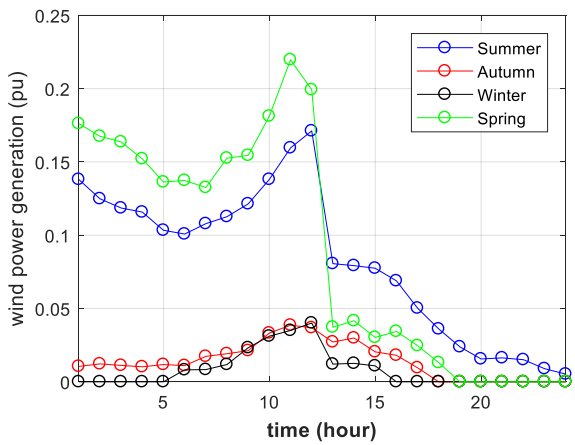

(b)

Fig. 8. Power generation after implementing the PSO algorithm throughout the day in a year with four seasons: (a) Hourly solar power generation and (b) wind power generation in the studied period

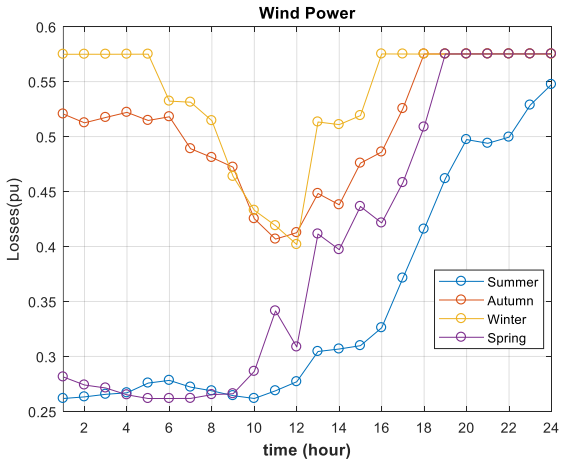

Fig. 9. Results of losses with wind sources

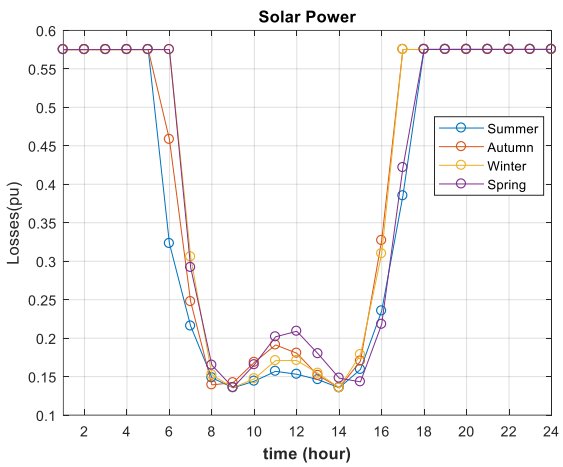

Fig.10. Results of losses with solar sources

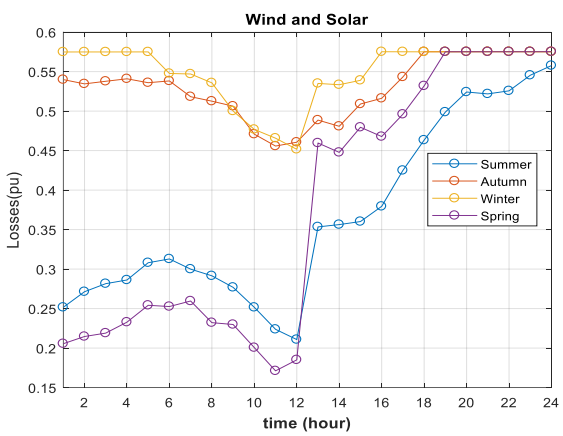

Fig.11. Results of losses with hybrid sources

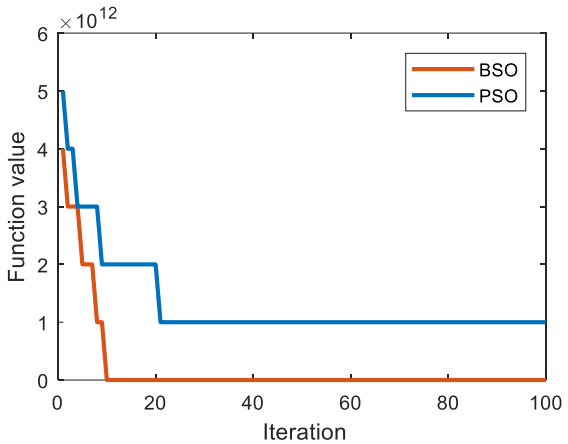

Fig.12. Convergence of the algorithms

Distributed generation resources usually reduce the feeding path, which reduces network losses. A load-proportional DG is installed at the desired location according to the relationship between the loss formulation and the reduced injection capacity. In fact, the effect of these sources is on the voltage and loss profiles, and these two components are closely related. The presence of DGs, as they feed loads locally, also reduces network load (Figure 13) and frees up the different line capacity, which is one of the advantages of these resources. However, some lines may be overloaded if the design is not adequate. Normally, DG reduces line current by feeding part of the network load. However, de-pending on the size and condition of the network, it is possible for the DG current to flow in the opposite direction. If the DG is larger than its loads, part of its current will return to the post. This may not be a problem unless the flow through the post is greater than the conductor capacity. However, this can occur under certain conditions, one of which is the release of loads after the DG due to unpredictable errors. If the DG size is large and the network is designed based on the same assumptions as traditional networks, it may face overcurrent issues. Figures (14, 15) show the load of lines with solar and hybrid resources. Note that, with the hybrid system, the line release space is significantly different than that of the previous two modes. The three wind resources are placed at nodes 30, 24, and 13 of the IEEE 33-bus network. More wind and solar resources were also tested, and their locations are shown in Tables 3 to 5.

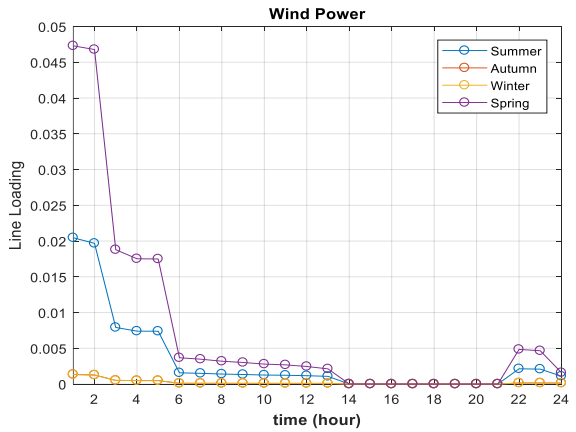

Figure 13. Load rate of lines in optimal condition with wind resources

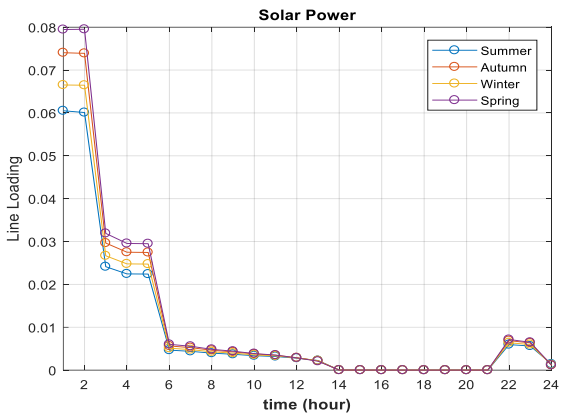

Fig.14. Load rate of lines in optimal condition with solar resources

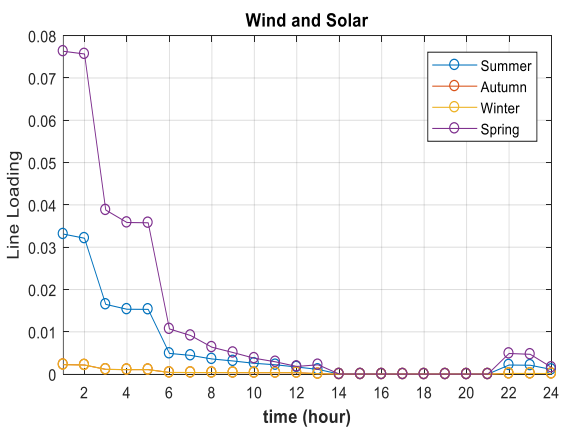

Fig. 15. Load rate of lines in optimal condition with wind and solar resources

TABLE 3
LOCATING WIND RESOURCES IN THE 33-BUS NETWORK

Number of wind resources	Locating resources with BSO	Locating resources with PSO
3	13-24-30	11-24-30
4	4-24-27-30	4-24-27-30
5	7-13-14-29-32	7-13-14-29-32

TABLE 4
LOCATING SOLAR RESOURCES IN THE 33-BUS NETWORK

Number of solar resources	Locating resources sources with BSO	Locating resources with PSO
3	13-24-30	13-24-30
4	11-13-17-27	11-15-17-27
5	13-14-27-29-32	13-14-27-29-30

TABLE 5
LOCATING HYBRID RESOURCES IN THE 33-BUS NETWORK

Number of hybrid resources	Locating resources with BSO	Locating resources with PSO
3	13-24-30	13-24-30
4	11-13-17-27-32	11-16-17-27-32
5	7-13-27-29-32	7-13-27-29-31

IV. Conclusions

The utilization of renewable energy sources, which have a fluctuating nature, has increased the unpredictability of power networks, which poses a number of challenges to their design and development. This study presented the calculation of the probability density function for networks with loads and wind and solar sources with variable output, thus contributing to the minimization of the u coordination in network load and unintentional power equipment output. Sustainable wind and solar power systems were located using the particle swarm optimization algorithm. In this study, the effect of distributed generation on a 33-bus network was analyzed. The optimal location of solar and wind resources was determined by considering seasonal loads and changes in weather conditions such as solar radiation level and wind speed. The coordination of these sources was based on the PSO and BSO algorithms, aiming to reduce the line load. The results show acceptable performance under various conditions, and the presence of DGs reduces network load because they feed loads locally. The optimal results of resources with two algorithms were compared and showed close answers. These systems can be used in remote areas without power grids or even in areas where, despite the existence of a power grid, there is a tendency to use renewable energy. It is presented for future research in this field:

• Reducing voltage fluctuations to achieve the maximum production power from DG sources

• Improving line losses by using compensators

REFERENCES

[1] Ahmed, Z., Ahmad, M., Rjoub, H., Kalugina, O. A., & Hussain, N. (2021). Economic growth, renewable energy consumption, and ecological footprint: Exploring the role of environmental regulations and democracy in sustainable development. Sus-tainable Development. https://doi.org/10.1002/sd.2251

[2] Adebayo, T. S., Rjoub, H., Akinsola, G. D., & Oladipupo, S. D. (2022). The asymmetric effects of renewable energy consumption and trade openness on carbon emissions in Sweden: new evidence from quantile-on-quantile regression approach. Environmental Science and Pollution Research, 29(2), 1875-1886.

[3] Adebayo, T. S., & Rjoub, H. (2021). A new perspective into the impact of renewable and nonrenewable energy consumption on environmental degradation in Argentina: a time–frequency analysis. Environmental Science and Pollution Research, 1-17.

[4] Odugbesan, J. A., & Rjoub, H. (2020). Relationship among economic growth, energy consumption, CO2 emission, and urbanization: evidence from MINT countries. Sage Open, 10(2), 2158244020914648.

[5] Farhadi, P., & Taheri, B. (2017, April). Smart meter tariff pricing using load demand response model. In 2017 5th International Istanbul Smart Grid and Cities Congress and Fair (ICSG) (pp. 135-139). IEEE.

[6] Liang Zhang, Xuesong Wang, Zhe Zhang, Ying Cui, Lyu Ling,... Cai, G. (2021). An Adaptative Control Strategy for Interfacing Converter of Hybrid Microgrid Based on Improved Virtual Synchronous Generator. IET Renewable Power Generation. doi: 10.1049/rpg2.12293

[7] Jalili, A., & Taheri, B. (2020). Optimal sizing and sitting of distributed generations in power distribution networks using firefly algorithm. Technology and Economics of Smart Grids and Sustainable Energy, 5, 1-14.

[8] Zishan, F., Akbari, E., Montoya, O. D., Giral-Ramírez, D. A., & Nivia-Vargas, A. M. (2022). Electricity retail market and ac-countability-based strategic bidding model with short-term energy storage considering the uncertainty of consumer demand response. Results in Engineering, 100679.

[9] Cho, G. J., Kim, C. H., Oh, Y. S., Kim, M. S., & Kim, J. S. (2018). Planning for the future: Optimization-based distribution planning strategies for integrating distributed energy resources. IEEE Power and Energy Magazine, 16(6), 77-87.

[10] Tightiz, L., Mansouri, S., Zishan, F., Yoo, J., & Shafaghatian, N. (2022). Maximum Power Point Tracking for Photovoltaic Systems Operating under Partially Shaded Conditions Using SALP Swarm Algorithm. Energies, 15(21), 8210.

[11] Kalantar, Saeed Vedadi, Amir Ali Saifoddin, Ahmad Hajinezhad, and Mohammad Hossein Ahmadi. "A Solution to Prevent a Blackout Crisis: Determining the Behavioral Potential and Capacity of Solar Power." International Journal of Photoenergy 2021 (2021).

[12] Ganjei, N., Zishan, F., Alayi, R., Samadi, H., Jahangiri, M., Kumar, R., & Mohammadian, A. (2022). Designing and Sensitivity Analysis of an Off-Grid Hybrid Wind-Solar Power Plant with Diesel Generator and Battery Backup for the Rural Area in Iran. Journal of Engineering, 2022.

[13] D. Ma et al., "Dual-Predictive Control with Adaptive Error Correction Strategy for AC Microgrids," IEEE Transactions on Power Delivery , Volume: 37, Issue: 3, June 2022.

[14] Grisales-Noreña, L. F., Montoya, O. D., Cortés-Caicedo, B., Zishan, F., & Rosero-García, J. (2023). Optimal Power Dispatch of PV Generators in AC Distribution Networks by Considering Solar, Environmental, and Power Demand Conditions from Colombia. Mathematics, 11(2), 484.

[15] Fan, S., Wang, Y., Cao, S., Zhao, B., Sun, T.,... Liu, P. (2022). A deep residual neural network identification method for uneven dust accumulation on photovoltaic (PV) panels. Energy (Oxford), 239, 122302. doi: 10.1016/j.energy.2021.122302

[16] Taheri, B., Foroud, A. A., & Jabari, F. (2023). Design and performance optimization of a tri-generation energy hub considering demand response programs. Energy Science & Engineering, 11(2), 675-684.

[17] R. Wang, Q. Sun, W. Hu, Y. Li, D. Ma and P. Wang, "SoC-Based Droop Coefficients Stability Region Analysis of the Battery for Stand-Alone Supply Systems With Constant Power Loads," in IEEE Transactions on Power Electronics, vol. 36, no. 7, pp. 7866-7879, 2021.

[18] Zishan, F., Mansouri, S., Abdollahpour, F., Grisales-Noreña, L. F., & Montoya, O. D. (2023). Allocation of Renewable Energy Resources in Distribution Systems while Considering the Uncertainty of Wind and Solar Resources via the Multi-Objective Salp Swarm Algorithm. Energies, 16(1), 474.

[19] Rikani, A. S. (2021). Numerical analysis of free heat transfer properties of flat panel solar collectors with different geometries. Journal of Research in Science, Engineering and Technology, 9(01), 95-116.

[20] Huy, P. D., Ramachandaramurthy, V. K., Yong, J. Y., Tan, K. M., & Ekanayake, J. B. (2020). Optimal placement, sizing and power factor of distributed generation: A comprehensive study spanning from the planning stage to the operation stage. Energy, 195, 117011.

[21] Zhang, S., Cheng, H., Li, K., Tai, N., Wang, D., & Li, F. (2018). Multi-objective distributed generation planning in distribu-tion network considering correlations among uncertainties. Applied energy, 226, 743-755.

[22] Jiawen Bai et al., " Day-Ahead Robust Economic Dispatch Considering Renewable Energy and Concentrated Solar Power Plants'', Energies 2019, 12(20), 3832.

[23] Sadeghi, B., Shafaghatian, N., Alayi, R., El Haj Assad, M., Zishan, F., & Hosseinzadeh, H. (2022). Optimization of synchronized frequency and voltage control for a distributed generation system using the Black Widow Optimization algorithm. Clean Energy, 6(1), 869-882.

[24] Ahmadi, Mohammad Hossein, Alireza Baghban, Milad Sadeghzadeh, Mohammad Zamen, Amir Mosavi, Shahaboddin Shamshirband, Ravinder Kumar, and Mohammad Mohammadi-Khanaposhtani. "Evaluation of electrical efficiency of photovoltaic thermal solar collector." Engineering Applications of Computational Fluid Mechanics 14, no. 1 (2020): 545-565.

[25] R. Wang, Q. Sun, D. Ma and Z. Liu, "The Small-Signal Stability Analysis of the Droop-Controlled Converter in Electromagnetic Timescale," in IEEE Transactions on Sustainable Energy, vol. 10, no. 3, pp. 1459-1469, July 2019.

[26] Akbari, E., Sheikholeslami, A. R., & Zishan, F. (2023). Participation of Renewable Energy in Providing Demand Response in Presence of Energy Storage. Renewable Energy Research and Applications, 4(2), 225-234.

[27] Böttcher, O. (2012). Energy efficient and sustainable—federal buildings in Germany. REHVA J, 49(3), 41-45.

[28] Alayi, R., Zishan, F., Mohkam, M., Hoseinzadeh, S., Memon, S., & Garcia, D. A. (2021). A sustainable energy

distribution configuration for microgrids integrated to the national grid using back-to-back converters in a renewable power system. Electronics, 10(15), 1826.

[29] Taheri, B., Jabari, F., & Foroud, A. A. (2023). A green cogeneration microgrid composed of water-source heat pumps, a gravity energy storage, and a bio-fueled gas turbine: design and techno-economic optimization. Sustainable Cities and Society, 104594.

[30] Zamani, R., Hamedani-Golshan, M. E., Haes Alhelou, H., Siano, P., & R Pota, H. (2018). Islanding detection of synchronous distributed generator based on the active and reactive power control loops. Energies, 11(10), 2819.

[31] Maalla, A. (2020, June). Research on Reactive Power Control of the HVDC Transmission System. In 2020 IEEE 4th Infor-mation Technology, Networking, Electronic and Automation Control Conference (ITNEC) (Vol. 1, pp. 2475-2479). IEEE.

[32] Zishan, F., Akbari, E., Montoya, O. D., Giral-Ramírez, D. A., & Molina-Cabrera, A. (2022). Efficient PID Control Design for Frequency Regulation in an Independent Microgrid Based on the Hybrid PSO-GSA Algorithm. Electronics, 11(23), 3886.

[33] Tang, Y., Hu, W., Cao, D., Hou, N., Li, Y., Chen, Z., & Blaabjerg, F. (2021). Artificial intelligence-aided minimum reactive power control for the DAB converter based on harmonic analysis method. IEEE Transactions on Power Electronics, 36(9), 9704-9710.

[34] Ehsan, A., & Yang, Q. (2018). Optimal integration and planning of renewable distributed generation in the power distribu-tion networks: A review of analytical techniques. Applied Energy, 210, 44-59.

[35] Mykola, T., Valerii, K., Andriy, R., Demeshchuk, V., & Bohdan, K. (2019). Evaluating Simulation and Development of Algo-rithms of Energy Consumption Reduction Based on Wireless Sensor Networks. Journal of Research in Science, Engineering and Technology, 7(3), 18-24.

[36] Wang, Y., Zou, R., Liu, F., Zhang, L., & Liu, Q. (2021). A review of wind speed and wind power forecasting with deep neural networks. Applied energy, 304, 117766. doi: 10.1016/j.apenergy.2021.117766

[37] K. Deb, A. Kumar, Real coded genetic algorithms with simulated binarycrossover: studies on multi modal and multi objec-tive problems, Complex Syst.9 (1995) 431–454.Quezada, V. M., Abbad, J. R., & Roman, T. G. S. (2006). Assessment of energy dis-tribution losses for increasing penetration of distributed generation. IEEE Transactions on power systems, 21(2), 533-540.

[38] R.C. Eberhart, J. Kennedy, A new optimizer using particle swarm theory, in: Pro-ceedings of the Sixth International Sym-posium on Micro Machine and HumanScience, New York, NY, 1995, pp. 39-43.

[39] Zhang, M., Xu, Z., Lu, X., Liu, Y., Xiao, Q., & Taheri, B. (2021). An optimal model identification for solid oxide fuel cell based on extreme learning machines optimized by improved Red Fox Optimization algorithm. International Journal of Hydrogen Energy, 46(55), 28270-28281.

[40] Moradi, M. H., & Abedini, M. (2012). A combination of genetic algorithm and particle swarm optimization for optimal DG location and sizing in distribution systems. International Journal of Electrical Power & Energy Systems, 34(1), 66-74.

[41] Aman, M. M., Jasmon, G. B., Mokhlis, H., & Bakar, A. H. A. (2012). Optimal placement and sizing of a DG based on a new power stability index and line losses. International Journal of Electrical Power & Energy Systems, 43(1), 1296-1304.

[42] Atwa, Y. M., El-Saadany, E. F., Salama, M. M. A., & Seethapathy, R. (2009). Optimal renewable resources mix for distribution system energy loss minimization. IEEE Transactions on Power Systems, 25(1), 360-370.

[43] Hung, D. Q., Mithulananthan, N., & Bansal, R. C. (2010). Analytical expressions for DG allocation in primary distribution networks. IEEE Transactions on energy conversion, 25(3), 814-820.

[44] Porwik, P., Doroz, R., & Orczyk, T. (2016). Signatures verification based on PNN classifier optimised by PSO algorithm. Pattern Recognition, 60, 998-1014.

[45] G.Carpinelli,P.Caramia,P.Varilone, Multi-linear Monte Carlo simulation method for probabilistic load flow of distribution systems with wind and photovoltaic generation systems, Renewable Energy, Volume 76, April 2015, Pages 283–295.

[46] Montoya, O. D., Zishan, F., & Giral-Ramírez, D. A. (2022). Recursive Convex Model for Optimal Power Flow Solution in Monopolar DC Networks. Mathematics, 10(19), 3649.

[47] Akbari, E., Shafaghatian, N., Zishan, F., Montoya, O. D., & Giral-Ramírez, D. A. (2022). Optimized Two-Level Control of Islanded Microgrids to Reduce Fluctuations. IEEE Access, 10, 95824-95838.

[48] M. Rostamzadeh1, K. Valipour1, S. J. Shenava1, M. Khalilpour1, N. Razmjoo,'' Optimal location and capacity of mul-ti-distributed generation for loss reduction and voltage profile improvement using imperialist competitive algorithm'', Artificial Intelligence Research, December, Vol(1), 22012.

[49] A.M. El-Zonkoly,'' Optimal placement of multi-distributed generation units including different load models using particle swarm optimization'', Swarm and Evolutionary Computation (1),2011.

[50] Reza Jabbari-Sabeta , Seyed-Masoud Moghaddas-Tafreshib, Seyed-Sattar Mirhoseinic,'' Microgrid operation and manage-ment using probabilistic reconfiguration and unit commitment'', Electrical Power and Energy Systems (75), (2016) .

[51] Ugranlı F. Ersavas_ C. Karatepe E. Neural network based distributed generation allocation for minimizing voltage fluctua-tion due to uncertainty of the output power. In: Proc IEEE INISTA, June, 2011, Istanbul, Turkey; 2011. p. 415–9.

[52] Karki R, Hu P, Billinton R. A simplified wind power generation model for reliability evaluation. IEEE Trans Energy Con-vers 2006;21(2):413–8.

[53] Mansouri, S., Zishan, F., Montoya, O. D., Azimizadeh, M., & Giral-Ramírez, D. A. (2023). Using an intelligent method for microgrid generation and operation planning while considering load uncertainty. Results in Engineering, 17, 100978.

[54] Mohseni - Bonab, Seyed Masoud, and Abbas Rabiee. "Optimal reactive power dispatch: a review, and a new stochastic voltage stability constrained multi - objective model at the presence of uncertain wind power generation." IET Generation, Transmission & Distribution 11.4 (2017): 815-829.

[55] Singh D, Misra RK, Singh D. Effect of load models in distributed generation planning. IEEE Trans Power Syst 2007;22:2204e12.

[56] Kayal P, Chanda CK. Placement of wind and solar based DGs in distribution system for power loss minimization and

voltage stability improvement. Elect Power Energy Syst 2013;53:795e809.
[57] Alayi, R., Zishan, F., Seyednouri, S. R., Kumar, R., Ahmadi, M. H., & Sharifpur, M. (2021). Optimal load frequency control of island microgrids via a PID controller in the presence of wind turbine and PV. Sustainability, 13(19), 10728.
[58] Sarineh Hacopian Dolatabadi, Maedeh Ghorbanian, Pierluigi Siano, and Nikos D. Hatziargyriou,'' An Enhanced IEEE 33 Bus Benchmark Test System for Distribution System Studies'', IEEE Transactions on Power Systems , Volume: 36, Issue: 3, 2021.
[59] Morteza Aien, Mahmud Fotuhi-Firuzabad, and Masoud Rashidinejad,'' Probabilistic Optimal Power Flow in Correlated Hybrid Wind–Photovoltaic Power Systems''IEEE TRANSACTIONS ON SMART GRID, VOL. 5, NO. 1, JANUARY 2014.

Farhad Zishan was born in Ardabil, Iran, 1985. He received the B.Sc. degree in Electrical Power Engineering from Islamic Azad University, Ardabil, Iran, in 2014and M.Sc degrees in Electrical Power System, from 2015 to 2017. In 2020, I entered the PhD course in power electricity at Sahand University of Technology. His research interests include renewable energy, distributed generation, optimization and power system .

Ehsan Akbari received the MSc degree from Mazandaran University of Science & Technology (MUST), Babol, Iran, in electrical power engineering in 2014. His research interests include power quality and distribution flexible AC transmission systems (DFACTS), application of power electronics in power systems, power electronic multilevel inverters, smart grids, harmonics and reactive power control, and renewable energy systems.

Abdolreza Sheikholeslami was born in Iran. He received the B.Sc. (Hons.) degree in electrical engineering from Mazandaran University, Babolsar, Iran, in 1979, and the M.Sc. and Ph.D. degrees in electrical power engineering from the University of Strathclyde, Glasgow, U.K., in 1978 and 1989, respectively. He has been an Associate Professor with the Department of Electrical and Computer Engineering, Babol Noshirvani University of Technology, Babol, Iran, since 2009. His current research interests include power electronic, power quality, harmonics, smart grids, and renewable energy.

Nima Shafaghatian received his M.S. degree from Zanjan University and is currently studying Ph.D there. He has authored two articles in the well-known Journals, published by IET and Springer. He has also published two books on renewable energy and the relationship between industry and academia subjects. In addition to studying Ph.D, He is a lecturer at Al-Ghadir University in Zanjan and offers courses in electrical installations, smart home design and specialized language of electricity. His research interests include microgrids, distributed generation and electricity market.

International Journal Of
Industrial Electronics Control and Optimization
Print ISSN: 3517-2645
Online ISSN: 3568-2645
Homepage: https://ieco.usb.ac.ir/

Fractional-Order Variable Structure Equations In Robust Control

Ebrahim Abbaszadeh-Soorami[1] | Mohammad Haddad-Zarif[1]

Department of Electrical and Robotic Engineering, Shahrood University of technology, Shahrood, Iran.[1]
Corresponding author's email: mhzarif@shahroodut.ac.ir

Article Info

Article type:
Research Article

Article history:
Received: 2023-January-23
Received in: 2023- May-3
Accepted: 2023-May-23
Published online: 2023-July-1

Keywords:
Fractional-order,
Robust Control,
Fast Response,
Variable Structure Control.

ABSTRACT

This work is trying to introduce a fractional order floated pole controller as a fast and robust approach. We designed a robust variable structure control that yields a continuous and constrained control signal, also a fast response in the presence of model uncertainties and external disturbances. In the proposed controller, we employed the pole placement algorithm, then by designing proper polynomials gave it robust property, then due to a simple optimization routine, we make it fast and faster within the stability region. Finally, to evaluate the proposed method, numerical examples in different situations of the presence of noise, disturbance, and model uncertainties, also comparative results are presented. This paper proposed an accurate, fast, and robust controller. This can improve the performance of the perturbed functional systems used in the industrial fields. It is proposed to spread the benefit of fractional calculus in the control of complex systems in practical situations.

NOMENCLATURE AND SYMBOLS

q_n	Commensurate fractional order	PID	Proportional-Integral-Derivative
$E_{\alpha,\beta(z)}$	Mittag-Leffler function	VSC	Variable Structure Control
$\Gamma(.)$	Gamma function	SMC	Sliding-Mode Control
ζ	Time scale factor	SVSC	Soft Variable Structure Control
ζ_0	Maximum time scale factor	FPID	Fractional PID
α_k	characteristic ratios	CRA	Characteristic Ratio Assignment
$L\{.\}$	Laplace transform	PPC	Pole Placement Controller
FC	Fractional Calculus	TSMC	Terminal Sliding-Mode Control
FO	Fractional Order	FSMC	Fractional-order Sliding-Mode Control
FOS	Fractional-Order System	FO-PPC	Fractional Order Pole Placement Controller

I. Introduction

A. Background

The main goals of each control system are to achieve the appropriate speed and accuracy. Besides, the control systems demanded to be used in the industry suffer from degradation caused by model uncertainties and external disturbances. In this manuscript, with the benefit of recent findings on two wings Fractional Calculus (FC) and Variable Structure Control (VSC), we are to propose an accurate, fast, and robust controller. This can improve the performance of the perturbed functional systems; robust control provides a reliable base for future smart systems.

B. Literature review

As the first wing, in this work the FC is used to spread the benefit of FC in control of complex systems; moreover, the advantage of using FC in real application has been proven in recent research [1]. FC is the generalization of Integer-Order (IO) differentiation to Fractional-Order (FO) ones. It has a long history in mathematics, and today enhancing both transient and steady-state responses of the closed-loop performance is confirmed. Furthermore, FO controllers can make a very important role in robust systems against model uncertainties and disturbances [1, 2]. Fractional-order (FO) controllers offer greater flexibility in robustness that can only be achieved with high-order IO controllers [2]. Using FC in robust control can make a remarkable improvement compared to the conventional IO control [3]. In [4], an optimal approach for a fractional-order PID controller proposes to control electrical autonomous cars. In [5] the fractional-order PID controller in a combination of the type-2 fuzzy logic is developed for efficient and robust control of seismic systems. PID control as a common form of industrial control is faced limitations like uncertainties and parameter variations. Using FC in PID first proposed by Podlubny, and gives more efficiency in robustness of the system against gain variations [6, 7]. Sliding-Mode Control (SMC) as another traditional robust control strategy experiences chattering phenomenon, because of the switching non-linearity [8-10]. In [8], a model-free adaptive SMC is designed for control of input saturated chaotic systems. In [9] a fractional-order sliding mode controller is improved considering the estimated disturbance output. SMC uses a linear hyperplane as the sliding surface. In [10] a non-linear sliding mode observer is used to compensate cyber-attack and load disturbance in smart power systems. However, these control methods ensure asymptotic convergence of the system states to the equilibrium point, but there is no guarantee in finite-time. For a better robust control, the modified versions of SMC are used; like Higher-Order Sliding Mode Control, Terminal Sliding Mode Control (TSMC), etc... [11]. In [12] neural network-based TSMC is mentioned for control of the on-holonomic spherical robot. A deep recurrent neural networks with TSMC for a chaotic fractional-order financial system is proposed in [13]. Chattering is discussed still as a challenge in TSMC. Fuzzy and neural network approaches is used in SMC it's modified versions to enhance the robustness of systems [14]. In addition, using FC in SMC preserve all the advantages of SMC and additionally, can reduce chattering and to improve the robustness of the system. In [15] a new design of robust fractional adaptive decoupled control on a parallel micropositioning piezostage is proposed that contains three intuitional terms. A feedback model reference adaptive control term with fractional updating rules that represses the creep effect, external disturbances and parameters uncertainty, further increases the robustness and accuracy of positioning. However, this work assumes the prior knowledge of the upper bound of the system uncertainty. First use of fractional order control (FOC) in power electronics is mentioned in [16]. A new robust fractional-order super-twisting sliding mode control for supercapacitor-based power supply is proposed in [17]. As the chattering-free design of the controller, a robust, steady and smooth DC voltage can be provided. Also, this controller requires prior knowledge of the upper bound of system uncertainty.

On the second wing, VSC as an effective way to achieving the least settling time is performed. In VSC the control decision switches between *n* designed control way to achieve short settling times [18]. However, high frequency pattern switching in VSC is not desirable in industrial applications. So Soft Variable Structure Control (SVSC) introduced through increasing the number of predesigned structures to infinity in order to the selecting control function becomes continuous [18, 19]. But, because of the lack of robustness discussion, there is no reliability in the operational use of multitude of theatrical systems in the industrial environment.

C. Research gap and motivation

With an increasingly understanding of the potential of FOC, the number of studies and applications is increasing. However, by summarizing the current research results, it can be found that the research on this field is still at a preliminary stage. Our try is to develop a new control strategy for FO systems and help to complement the exploitation of the applications of FOS in modeling and controlling complex physical phenomena.

D. Challenges

To overcome the problem of disturbances in practice, applying FOC in variable structure schema is on the agenda; we are to solve the problems of modification of the RST control structure [19] with proper polynomials that guarantees the robustness of system, and propose a routine to vary the control signal continuously in a limited frame. The challenge relevant between velocity and parameters of the controller is adjusted by the Characteristic Ratio Assignment (CRA) method [20] in the FO pole placement algorithm [21]. The proposed VSC is to have a stable and robust control system,

with quick response, soft and restricted control signal.

E. Contribution

The contributions and novelties of the work are summarized as follows:

- The presented SVSC approach is raised in FO systems; compared with SVSC in [18] that are integer-order.
- The variable structure property of the proposed scheme, compared to fixed structure control in [22, 23], carries out a faster response, robust and stable control system, with a smooth and restricted control signal.
- In comparison with [19] that uses PSO, in this paper in order to decrease computational effort, a new simple and stable procedure for changing the parameters of the controller is proposed.
- In comparison with [19], system the robust performance and robust stability against external disturbances and model uncertainties is guaranteed.

F. Paper organization

This paper is organized as follows. In section 2 the procedure of the proposed SVSC is reviewed. Section 3 contains the stability and robustness discussion of the proposed control schema. Section 4 presents the simulations to validate the efficiency of the control system. Section 5 is dedicated to concluding remarks.

II. The proposed control scheme

To introduce the new proposed control scheme, we divided the dissection in four subsections: RST control structure, generalization to FO, desired commensurate system, and the SVSC approach.

A. *RST control structure*

The RST control structure is employed as a Pole Placement Controller (PPC) [20].

If we consider the system G and desired system G_m as follow:

$$G=\frac{B}{A}=\frac{b_n s^{q_n}+b_{n-1}s^{q_{n-1}}+\ldots+b_1 s^{q_1}+b_0}{a_m s^{p_m}+a_{m-1}s^{p_{m-1}}+\ldots+a_1 s^{p_1}+a_0} \quad (1)$$

$$G_m=\frac{B_m}{A_m}=\frac{b'_n s^{q'_n}+b'_{n-1}s^{q'_{n-1}}+\ldots+b'_1 s^{q'_1}+b'_0}{a'_m s^{p'_m}+a'_{m-1}s^{p'_{m-1}}+\ldots+a'_1 s^{p'_1}+a'_0} \quad (2)$$

Where $a_i, b_i, p_i, q_i \epsilon R$, $0<q_1<q_2<\cdots<q_n$ and $0<p_1<p_2<\cdots<p_m$. Also, $a'_i, b'_i, p'_i, q'_i \epsilon R$, $0<q'_1<q'_2<\cdots<q'_n$ and $0<p'_1<p'_2<\cdots<p'_m$. A_m is the desired characteristics polynomial and the A_c is closed loop characteristics polynomial from Diophantine equation:

$$AR+BS=A_c \quad (3)$$

So we will have:

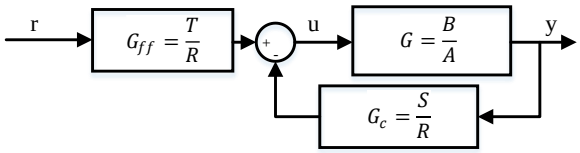

Fig 1. The RST control system

$$A_m y_{m(t)}=B_m u_{c(t)} \Rightarrow \frac{y_m}{u_c}=\frac{B_m}{A_m}=\frac{BT}{AR+BS}=\frac{BT}{A_C} \quad (4)$$

The controller polynomials R, S and T will be derived from (3) and (4).

B. *Generalized FO-PPC*

To generalize the RST method to FO-systems, at first, we make an integer-order reflection of FO polynomial. Therefore in polynomials, the minimum common resolution (q_n) will be chosen and substituted by δ. Second, the RST-based PPC will be applied to the reflective transfer functions [22].

$$G_{(\delta)}=\frac{B_{(\delta)}}{A_{(\delta)}}=\frac{b_n\delta^{p\beta_n}+b_{n-1}\delta^{p\beta_{n-1}}+\ldots+b_1\delta^{p\beta_1}+b_0}{a_m\delta^{p\alpha_m}+a_{m-1}\delta^{p\alpha_{m-1}}+a_1\delta^{p\alpha_1}+a_0} \quad (5)$$

$$G_{m(\delta)}=\frac{B_{m(\delta)}}{A_{m(\delta)}}=\frac{b'_n\delta^{gq'_n}+b'_{n-1}\delta^{gq'_{n-1}}+\ldots+b'_1\delta^{gq'_1}+b'_0}{a'_m\delta^{gp'_m}+a'_{m-1}\delta^{gp'_{m-1}}+a'_1\delta^{gp'_1}+a'_0} \quad (6)$$

The Diophantine equations (3 and 4) and Re-reflecting, give the S, R, and T, in FO form. By this design, the closed loop poles are directed to desired. Also, removing unstable zeros and poles is avoided.

C. *Desired commensurate system*

Because of the high-order nature of FOS, the velocity-parameters relation is adjusted by the CRA. According to CRA and Laplace scaling property, the response of closed loop systems (8), is ξ-times faster than the response systems (7) and the overshoots are the same.

$$G(s)=\frac{a_0}{a_n s^{qn}+a_{n-1}s^{q(n-1)}+\ldots+a_1 s^{q}+a_0} \quad (7)$$

$$G_{m(s)}=\frac{\zeta^{qn}a_0}{a_n s^{qn}+a_{n-1}\zeta^{q}s^{q(n-1)}+\ldots+\zeta^{q(n-1)}a_1 s^{q}+\zeta^{qn}a_0} \quad (8)$$

Where q is commensurate fractional order.

D. *The SVSC approach*

In the non-variable structure controller, the amplitudes of states decrease during the control period, so if we can modify the parameters of the controller during a control clock most capabilities of the control system can be used and earn a faster controller. Based on the proposed SVSC approach, at first, a FO-PPC will be designed; then the time-scaling factor ξ will be large and larger in the stability framework and constraint of the control signal. Changes in the controller's parameters make the system faster while the overall system is stable, the control signal is limited, and since the number of changes in the

controller decreases to infinity, the control signal is smooth.

In our proposed method, after shaping the FO-PPC, we try Increase ξ in $G_{m(s,\xi)}$ by consideration the following conditions:

$$\xi_i > \xi_0 > 0$$
$$\left| r\frac{G_{ff}}{1-GG_c} \right| - |u_{max}| \le 0 \quad (9)$$
$$|\xi_i - \xi_{i-1}| \le N|x_{(t)}|$$

Where N is a positive constant. We have $\xi_i = \xi_{i-1} + Nx_{(t)}$ and if the condition (9) is not fulfilled in the increase ξ, then $\xi_i = \xi_{i-1} - s_D x_{(t)}$ until establishment of (9). s_D is a positive constant. So we get the biggest time-scaling factor ξ, the desired commensurate system will be reshape in each control period i , and by applying the controller the overall system were faster and faster.

III. Stability, sensitivity and robustness

In this section, the stability discussion of the system is provided in subsections on internal and overall time-variant system stability. Also, the sensitivity and robustness of the proposed system against external disturbances, noise, and model uncertainties is interpreted.

A. Internal stability

In order to have internal stability and model following condition, BT and A_c have to have no common factor in in Diophantine equations (3, 4). So we separate polynomial B into B^+ and B^- as stable and an unstable part (10). The unstable poles of B^- cannot be canceled and it can cause instability problem; to overcome this problem, we can consider B^-as a part of B_m (11). And, B^+ should be a common factor in A_c and R (12, 13).

$$B = B^- B^+ \quad (10)$$
$$B_m = B^- B'_m \quad (11)$$
$$R = R'B^+ \quad (12)$$
$$A_c = A_0 . A_m . B^+ \quad (13)$$

Where A_0 is the residual part poles. Therefore, the Diophantine equation is reduced as bellows.

$$AR' + B^- S = A_0 A_m \quad (14)$$

Also, about T we will have

$$T = A_0 B'_m \quad (15).$$

B. Time-variant system stability

Changing the controller parameters during every control clock leads the proposed controller to a FO time-variant system. We consider the proposed SVSC as the following system.

$$\frac{d^\alpha}{dt^\alpha} x(t) = \tilde{A}(t)x(t) = \bar{A}x(t) + \Delta A(t)x(t) \quad (16)$$

Where $x(t) \in R^n$ is the system state vector, $\tilde{A}(t) \in R^{n\times n}$ is system equivalent matrix. The VSC approach produces the time-variant portion , $\Delta A(t) \in R^{n\times n}$, the , $\bar{A}(t) \in R^{n\times n}$ is a constant matrix, and $0 < \alpha < 2$ is fractional order

In the following, before presenting the main theory of stability of the studied system, it is necessary to mention some definitions and lemmas.

Definition 1: The α-order Caputo derivative of function $h_{(t)}$ is defined as (17), and its Laplace transform at $t_0 = 0$ is written as (19) [1].

$${}_{t_0}^{C}D_t^\alpha h(t) = \frac{1}{\Gamma(n-\alpha)}\int_{t_0}^{t}(t-\tau)^{n-\alpha-1}h^{(n)}(\tau)d\tau, \quad n-1<\alpha\le n \quad (17)$$

$$\Gamma(\tau) = \int_0^\infty t^{\tau-1}e^{-t}dt. \quad (18)$$

$$\int_0^\infty e^{-st}\,{}_{t_0}^{C}D_t^\alpha x(t)dt = s^\alpha X(s) - \sum_{k=0}^{n-1} s^{\alpha-k-1}x^{(k)}(0), (n-1<\alpha\le n) \quad (19)$$

Where $\Gamma(.)$ denotes the Gamma function.

Definition 2: The system ${}_{t_0}^{C}D_t^\alpha x(t) = g_{(t,x(t))}$, $0 < \alpha \le 1$ (also $1 < \alpha < 2$) is stable if, for any initial values, there is $\varepsilon > 0$ such that $\|x\| < \varepsilon$ for all $t > t_0$. The system is asymptotically stable if $\|x\| \to 0$ as $t \to +\infty$.

Definition 3 [1, 24]: The introduction of Mittag-Leffler function is mentioned in (20), and its two-parameters form and its Laplace transform are mentioned in (21) and (22).

$$E_\alpha(z) = \sum_{k=0}^{\infty}\frac{z^k}{\Gamma(k\alpha+1)} \quad (20)$$

$$E_{\alpha,\beta}(z) = \sum_{k=0}^{\infty}\frac{z^k}{\Gamma(k\alpha+\beta)} \quad (21)$$

$$L\left\{t^{\beta-1}E_{\alpha,\beta}(-\lambda t^\alpha)\right\} = \frac{s^{\alpha-\beta}}{s^\alpha+\lambda}, (R(s) > |\lambda|^{\frac{1}{\alpha}}) \quad (22)$$

Where z is a complex number, $0 < \alpha$, $0 < \beta$ and $L\{.\}$, is the Laplace transform symbol. In particular, if $\alpha = 1$ and $\beta = 1$, then $E_{1,1}(z) = e^z$.

Lemma 1 [19]: If $A \in C^{n\times n}$ and $0 < \alpha < 2$, μ satisfies $\pi\alpha/2 < \mu < \min\{\pi, \pi\alpha\}$, β is an arbitrary real number, and $P > 0$ is a real constant, then Mittag-Leffler function in (23) applies.

$$\left\|E_{\alpha,\beta}(A)\right\| \le \frac{\mathrm{P}}{1+\|A\|} \tag{23}$$

In which $\mu \le \left|\arg(spec(A))\right| \le \pi$, $\|.\|$ is the L_2 norm and $spec(.)$ denotes the eigenvalues of the matrix.

Lemma 2: based on Gronwall inequality [19] for all continuous functions on $[t_0,T), T \le +\infty$, $k(t) \ge 0$ and we have

$$x(t) \le h(t) + \int_{t_0}^{t} k(s)x(s)ds, \qquad t \in [t_0,T) \tag{24}$$

then $x(t)$ convinces

$$x(t) \le h(t) + \int_{t_0}^{t} k(s)h(s)\exp\left[\int_{s}^{t} k(u)du\right]ds. \tag{25}$$

Theorem 1: For *fractional order* α if*:*

a) $0 < \alpha \le 1$, $\left|\arg(spec(A))\right| > \alpha\pi/2$, $\alpha\|A\| > 1$, *and* $\Delta A(t)x(t)$ *in* $\lim_{x\to 0}{}^{\|\Delta A(t)x(t)\|}/_{\|x(t)\|} = 0$ *applies,*

b) $1 < \alpha \le 2$, $\left|\arg(spec(A))\right| > \alpha\pi/2$, $(\alpha-1)\|A\| > 1$, *and* $\Delta A(t)x(t)$ *in* $\lim_{x\to 0}{}^{\|\Delta A(t)x(t)\|}/_{\|x(t)\|} = 0$ *applies,*

then the system (16) is asymptotically stabile.

Proof. (a). The PPC system is as follows.

$$D^{\alpha}X = AX + Bu = (A+BK)X = \bar{A}X \tag{26}$$

Where $K \in R^n$ includes the pole placement gains and $A+BK = \bar{A}$. So the time-variant proposed SVSC can be considered as (16).

To get the solution of (16), firstly we take Laplace transform on (16), and secondly Laplace inverse transform.

$$X(s) = (Is^{\alpha} - A)^{-1}(s^{\alpha-1}x_0 + L\{\Delta A(t)x(t)\}) \tag{27}$$

$$x(t) = E_{\alpha,1}(A(t-t_0)^{\alpha})x_0 + \int_{t_0}^{t}((t-\tau)^{\alpha-1}E_{\alpha,\alpha}(A(t-\tau)^{\alpha})\Delta A(\tau)x(\tau)d\tau, \tag{28}$$

Where I is identity matrix.

Lemma 1 says that there exist positive constants P and P_0 that get as follows.

$$\|x(t)\| \le \frac{\mathrm{P}\|x_0\|}{1+\|A\|(t-t_0)^{\alpha}} + \int_{t_0}^{t}\frac{(t-\tau)^{\alpha-1}\mathrm{P}_0}{1+\|A\|(t-\tau)^{\alpha}}\|\Delta A(\tau)x(\tau)\|d\tau \tag{29}$$

Considering the assumption $|\xi_i - \xi_{i-1}| \le N|x_{(t)}|$ we have

$$\|\Delta A(t)x(t)\| \le \frac{1}{\mathrm{P}_0}\|x(t)\| \tag{30}$$

Substituting (30) into (29), we gets

$$\|x(t)\| \le \frac{\mathrm{P}\|x_0\|}{1+\|A\|(t-t_0)^{\alpha}} + \int_{t_0}^{t}\frac{(t-\tau)^{\alpha-1}}{1+\|A\|(t-\tau)^{\alpha}}\|x_{(\tau)}\|d\tau \quad ,(31)$$

By applying Lemma 2 on (31), results in:

$$\|x(t)\| \le \frac{\mathrm{P}\|x_0\|}{1+\|A\|(t-t_0)^{\alpha}} + \mathrm{P}\int_{t_0}^{t}\frac{(t-\tau)^{\alpha-1}\|x_0\|}{(1+\|A\|(\tau-t_0)^{\alpha})(1+\|A\|(t-\tau)^{\alpha})}\times \exp\left(\int_{\tau}^{s}\frac{(t-s)^{\alpha-1}ds}{(1+\|A\|(t-s)^{\alpha})}\right)d\tau = \frac{\mathrm{P}\|x_0\|}{1+\|A\|(t-t_0)^{\alpha}} + \mathrm{P}\int_{t_0}^{t}\frac{(t-\tau)^{\alpha-1}\|x_0\|}{(1+\|A\|(\tau-t_0)^{\alpha})(1+\|A\|(t-\tau)^{\alpha})^{\left(1-\frac{1}{\alpha\|A\|}\right)}} \le \frac{P\|x_0\|}{1+\|A\|(t-t_0)^{\alpha}} + \mathrm{P}\|x_0\|\|A\|^{\left(\frac{1}{\alpha\|A\|}-2\right)}\int_{t_0}^{t}(t-\tau)^{\frac{1}{\|A\|}-1}(\tau - t_0)^{-\alpha}d\tau = \frac{P\|x_0\|}{1+\|A\|(t-t_0)^{\alpha}} + \mathrm{P}\|x_0\|\|A\|^{\left(\frac{1}{\alpha\|A\|}-2\right)}\frac{\Gamma\left(\frac{1}{\|A\|}\right)\Gamma(1-\alpha)}{\Gamma\left(1+\frac{1}{\|A\|}-\alpha\right)}(t - t_0)^{\frac{1}{\|A\|}-\alpha} \tag{32}$$

Thus, when $t \to +\infty, \|x(t)\| \to 0$ for $\alpha\|A\| > 1$, that ensures the asymptotic stability of the system (16).

(b) assume $x^{(k)}(t_0) = x_k (k = 0,1)$ as initial conditions. Through the Laplace and Laplace inverse transform, the output of (16) is as follows.

$$x(t) = E_{\alpha,1}(A(t-t_0)^{\alpha})x_0 + (t-t_0)E_{\alpha,2}(A(t-t_0)^{\alpha})x_1 + \int_{t_0}^{t}(t-\tau)^{\alpha-1}E_{\alpha,\alpha}(A(t-\tau)^{\alpha})\Delta A(\tau)x(\tau))d\tau. \tag{33}$$

Lemma 1 says that there exist positive constants P_1, P_2, and P_3 such that

$$\|x(t)\| \le \frac{\mathrm{P}_1\|x_0\|}{1+\|A\|(t-t_0)^{\alpha}} + \frac{\mathrm{P}_2(t-t_0)\|x_1\|}{1+\|A\|(t-t_0)^{\alpha}} + \int_{t_0}^{t}\frac{\mathrm{P}_3(t-\tau)^{\alpha-1}}{1+\|A\|(t-\tau)^{\alpha}}\|\Delta A(\tau)x(\tau)\|d\tau \tag{34}$$

Considering the assumption $|\xi_i - \xi_{i-1}| \le N|x_{(t)}|$ we have

$$\|\Delta A(t)x(t)\| \le \frac{1}{\mathrm{P}_3}\|x(t)\| \tag{35}$$

Submitting (35) into (34), we gets

$$\|x(t)\| \le \frac{\mathrm{P}_1\|x_0\| + \mathrm{P}_2(t-t_0)\|x_1\|}{1+\|A\|(t-t_0)^{\alpha}} + \int_{t_0}^{t}\frac{(t-\tau)^{\alpha-1}}{1+\|A\|(t-\tau)^{\alpha}}\|\Delta A(\tau)x(\tau)\|d\tau \tag{36}$$

By applying Lemma 2 on (36), results in:

$$\|x(t)\| \le \frac{\mathrm{P}_1\|x_0\|+\mathrm{P}_2(t-t_0)\|x_1\|}{1+\|A\|(t-t_0)^{\alpha}} + \int_{t_0}^{t}\frac{(\mathrm{P}_1\|x_0\|+\mathrm{P}_2(t-t_0)\|x_1\|)(t-\tau)^{\alpha-1}}{(1+\|A\|(\tau-t_0)^{\alpha}(1+\|A\|(t-\tau)^{\alpha})}\times\exp\left(\int_{\tau}^{s}\frac{(t-s)^{\alpha-1}ds}{(1+\|A\|(t-s)^{\alpha})}\right)d\tau = \frac{\mathrm{P}_1\|x_0\|+\mathrm{P}_2(t-t_0)\|x_1\|}{1+\|A\|(t-t_0)^{\alpha}} + \int_{t_0}^{t}\frac{(\mathrm{P}_1\|x_0\|+\mathrm{P}_2(t-t_0)\|x_1\|)(t-\tau)^{\alpha-1}}{(1+\|A\|(\tau-t_0)^{\alpha})(1+\|A\|(t-\tau)^{\alpha})^{\left(1-\frac{1}{\alpha\|A\|}\right)}} \le \frac{\mathrm{P}_1\|x_0\|+\mathrm{P}_2(t-t_0)\|x_1\|}{1+\|A\|(t-t_0)^{\alpha}} + \mathrm{P}_1\|x_0\|\|A\|^{\left(\frac{1}{\alpha\|A\|}-2\right)}\frac{\Gamma\left(\frac{1}{\|A\|}\right)\Gamma(1-\alpha)}{\Gamma\left(1+\frac{1}{\|A\|}-\alpha\right)}(t - t_0)^{\frac{1}{\|A\|}-\alpha} + \mathrm{P}_2\|x_1\|\|A\|^{\left(\frac{1}{\alpha\|A\|}-2\right)}\frac{\Gamma\left(\frac{1}{\|A\|}\right)\Gamma(2-\alpha)}{\Gamma\left(2+\frac{1}{\|A\|}-\alpha\right)}(t - t_0)^{\frac{1}{\|A\|}-\alpha} \tag{37}$$

Therefore, if $(\alpha-1)\|A\| > 1$, then $\|x(t)\| \to 0$ as $t \to +\infty$, which implies that the system (16) is asymptotically stable.

C. External disturbances

Assume that there is a process disturbance d and measurement noise n as is illustrated in Fig. 2. In the system in Fig. 2 y is the process output and y_n denotes the measured signal. So for the signals y, y_n, and u we have:

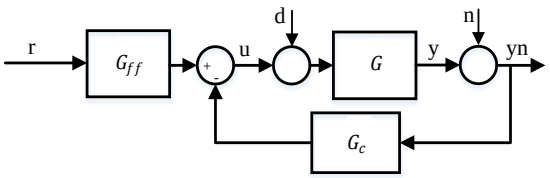

Fig 2. Block diagram of closed-loop system with load disturbance d and measurement noise n

$$\begin{aligned} Ay &= B(u+d) \\ y_n &= y+n \\ Ru &= Tr - Sy_n \end{aligned} \tag{38}$$

$$\begin{aligned} y &= \frac{BT}{AR+BS}r + \frac{BR}{AR+BS}d + \frac{BS}{AR+BS}n \\ y_n &= \frac{BT}{AR+BS}r + \frac{BR}{AR+BS}d + \frac{AR}{AR+BS}n \\ u &= \frac{AT}{AR+BS}r - \frac{BS}{AR+BS}d - \frac{AS}{AR+BS}n \end{aligned} \tag{39}$$

These equations show the effect of command signals and disturbances in the closed-loop system response separately. The design of the closed-loop system assumed always stable, so all the roots of characteristic polynomial $A_c = AR + BS$ is in the left half plane. The Diophantine algebraic problem is finding two polynomials $R_{(s)}$ and $S_{(s)}$ for given $A_{(s)}$, $B_{(s)}$, and $A_{c(s)}$ from one equation (3). The designer can consider the auxiliary constraints by choosing an appropriate polynomial and obtaining another one.

First, consider the low frequency load disturbance d is a step. To avoid that there is a steady-state error we must require that the static gain from the disturbance d to y_n is zero. This means that $\lim_{s\to 0} B_{(s)} R_{(s)} = 0$. If the process itself has a nonzero gain, s must be a factor of $R(s)$. Secondly, measurement noise is typically of high frequency. One way to make sure that measurement noise does not generate large signals is to require that the controller G_c have a low-pass filter nature. This means that measurement signals do not give any errors in the process variable. To summarize, the disturbances can be dealt with by introducing constraints on the polynomials R and S.

D. Model uncertainties

If we consider that the design of the controller is based on the nominal uncertain model$G$, true open-loop transfer function is $\hat{G}$; The closed-loop system will be T_{cl} and $\hat{T}_{cl}$ respectively.

$$T_{cl} = \frac{G_{ff}G}{1+G_cG} \tag{40}$$

$$\hat{T}_{cl} = \frac{G_{ff}\hat{G}}{1+G_c\hat{G}} \tag{41}$$

The sensitivity of closed-loop system respect to variations in G is given by

$$\frac{dT_{cl}}{dG} = \frac{G_{ff}}{(1+G_cG)^2} \tag{42}$$

The relative sensitivity of closed-loop system respect to G can be written as

$$\frac{dT_{cl}}{T_{cl}} = \frac{1}{1+G_cG}\frac{dG}{G} = \Gamma\frac{dG}{G} \tag{43}$$

The transfer function Γ is called sensitivity function and transfer function Δ is called complementary sensitivity.

$$\Gamma = \frac{1}{1+G_cG} \tag{44}$$

$$\Delta = 1 - \Gamma = \frac{G_cG}{1+G_cG} \tag{45}$$

The poles of the closed-loop system are the zeros of the function

$$\begin{aligned} f_{(s)} &= 1 + G_{c(s)}\hat{G}_{(s)} \\ &= 1 + G_{c(s)}\hat{G}_{(s)} + G_{c(s)}G_{(s)} - G_{c(s)}G_{(s)} \\ &= 1 + G_{c(s)}G_{(s)} + G_{c(s)}(\hat{G}_{(s)} - G_{(s)}) \end{aligned} \tag{46}$$

If in the left half plane

$$\left|G_{c(s)}(\hat{G}_{(s)} - G_{(s)})\right| \le |\,1 + G_cG| = \left|\frac{G}{T_{cl}}\right|\left|G_{ff}\right| \tag{47}$$

Then it follows from the principle of variation of the argument that the differences between the number of poles and zeros in right half plane for the function $1 + G_cG$ and $1 + G_c\hat{G}$ are the same. The relative precision needed for stability robustness is obtained by dividing by G_cG.

$$\left|\frac{\hat{G}-G}{G}\right| \le \left|\frac{1+G_c\hat{G}}{G_cG}\right| = \left|\frac{1}{\Delta}\right| \tag{48}$$

The complementary sensitive function thus makes it possible to determine bounds for stability robustness. The following theorem results.

Theorem 2: Consider the closed-loop systems T_{cl} and $\hat{T}_{cl}$ obtained from systems with transfer functions G and $\hat{G}$ I respectively. The system $\hat{T}_{cl}$ is stable if the following conditions are true:

1. T_{cl} is stable.

2. G and $\hat{G}$ have the same number of poles in right half plane.
3. The inequality (47) is fulfilled in left half plane.

The result shows that the designer must know the number of unstable modes in order to design a regulator for the system. The theorem is, however, conservative. The inequality (47) gives the frequency range in which it is important to have a good description of the process where $\hat{G}_{(s)} \approx 1$.

The transfer function of the closed-loop system given in (41) can also be written as bellows.

$$T_{cl} = \frac{1}{1 + 1/G_c\hat{G}} \tag{49}$$

The poles of the closed-loop system are thus the zeros of the function.

$$\begin{aligned} f_{(s)} &= 1 + \frac{1}{G_{c(s)}\hat{G}_{(s)}} \\ &= 1 + \frac{1}{G_{c(s)}\hat{G}_{(s)}} + \frac{1}{G_{c(s)}G_{(s)}} - \frac{1}{G_{c(s)}G_{(s)}} \end{aligned} \tag{50}$$

It follows from the principle of variation of the argument that the differences between the zeros and poles in right half plane of the functions $1 + \frac{1}{G_{c(s)}\hat{G}_{(s)}}$ and $1 + \frac{1}{G_{c(s)}G_{(s)}}$ are the same if in the left half plane

$$\left|\frac{1}{G_{c(s)}\hat{G}_{(s)}} - \frac{1}{G_{c(s)}G_{(s)}}\right| < \left|1 + \frac{1}{G_{c(s)}G_{(s)}}\right| \tag{51}$$

Theorem 3: Consider the closed-loop systems T_{cl} and $\hat{T}_{cl}$ obtained from transfer functions G and $\hat{G}$ respectively. The system $\hat{T}_{cl}$ is stable if the following conditions are true:

1. T_{cl} is stable.
2. G and $\hat{G}$ have the same number of zeros in right half plane.
3. The inequality (51) is fulfilled on the Im axe of complex plane.

The theorem shows that stability can be maintained in spite of large differences between G and Gˆ provided that the loop gain is large.

Based on theorems 2 and 3, to achieve robust stability based on an uncertain model the following rules are obtained.

- The designer must know the number of unstable poles and zeros.
- The designer must know the model precisely for those frequencies for which the loop gain can be made large.
- The designer must make the loop gain small for those frequencies for which the relative error $\frac{\Delta G}{G}$ is large.
- The designer must have a model that describes the system precisely for those frequencies for which $\hat{G} \approx -1$

IV. Simulation tests

The DC/DC converters that convert an unregulated input voltage to a regulated output voltage have an important role in energy storage systems to increase the efficiency of power conversion [25]. In recent studies, modeling of DC/DC converters in FO systems has been considered by many researchers. The following sample model is used for numerical example simulations on FO DC/DC buck converter [26] to show the efficiency of proposed method.

$$G_{(s)} = \frac{V_o}{D} = \frac{V_i}{L_\alpha C_\beta s^{\alpha+\beta} + \frac{L_\alpha}{R}s^{\alpha} + 1} \tag{52}$$

Where and α and β reflect the non-ideality of inductor and capacitor model and L_α and C_β is fractional order inductance and capacitance. The control signal D is input duty-cycle, V_o is output voltage and V_i is input voltage. The parameters considered as L=4.7 mH, C=10 mF, R=5 Ω, α=0.9, β=0.8 and V_i=1 V. Taking into account the desired response characteristics and the given actuator constraint $|D_{max}| = 1$ the desired system is assumed as follows.

$$G_{m(s,\zeta)} = \frac{1024\zeta^2}{s^2 + 64\zeta s + 1024\zeta^2} \tag{53}$$

Through this G_m, by $\zeta_0 = 1$ the fastest possible system regarding actuator constraint will be obtained.

A. The simulation structure

In the simulation structure Fig. 3, the controller is performed as a function, by selecting polynomial $S_{(s)} = 1/s + \frac{V_i}{1024\xi^2}$ and solving Diophantine equation (3), the controller's polynomials will be obtained as (54) and (55).

$$R = \frac{1024\xi^2 s^3 + (65536\xi^3 + L_\alpha C_\beta V_i)s^2 + (1024^2\xi^4 + 64V_i\xi)s}{L_\alpha C_\beta 1024\xi^2 s^{2.7} + \frac{L_\alpha}{R}1024\xi^2 s^{1.9} + L_\alpha C_\beta V_i s^{1.7} + \frac{L_\alpha}{R}V_i s^{0.9} + 1024\xi^2 s + V_i} \tag{54}$$

$$T = \frac{1024\xi^2}{V_i} \tag{55}$$

In performing SVSC schema, we got N=10 and decreasing step $s_D = 0.05$. By this design we have s-factor in the $R(s)$ cause to disappear low frequency step disturbance in steady-state, also, the controller G_c have low-pass filter nature, so it

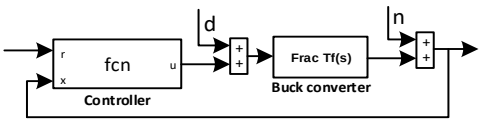

Fig 3. The simulation structure

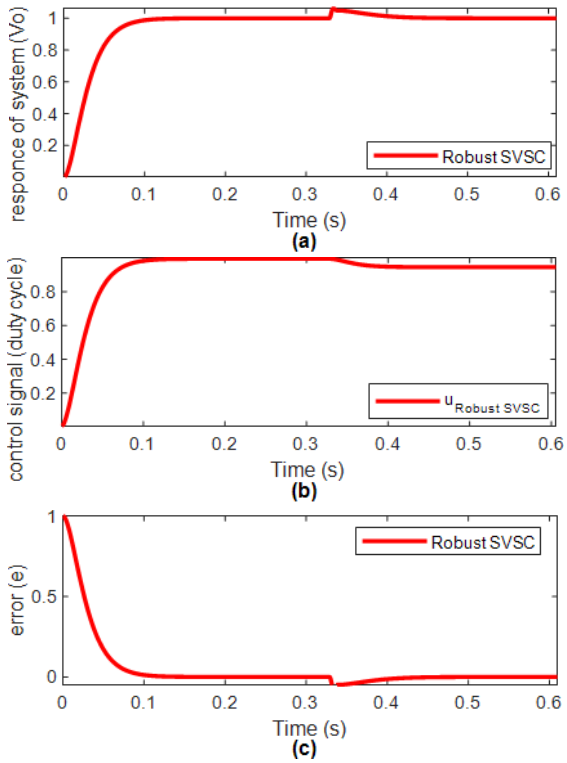

Fig 4. Output (a), control signal (b) and error (c) of the proposed controller in the presence of disturbance.

can eliminate the high frequency noise. Furthermore, by considering conditions in Theorem 2 and Theorem 3, the closed-loop system in the presence of model uncertainty will stay stable.

B. The simulation tests

a) In the presence of disturbance

In order to evaluate the controller in the presence of disturbance, the control system is affected by step load disturbance with amplitude $0.05|D_{max}| = 0.05$ in t=0.35s is shown in Fig. 4.

As a physical interpretation of Fig. 4, the disturbance deviation in the duty cycle is well compensated. It is illustrated that the control system has eliminated the effect of disturbance within an acceptable period of time and the control signal behaves smoothly within the actuator constraint range.

b) In the presence of model uncertainties

In this simulation case, the parameter of system $G_{(s)}$ is replaced by the values $a2 = 0.8a2$, $a1 = 0.82a1$, $and\ a0 = 0.78a0$ in time 0.35s. From a physical point of view, this case can be interpreted as changes in the value of electrical elements due to wear or environmental conditions.

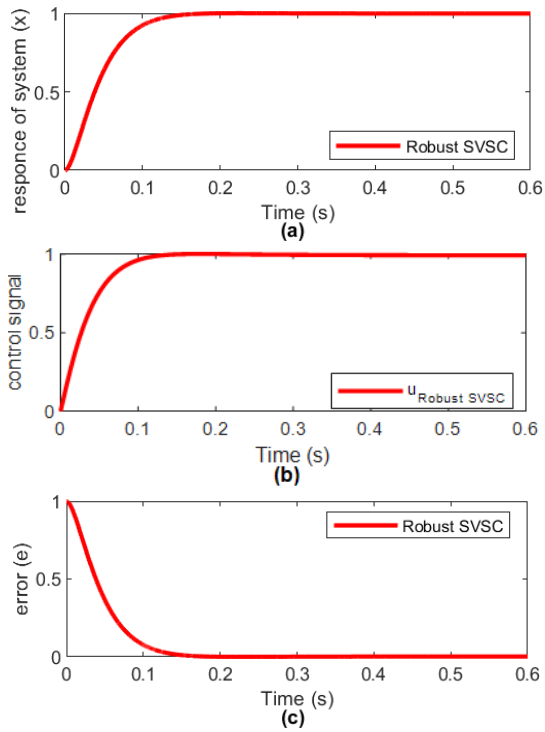

Fig 5. Output (a), control signal (b) and error (c) of the proposed controller in the presence of model uncertainty.

As is illustrated in Fig. 5, the controller has an acceptable performance in the presence of significant model uncertainty. There is no considerable effect on response and control signal of the system.

c) In the presence of noise, disturbance and model uncertainties

In the following case, In addition to disturbance and model uncertainties, the response signal is corrupted by measurement noise. The 29dB white Gaussian noise is added to measured signal, step load disturbance with amplitude 0.05 in t=0.35s and the parameter change as case b is forced to system. Fig. 5 shows the performance of the controller in this environment.

As can be seen, the performance in the presence of noise, disturbance and model uncertainties is satisfactory. The control system can tolerate the noise, disturbance and model uncertainties. There is no change in the settling time, and the control signal is smooth within the actuator constraint range.

d) Comparative results

To improve the results and discussions, a comparison with methods Fractional-order Sliding-Mode Control [27] and Fractional-order PID (FPID) [28] is presented. For these cases

the fractional sliding surface is selected as follows:

$$S = e^{(0.7)} + \lambda e, \quad (56)$$

Where λ=1; and parameters of the FPID selected thorough MATLAB SQP_ ITSE optimization ($P = 0.10,\ I = 22.08$

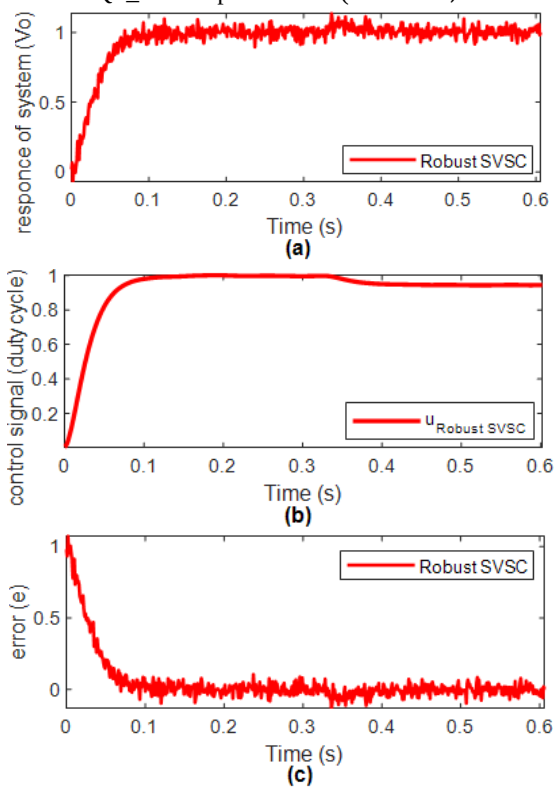

Fig 6. Output (a), control signal (b) and error (c) of the proposed controller in the presence of disturbance, model uncertainty and noise

Table 1.TABLE OF RESULTS

method	t_s	**u**max
Robust SVSC	0.15s	1.0 (by restriction)
FSMC	0.24s	1.0
FPID	0.41s	1.0

$\lambda = 0.78,\ D = 0.02,\ and\ \mu = 0.09$). Fig. 6 shows the comparative performance of the controllers. Table 1 summarizes the simulation results.

As is illustrated, the SMC is as fast as the proposed controller, and has good robustness against uncertainties; but the SMC is diagnosed with chattering, while the control signal of the proposed controller is smooth. Plus, there is no restriction barrier on the control signal in FSMC and FPID. By the initiative presented in this article, during the control period it exploits the maximum capacity of the actuator; and by selecting proper polynomials in controller design, the robust performance and robust stability against external disturbances and model uncertainties was obtained. Therefore, we could implement a faster controller while considering control signal constraints in the presence of model uncertainties and external disturbances. The control signal is soft and has no chattering.

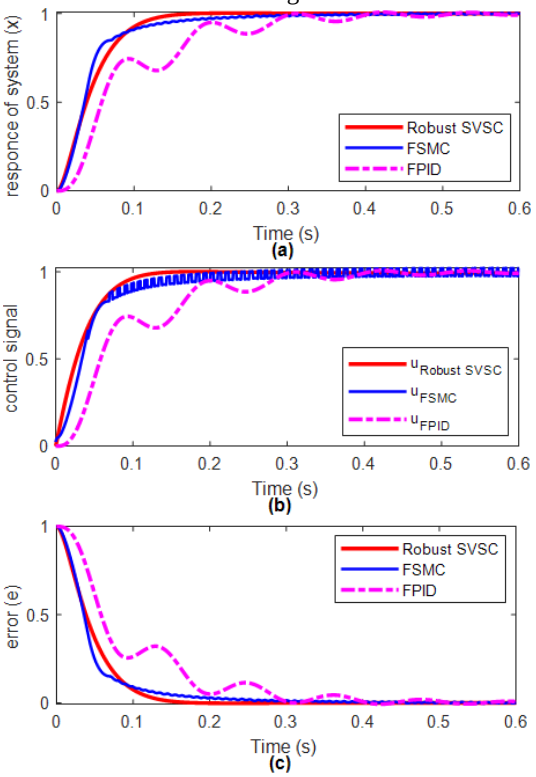

Fig 7. Comparison of the proposed controller with FSMC and FPID: response (a), the control signal (b), and error (c)

V. Conclusions

In this paper, the fractional-order floated pole controller as a fast and robust approach for the FO systems is proposed. The proposed robust variable structure control yields a continuous and constrained control signal, also a fast response in the presence of model uncertainties and external disturbances. In the proposed method, the pole placement algorithm is employed, the robust property added to the controller by designing proper polynomials, then due to a simple optimization routine it made fast and faster within the stability region. In the proposed robust system, a continuous and constrained control signal is get. The sufficient condition of stability is developed based on attributes of the Mittag-Leffler function and the stability theory of FOS. Numerical simulations and examples are done to demonstrate the effectiveness of the proposed method. As the future scope, the generalization of other SVSC methods to FO systems can be relevant. Also as a recommendation for the practical use of the proposed method in real life, the Oustaloup approximation and Hankel model order reduction techniques can be used for approximation to integer order systems and reduce the complexity of such high-order integer controllers, respectively.

References

[1] P. Warrier and P. Shah, "Fractional Order Control of Power Electronic Converters in Industrial Drives and Renewable Energy Systems: A Review," in IEEE Access, vol. 9, pp. 58982-59009, 2021, doi: 10.1109/ACCESS.2021.3073033.

[٢] Gholipour, R., Fateh, M.M. Robust Control of Robotic Manipulators in the Task-Space Using an Adaptive Observer Based on Chebyshev Polynomials. J Syst Sci Complex 33, 1360–1382 (2020). https://doi.org/10.1007/s11424-020-8186-0

[٣] Y. Chen, I. Petras, and D. Xue, ''Fractional order control—A tutorial,'' in Proc. Amer. Control Conf., Jun. 2009, pp. 1397–1411.

[٤] Batiha IM, Ababneh OY, Al-Nana AA, Alshanti WG, Alshorm S, Momani S. A Numerical Implementation of Fractional-Order PID Controllers for Autonomous Vehicles. Axioms. 2023 Mar 17;12(3):306.

[٥] Zamani AA, Etedali S. Seismic structural control using magneto-rheological dampers: A decentralized interval type-2 fractional-order fuzzy PID controller optimized based on energy concepts. ISA transactions. 2023 Feb 7.

[٦] S. Pandey, P. Dwivedi, and A. S. Junghare, ''A novel 2-DOF fractional-order PI λ – D μ controller with inherent anti-windup capability for a magnetic levitation system,'' AEU-Int. J. Electron. Commun., vol. 79, pp. 158–171, Sep. 2017.http://www.sciencedirect.com/science/article/pii/S1434841117301905

[7] P. Shah and S. Agashe, ''Review of fractional PID controller,'' Mechatronics, vol. 38, pp. 29–41, Sep. 2016. http://www.sciencedirect.com/science/article/pii/S095741581630068X

[8] Chen Y, Tang C, Roohi M. Design of a model-free adaptive sliding mode control to synchronize chaotic fractional-order systems with input saturation: An application in secure communications. Journal of the Franklin Institute. 2021 Oct 1;358(16):8109-37.

[9] Mohammad Ghamgosar, Seyed Mehdi Mirhosseini-Alizamini, Mahmood Dadkhah, Design of Optimal Sliding Mode Control based on Linear Matrix Inequality for Fractional Time-Varying Delay Systems, International Journal of Industrial Electronics, Control and Optimization (IECO), Volume 5, Issue 4 , December 2022, , Pages 317-325, https://doi.org/10.22111/ieco.2022.42132.1423 ..

[10] Rouhani SH, Mojallali H, Baghramian A. Load frequency control in the presence of simultaneous cyber-attack and participation of demand response program. Transactions of the Institute of Measurement and Control. 2022 Jun;44(10):1993-2011.

[11] Shokoohinia, M.R., Fateh, M.M. & Gholipour, R. Design of an adaptive dynamic sliding mode control approach for robotic systems via uncertainty estimators with exponential convergence rate. SN Appl. Sci. 2, 180 (2020). https://doi.org/10.1007/s42452-020-1947-5.

[12] Chen SB, Beigi A, Yousefpour A, Rajaee F, Jahanshahi H, Bekiros S, Martínez RA, Chu Y. Recurrent neural network-based robust nonsingular sliding mode control with input saturation for a non-holonomic spherical robot. IEEE access. 2020 Oct 13;8:188441-53.

[13] Wang YL, Jahanshahi H, Bekiros S, Bezzina F, Chu YM, Aly AA. Deep recurrent neural networks with finite-time terminal sliding mode control for a chaotic fractional-order financial system with market confidence. Chaos, Solitons & Fractals. 2021 May 1;146:110881.

[14] Dipayan Guha, Provas Kumar Roy, Subrata Banerjee, Adaptive fractional-order sliding-mode disturbance observer-based robust theoretical frequency controller applied to hybrid wind–diesel power system, ISA Transactions, 2022, ISSN 0019-0578, https://doi.org/10.1016/j.isatra.2022.06.030.

[15] S. Hou, Y. Chu, and J. Fei, ''Intelligent global sliding mode control using recurrent feature selection neural network for active power filter,'' IEEE Trans. Ind. Electron., early access, Jun. 12, 2020, doi: 10.1109/TIE.2020.3000098.

[16] J. Wang, W. Luo, J. Liu, and L. Wu, ''Adaptive type-2 FNN-based dynamic sliding mode control of DC–DC boost converters,'' IEEE Trans. Syst., Man, Cybern. Syst., vol. 51, no. 4, pp. 2246–2257, Apr. 2021.

[17] Shengzheng Kang, Hongtao Wu, Xiaolong Yang, Yao Li, Liang Pan, Bai Chen, Fractional robust adaptive decoupled control for attenuating creep, hysteresis and cross coupling in a parallel piezostage, Mechanical Systems and Signal Processing, Volume 159, 2021, 107764,ISSN 0888-3270, https://doi.org/10.1016/j.ymssp.2021.107764.

[18] Kaheni M, Zarif MH, Kalat AA, Fadali MS. Soft variable structure control of linear systems via desired pole paths. Information Technology and Control/Informacinės technologijos ir valdymas. 2018 Sep 10;47(3):447-56.

[19] Abbaszadeh E, Haddad-Zarif M. Soft variable structure control of linear fractional-order systems with actuators saturation. ISA transactions. 2022 Mar 10.

[20] Åström KJ, Wittenmark B. Computer-controlled systems: theory and design. Courier Corporation; 2013 Jun 13.

[21] Tabatabaei M, Haeri M. Characteristic ratio assignment in fractional order systems. ISA transactions. 2010 Oct 1;49(4):470-8.

[22]Rasouli H, Fatehi A, Zamanian H. Design and implementation of fractional order pole placement controller to control the magnetic flux in Damavand tokamak. Review of Scientific Instruments. 2015 Mar 10;86(3):033503.

[23] Junior FA, Bessa I, Pereira VM, da Silva Farias NJ, de Menezes AR, de Medeiros RL, Chaves Filho JE, Lenzi MK, da Costa Júnior CT. Fractional Order Pole Placement for a buck converter based on commensurable transfer function. ISA transactions. 2020 Dec 1;107:370-84.

[24] Zúñiga-Aguilar CJ, Gómez-Aguilar JF, Romero-Ugalde HM, Escobar-Jiménez RF, Fernández-Anaya G, Alsaadi FE. Numerical solution of fractal-fractional Mittag–Leffler differential equations with variable-order using artificial neural networks. Engineering with Computers. 2021:1-4.

[25] Sivakumar S, Sathik MJ, Manoj PS, Sundararajan G. An assessment on performance of DC–DC converters for renewable energy applications. Renewable and Sustainable Energy Reviews. 2016 May 1;58:1475-85.

[26] Ahmed G. Radwan, Ahmed A. Emira, Amr M. AbdelAty, Ahmad Taher Azar, Modeling and analysis of fractional order DC-DC converter,ISA Transactions, Volume 82, 2018, Pages 184-199, ISSN 0019-0578, https://doi.org/10.1016/j.isatra.2017.06.024.

[27] Pouzesh M, Mobayen S. Event-triggered fractional-order sliding mode control technique for stabilization of disturbed quadrotor unmanned aerial vehicles. Aerospace Science and Technology. 2022 Feb 1;121:107337.

[28] Zamani AA, Etedali S. Optimal fractional-order PID control design for time-delayed multi-input multi-output seismic-excited structural system. Journal of Vibration and Control.

2023 Feb;29(3-4):802-19.

Ebrahim Abbaszadeh-Soorami is a Ph.D. candidate in Control Engineering, in the Department of Electrical and Robotics, Shahrood university of technology, I.R.Iran. He received his B.Eng. in Electrical-Electronic Engineering, from Azad University branch Lahidjan, I.R.Iran, in 2008 and M.Sc. in Electrical-Control Engineering, from the Shahrood University of Technology, Shahrood, I.R. Iran, in 2013.
Mr. Abbaszadeh's research interests include robotic control, computer numerical control machining, applied computational geometry, fractional-order systems, and discrete-event computer simulation.

Mohammad Haddad-Zarif is Associate Professor of Control Engineering at Shahrood University of Technology, Shahrood, I.R. Iran.
Dr. Haddad-Zarif's research interests include optimal control, robotic control, and applied computational geometry.

IECO

This page intentionally left blank.

International Journal Of
Industrial Electronics Control and Optimization
Print ISSN: 3517-2645
Online ISSN: 3568-2645
Homepage: https://ieco.usb.ac.ir/

Synchronization Control Strategy of Inverted Pendulums using Control Law Partitioning and Contraction Theory

Rogayyeh Soltani[1] | Bashir Naderi[1] | Saeed Nezhadhossein[1] | Aghileh Heydari[1]

Department of Mathematics, Payame Noor University, Tehran, Iran [1]
Corresponding author's email: b_naderi@pnu.ac.ir

Article Info

Article type:
Research Article
Article history:
Received: 2023-March-15
Revised: 2023-Jun-14
Accepted: 2023 – July- 1
Published online: 2023-July-1
Keywords:
Contraction Theory,
Synchronization Control,
Inverted Pendulum,
Cart and Pole.

ABSTRACT

A synchronization balancing control is proposed based on the contraction theory of stability. The control scheme is applied to balance an inverted pendulum mounted on a moving cart with two wheels. The equations of motion of the system are divided into two cascade systems using the control law partitioning method, which allows the designer to split the control design process into simpler parts for each isolated fragment of the system. Then two control laws are proposed for the corresponding partitions. The main aim of the closed-loop system is to balance the pendulum and synchronize the transient behavior of the system state with a reference model with time-varying parameters. The stability is guaranteed using the contraction theory. The proposed control mechanism is investigated through simulation and comparison studies, and the results confirm the performance and superiority of the proposed controller.

Nomenclature

x	State vector of system, $\mathbb{R}^{n\times 1}$	g	Gravity, $\mathbb{R}$
$f(.,.)$	Continuously differentiable function, $\mathbb{R}^{n\times 1}$	τ_R, τ_L	Right and left wheel torque, $\mathbb{R}$
$\partial/\partial x$	Partial differentiation with respect to x	τ_B	Applied torque to the pendulum joint, $\mathbb{R}$
δx	Perturbed variation to x	τ	Summation of the right and left wheel torque, $\mathbb{R}$
$J(x,t)$	Jacobian matrix of the system, $\mathbb{R}^{n\times n}$	θ	The rotational angle of the pendulum, $\mathbb{R}$
J_{sym}	The symmetric part of the Jacobian matrix, $\mathbb{R}^{n\times n}$	u	The output of the linear portion of the system, $\mathbb{R}$
λ_{max}	The largest eigenvalue of J_{sym}, $\mathbb{R}$	α_i, β_i, ξ	The defined parameter in Equs (14) and (15), $\mathbb{R}$
$I_{n\times n}$	The dimensional identity matrix, $\mathbb{R}^{n\times n}$	ψ	The defined variable based on the reference, $\mathbb{R}$
$\|.\|$	The Euclidian norm	m_B	Body weight, 1.2 kg
μ	A real positive fix constant, $\mathbb{R}$	m_W	Wheel weight, 0.02 kg
$\varphi(x,t)$	Transition matrix, $\mathbb{R}^{n\times n}$	I_B	Body inertia, 0.015 kgm^2
z	Generalized state vector, $\mathbb{R}^{n\times 1}$	I_W	Wheel inertia, 0.00002 kgm^2
M	A square symmetric metric, $\mathbb{R}^{n\times n}$	I_M	Rotor inertia, 0.000001 kgm^2
$F(x,t)$	Generalized Jacobian matrix, $\mathbb{R}^{n\times n}$	I_G	Gearbox inertia, 0.0001 kgm^2
X	The state vectors of the system, $\mathbb{R}^{n\times 1}$	b_M	Motor damping, 0.001 Nms/rad
Y	The state vector of the reference system, $\mathbb{R}^{n\times 1}$	b_W	Wheel damping, 0.001 Nms/rad
γ_i	Time-variant coefficients of the reference system, $\mathbb{R}$	b_G	Gearbox damping, 0.001 Nms/rad
e_i	synchronization error, $\mathbb{R}$	n	Gearbox ratio, 30
z_i	Generalized synchronization error variable, $\mathbb{R}$	r	Wheel diameter, 0.032 m
z_i^{ref}	a virtual desired value for z_i, $\mathbb{R}$	l	COG distance, 0.075 m
E	Error vector of synchronization system, $\mathbb{R}^{n\times 1}$	R	Armature resistance, 2.4 Ω
Z	Generalized Error vector of system, $\mathbb{R}^{n\times 1}$	K	Motor constant, 0.01 Nm/A
η_i	The desired dynamics design parameters	ζ_i	Design parameters of the error system dynamics

I. Introduction

Background: An Inverted Pendulum (IP) is a principal benchmark for control systems. IP Balancing control has been studied for decades due to its role in many other sciences, including the rocket's vertical take-off [1], biped robot walking analysis and control [2], self-balancing robot [3], dynamics of human sagittal balance [4], prosthetic finger robust controller design [5], lower limb rehabilitation robot [6], running trajectory generation [7], development of biomechanical gait analysis [8], dynamic walking of legged robots [9]. This wide range of applications makes the inverted pendulum an attractive research area, from theoretical analysis to practical control system design. Moreover, synchronization control is an active research area. Lyapunov stable fractional-order sliding mode controller with time-varying switching surface and without the reaching phase is proposed in [10]. Impulsive synchronization in fractional-order complex-valued reaction-diffusion networked systems based on the Lyapunov function, finite-time Mittag-Leffler criteria, and linear matrix inequalities (LMIs) as a cryptosystem is introduced in [11].

Literature review: In 2002, a moving IP as an archetype of a two-wheeled robot was presented [12]. As a result of its two coaxial wheels connected to two DC motors, the vehicle can turn without transitional motion. The controller was created with two state-space controllers connected to DC motors that drive the wheels by an isolation unit. In 2005, Ibanez et al. offered a nonlinear controller to balance an IP, which utilized partial feedback linearization [13]. The inverse pendulum excitation coordinates were linearized first, and then a Lyapunov-like function was designed to gain a stable feedback controller. In 2006, Muskinja and Tovornik developed an adaptive state controller to stabilize and optimally balance an IP, in which a switching mechanism between the swing and balance algorithm has been proposed [14]. In 2011, the optimal control of the nonlinear dynamic system of IP was proposed, using LQR and PID controllers [15]. In 2018, Khoshroo et al. designed a reinforcement learning controller based on the robust quadratic linear controller (LQR) for a four-degree-of-freedom inverted pendulum [16]. In 2018, Irfan proposed a robust control mechanism and compared it with time-dependent linear and nonlinear control methods, energy-based methods, and tracking controllers, to confirm the efficiency of IP control systems [17]. In 2018, Franco et al. introduced a balancing control mechanism for a kind of flexible IP, which was robust against external disturbances. In addition, a method was developed to identify the dominant parameters that impact the robustness of the closed-loop system [18]. In 2019, Hamza et al. used a rotational IP as a point of reference for a comparative study of different control methods, such as oscillation control, stabilization control, switching control, and path tracking control. Finally, they proposed a new general system for testing higher-order intelligent controllers [1]. In 2020, Johnson et al. implemented a perceptual controller for an IP on a cart. Perceptual control theory roots in a theory that says "behavior is the control of perception." A unique feature of this controller is facing external disturbance [19]. In 2023, stabilization of an IP on a cart with cart position feedback was considered in [20]. Stable and proper compensators are not able to stabilize such a system. Therefore, the paper suggested utilizing an additional compensator in a parallel feedforward loop. The suggestion brought up a high sensitivity to noise. In 2023, two reinforcement learning algorithms, i.e. basic Q-Learning and Deep Q-Networks, were utilized to balance an IP without mathematical model requirement [21]. The attained advantage was the practical applicability of the method. However, the disadvantages of it were the time required for training the controller and the complexity of the approach. An adaptive fuzzy fast terminal sliding mode controller was detailed in [22] to balance an IP on a cart in the presence of uncertainties and actuator faults. The method succeeded in balancing the IP while compensating for the imperfections with a fast transient response. However, the design procedure and stability proof analysis were complicated. A mathematical controller was designed for an IP based on Taylor expansion, fourth-order Runge–Kutta, and multiple time-scale perturbation techniques [23]. The linearized stability has been proven based on Routh–Hurwitz criterion. However, the difficulty of the design process, linearized stability, and sensitivity to uncertainties were the drawbacks of the method.

Research gap and motivation: However, the main issue in the control design is stability. The second method of Lyapunov for stability explicitly necessitates defining or finding a function as a distance metric. This metric function must be decreasing over time for guaranteed stability. In order to find this function, the system must have specific characteristics in its structure or involve implicit optimization. To solve this problem, contraction theory utilizes a differentially constructed distance function that is not explicitly defined [24]. The only required property for constructing the contraction metric is the stabilizability of the under-control system, or in other words, the existence of the control signal [24], [25]. This generalization enables the contraction metric to be applied to underactuated systems. The other wide usage of the contraction theory is in transfer learning, in which a controller is designed for a typical system and must be tuned to work in the presence of uncertainty or parameter variations [24]. The contraction metric measures the convergence of two systems' trajectories [26]. Contraction theory, as stated in [27]-[29], is a study of the convergence of all nearby trajectories to a nominal motion. Therefore, this differential analysis is much simpler than what happened in Lyapunov's theory. A "contracting nonlinear dynamical system" is a term assigned to a system that exponentially

forgets its initial conditions or external disturbances and returns to its nominal trajectory fast [26]. The stability is different from the specific trajectory, which this fact is applied to the control designing process. In order to convergence checking, contraction theory utilized the neighboring system trajectories' local analysis [25]. For example, synchronization condition based on the contraction analysis is developed in [26], [30].

Challenges: The existing synchronization methods are trapped in high run-time computational cost or hard controller design procedure when seeking high accuracy, e.g. fractional order controllers or iterative methods ([11], [20]-[23]), or have lost the analysis of convergence whenever they proposed a simple controller, e.g. linear stable controller proposed in [31]. Finding the second derivative of the Lyapunov-like functions to prove stability is a complex task. Therefore, some methods suffer from the lack of guaranteed stability. In addition, the contraction-based synchronization controllers are applied to fully actuated systems, where the symmetric part of the Jacobian matrix is uniformly negative definite. However, in the underactuated systems, the symmetric part of the Jacobian matrix may not be uniformly negative definite. Here, the asymptotic convergence of such systems is studied. Moreover, time-varying parameters in the reference model are less studied in the literature.

Contributions: The contributions of this research can be listed as follows. (I) A balancing controller is designed for a benchmark, a two-wheeled self-balancing inverted pendulum robot, using a contraction-based synchronization procedure inspired by the works of [26] and [30]. (II) Time-varying parameters are considered for the synchronization reference model, which is different from the parameters of the under-control system, whereas in [26] and [30], the parameters of the reference model are time-invariant, and their values are as same as those of the under-control system. (III) In addition, the under-control system is underactuated, so the symmetric part of its Jacobian matrix is not uniformly negative definite. (IV) The exponential convergence of the generalized state variables to zero and the asymptotic stability of the closed-loop synchronization system are guaranteed. (V) Control law partitioning is utilized to separate the control design process into two simpler mechanisms, the linear control portion (with a perfect control design based on transfer function) and the synchronization control law (which provides an underactuated affine system). (VI) the main achievements of the proposed control method are ease of design, low runtime computational cost, guaranteed stability with exponential convergence, adjustable desired transient response, small synchronization error, and the ability of experimental implementation due to its simplicity. These specifications make the proposed method applicable to control fast dynamics including biped walking robots, human gait and running balance, or rehabilitation robotics.

Paper organization: In this paper, Section 2 briefly introduces the contraction theory. Then in Section 3, we present the equations of motion of the two-wheeled IP system. In Section 4, we propose a control law partitioning method in combination with contraction theory based on synchronization applied to the balancing control. Section 5 investigates the performance of the proposed controller through simulation and comparison studies (compared with the method proposed in [32]). The conclusion is stated in Section 6.

II. Preliminaries

In this section, the fundamental definitions of the contraction theory are formulated [26], [27]. Then we will briefly discuss the generalized distance measure, generalized eigenvalue analysis, and the control law partitioning approach.

E. Contraction Theory

Let's consider an autonomous nonlinear dynamical system,

$$\dot{x} = f(x,t), \tag{1}$$

in which, $f(.,.)$ is an $n \times 1$ continuously differentiable vector function and $x \in \mathbb{R}^{n\times 1}$is the state vector of system. If the system's state vector is perturbed by an infinitesimal shift of δx, also termed virtual displacement, then based on the concept of virtual dynamics, the first variation of the system will be as follows [26]:

$$\delta\dot{x} = \frac{\partial f(x,t)}{\partial x}\delta x\,. \tag{2}$$

Equation (2) determines the way the system reacts to the virtual displacement in the future. In other words, the variation in the trajectory, which is due to the infinitesimal shift in the initial value, is investigated by the virtual dynamic theory. Therefore, there are two different trajectories, including nominal (x) and perturbed $(x+\delta x)$. The quadratic distance between these two neighboring trajectories can be measured with $\delta x^T\delta x$. The behavior of convergence/divergence between the trajectories can be studied through their quadratic distance as follows:

$$\frac{d}{dt}(\delta x^T\delta x) = 2\delta x^T\delta\dot{x} = 2\delta x^T\frac{\partial f(x,t)}{\partial x}\delta x\,. \tag{3}$$

If $J(x,t) = \partial f/\partial x$ is the Jacobian matrix of the system and $J_{sym} = \frac{1}{2}\left(\frac{\partial f(x,t)}{\partial x} + \frac{\partial f(x,t)}{\partial x}^T\right)$ is its symmetric part, then $\lambda_{max}(x,t)$ is the largest eigenvalue of J_{sym} such that $\frac{\partial f(x,t)}{\partial x} \le \lambda_{max}(x,t)I_{n\times n}$. Therefore,

$$\frac{d}{dt}(\delta x^T\delta x) \le 2\lambda_{max}(x,t)(\delta x^T\delta x)\,. \tag{4}$$

Then, it can be proved that

$$\|\delta x(t)\| \le \|\delta x(0)\| e^{\int_0^t \lambda_{max}(x,t)dt}\,. \tag{5}$$

According to the $\lambda_{max}(x,t)$, the converging system is defined in [27] as follows.

Remark 1: Every infinitesimal perturbation, $\|\delta x\|$, will exponentially converge to zero if $\lambda_{max}(x,t)$ is strictly uniformly negative, which means that

$$\exists\mu > 0, \forall x, \forall t > 0 \rightarrow \lambda_{max}(x,t) \le -\mu. \tag{6}$$

Based on remark 1, when the Jacobian matrix, $J(x,t)$, is uniformly negative definite in a region, the system is termed "contracting" in that region [26], [27].

Remark 2: If a system is contracting in whole state space, then global exponential convergence of the perturbed

trajectories to the nominal trajectory is guaranteed [26]. Hence, the system is contracting if

$$\exists \mu > 0, \forall x, \forall t > 0 \rightarrow J_{sym} \leq -\mu I_{n\times n} < 0\,. \quad (7)$$

Fig. 1 shows the concept of trajectory perturbation, distance, and convergence. The above-mentioned concept is the basis of contraction theory.

F. Distance measure generalization

If we generalize the distance definition, we can widely generalize the contraction theory. The generalized distance can be explained by the differential coordination transition as

$$\delta z = \varphi(x,t)\delta x, \quad (8)$$

in which, $\varphi(x,t)$ is a transition matrix, such that $M = \theta^T\theta$ is a square symmetric differential continuous metric. This transition leads to a generalization of distance and the quadratic distance $\delta z^T\delta z = \delta x^T M \delta x$. The convergence of δz to zero brings the convergence of δx to zero [26].

G. Generalized eigenvalue analysis

Time derivative of (8) is

$$\begin{aligned}\frac{d}{dt}\delta z &= \dot{\varphi}(x,t)\delta x + \varphi(x,t)\frac{d}{dt}\delta x \\ &= \left(\dot{\varphi} + \varphi\frac{\partial f}{\partial x}\right)\varphi^{-1}\delta z = F(x,t)\delta z,\end{aligned} \quad (9)$$

in which, $F(x,t) = \left(\dot{\varphi} + \varphi\frac{\partial f}{\partial x}\right)\varphi^{-1}$ is the generalized Jacobian matrix. Therefore,

$$\frac{d}{dt}(\delta z^T\delta z) = 2\delta z^T\frac{d}{dt}\delta z = 2\delta z^T F(x,t)\delta z\,. \quad (10)$$

As before, if $F(x,t)$ is strictly negative definite, then the convergence of δz, and consequently δx, to zero is guaranteed. Here, we used contraction theory to synchronize two nonlinear systems [26].

H. Control Law Partitioning

Designing a controller for a complex nonlinear system is a complicated task. Control Law Partitioning (CLP) approach departs the control law into two portions to simplify the control design procedure. The most famous CLP method dissects the control law into a model-based controller and the servo feedback [33], [34]. The model-based control law transforms the system into a unit mass for the servo controller [33], [34]. There are other kinds of CLP, for example, layered architecture [29], [35], where the controller is partitioned based on the task. Here, we utilize CLP to separate the system's model into a transfer function and a simple affine system.

III. System Modeling and Control Law Partitioning

This section describes the mathematical model of the two-wheeled self-balancing robot or simply an inverted pendulum attached to a two-wheeled moving cart [3]. The schematic of the system is drawn in Fig. 2.

A. Dynamical Model of the System

The mathematical model of the system is described as:

$$\left(m_B + 2m_w + 2\frac{I_w}{r^2}\right)\ddot{p} + 2\frac{b_w}{r^2}\dot{p} + m_B l\ddot{\theta} = \frac{1}{r}(\tau_R + \tau_L) \quad (11.a.)$$

$$m_B l\ddot{p} + (m_B l^2 + I_B)\ddot{\theta} - m_B lg\theta = -(\tau_R + \tau_L) \quad (11.b.)$$

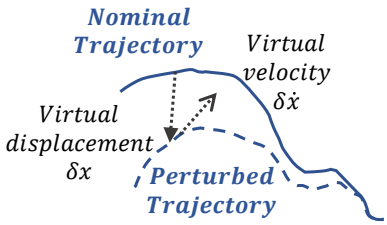

Fig. 1. The concept of neighboring trajectories, virtual displacement, distance, and convergence

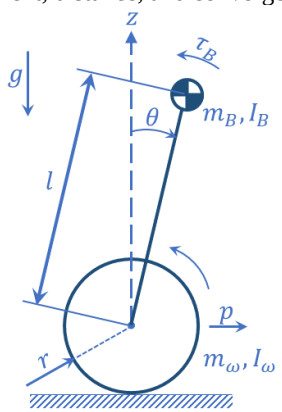

Fig. 2. Schematic of the dynamical system (two-wheeled self-balancing robot driven by dc gear motors) [3]

It is assumed that small movements of the cart (p) along axis x cause a neglectable deviation in the rotational angle of the pendulum, θ, [3]. In other words, when the cart is moving along x direction $\dot{\theta} \approx 0$ and $\cos(\theta) \approx 1$. Here, τ_B, τ_R, and τ_L are the applied torque to the pendulum joint and right and left wheels torques, respectively. Parameters of the system are selected as described in the nomenclature section.

Defining $\tau = \tau_R + \tau_L$, based on (11.b.) the cart acceleration $\ddot{p}$ can be computed.

$$\ddot{p} = -\left(l + \frac{I_B}{m_B l}\right)\ddot{\theta} + g\theta - \frac{1}{m_B l}\tau\,. \quad (12)$$

Substituting (12) in (11.a.), the following equation will be obtained.

$$\begin{aligned}&\left(m_B^2 l^2 - \left(m_B + 2m_w + 2\frac{I_w}{r^2}\right)(m_B l^2 + I_B)\right)\ddot{\theta} \\ &\quad - \left(2\frac{b_w}{r^2}(m_B l^2 + I_B)\right)\dot{\theta} \\ &\quad + \left(\left(m_B + 2m_w + 2\frac{I_w}{r^2}\right)m_B lg\right)\theta \\ &\quad + \left(2m_B lg\frac{b_w}{r^2}\right)\int_0^t \theta dt \\ &= \left(\frac{m_B l}{r} + \left(m_B + 2m_w + 2\frac{I_w}{r^2}\right)\right)\tau \\ &\quad + \left(2\frac{b_w}{r^2}\right)\int_0^t \tau dt\,.\end{aligned} \quad (13)$$

For the sake of simplicity, we rename the constant coefficients as below,

$$\begin{cases} \beta_1 = -\xi^{-1}\left(2m_B lg\dfrac{b_w}{r^2}\right), \\ \beta_2 = -\xi^{-1}\left(\left(m_B + 2m_w + 2\dfrac{I_w}{r^2}\right)m_B lg\right), \\ \beta_3 = \xi^{-1}\left(2\dfrac{b_w}{r^2}(m_B l^2 + I_B)\right), \\ \alpha_1 = \xi^{-1}\left(\dfrac{m_B l}{r} + \left(m_B + 2m_w + 2\dfrac{I_w}{r^2}\right)\right), \\ \alpha_2 = \xi^{-1}\left(2\dfrac{b_w}{r^2}\right), \end{cases} \quad (14)$$

in which,

$$\xi = \left(m_B^2 l^2 - \left(m_B + 2m_w + 2\frac{I_w}{r^2}\right)(m_B l^2 + I_B)\right). \quad (15)$$

Therefore, the equation of motion is rewritten.

$$\ddot{\theta} - \beta_3\dot{\theta} - \beta_2\theta - \beta_1\int_0^t \theta dt = \alpha_1\tau + \alpha_2\int_0^t \tau dt\,. \quad (16)$$

The main aim of the controller design procedure is to find the control signal, τ, such that the dynamical system behaves desirably.

B. Control Design Partitioning

In order to simplify the control design process, we proposed using "Control Law Partitioning," in which the obtained equation of motion can be divided into two cascade systems. Therefore, two control laws will be designed separately. In fact, the designed controller consists of two parts, a Synchronization Control Law (SCL) and a first-order Linear Control Portion (LCP). To simplify the control design process, we propose the linear portion of the system as below:

$$u = \alpha_1\tau + \alpha_2\int_0^t \tau dt\,. \quad (17)$$

Equation (17) is a first-order differential equation with constant coefficients. Therefore, τ can be easily found according to the new control signal, u. The proposed Linear Control Portion (LCP) is designed based on (17), as below:

$$\frac{\tau(s)}{u(s)} = \frac{s}{\alpha_1 s + \alpha_2}. \quad (18)$$

Since the angular position of the inverted pendulum is important to be synchronized with a desired reference system, one can define the state variables of the system as $X_1 = \int_0^t \theta dt$, $X_2 = \theta$, and $X_3 = \dot{\theta}$, the state vector as $X = [X_1, X_2, X_3]^T$, and the state space as below:

$$\begin{cases} \dot{X}_1 = X_2\,, \\ \dot{X}_2 = X_3\,, \\ \dot{X}_3 = \beta_1 X_1 + \beta_2 X_2 + \beta_3 X_3 + u\,. \end{cases} \quad (19)$$

Therefore, (19) is the synchronizing portion of the system. In the next section, we will formulate the control design process for (19).

IV. Contraction-based Synchronization

In this section, we proposed a Synchronization Control Law (SCL) based on the contraction theory [26]. First of all, a desired reference system is introduced as:

$$\begin{cases} \dot{Y}_1 = Y_2\,, \\ \dot{Y}_2 = Y_3\,, \\ \dot{Y}_3 = \gamma_1 Y_1 + \gamma_2 Y_2 + \gamma_3 Y_3\,, \end{cases} \quad (20)$$

in which, $Y = [Y_1, Y_2, Y_3]^T$ is the state vector of the reference system, and γ_1, γ_2 and γ_3 are (time-variant/invariant) coefficients of the reference system, which are adjusted for achieving the desired transient response. In this paper, we utilized time-variant coefficients for the reference model. Synchronization error is defined as $e_1 = X_1 - Y_1$, $e_2 = X_2 - Y_2$, and $e_3 = X_3 - Y_3$. By subtracting (20) from (19), we have:

$$\begin{cases} \dot{e}_1 = e_2\,, \\ \dot{e}_2 = e_3\,, \\ \dot{e}_3 = \beta_1 e_1 + \beta_2 e_2 + \beta_3 e_3 + \psi + u\,, \end{cases} \quad (21)$$

in which, $\psi = (\beta_1 - \gamma_1)Y_1 + (\beta_2 - \gamma_2)Y_2 + (\beta_3 - \gamma_3)Y_3$. Now, the control law will be designed through three steps based on the contraction theory. We define a new variable $z_1 \triangleq e_1$. Considering a desired dynamic of z_1 as $\dot{z}_1^{ref} = -\eta_1 z_1$, in which z_1^{ref} is a virtual desired value for z_1, and comparing with its actual dynamics $\dot{z}_1 = \dot{e}_1 = e_2$, a desired value for e_2 is obtained as $e_{2d} = -\eta_1 z_1$. Here, a new conceptual error is defined as:

$$z_2 \triangleq e_2 - e_{2d} = \eta_1 e_1 + e_2\,. \quad (22)$$

When z_2 converges to 0, considering (22), e_2 will converge to e_{2d}, which means that $(\dot{e}_1 + e_1) \to 0$ that is a desired behavior. Based on (22), we have:

$$e_2 = z_2 - \eta_1 z_1\,. \quad (23)$$

and the dynamic of z_2 is computable as:

$$\dot{z}_2 = -\eta_1^2 z_1 + \eta_1 z_2 + e_3\,. \quad (24)$$

However, the desired dynamic is $\dot{z}_2^{ref} = -\eta_2 z_2$. Therefore, a new desired value for e_3 can be obtained as $e_{3d} = -\eta_1\eta_2 e_1 - (\eta_1 + \eta_2)e_2$ based on (24) and $\dot{z}_2^{ref}$. The other conceptual error is defined as:

$$z_3 \triangleq e_3 - e_{3d} = \eta_1\eta_2 e_1 + (\eta_1 + \eta_2)e_2 + e_3\,. \quad (25)$$

To push z_3 to zero, its dynamic is computed:

$$\dot{z}_3 = \eta_1\eta_2 e_2 + (\eta_1 + \eta_2)e_3 + \beta_1 e_1 + \beta_2 e_2 + \beta_3 e_3 + \psi + u\,. \quad (26)$$

However, the desired dynamic is $\dot{z}_3^{ref} = -\eta_3 z_3$. Thus, by $\dot{z}_3 \to \dot{z}_3^{ref}$, we have:

$$\eta_3 z_3 + \eta_1\eta_2 e_2 + (\eta_1 + \eta_2)e_3 + \beta_1 e_1 + \beta_2 e_2 + \beta_3 e_3 + \psi + u = 0. \quad (27)$$

Now, we can propose the synchronization control law as:

$$\begin{aligned} u = &-\psi - (\eta_1\eta_2\eta_3 + \beta_1)e_1 \\ &-\left((\eta_1\eta_2 + \eta_1\eta_3 + \eta_2\eta_3) + \beta_2\right)e_2 \\ &-\left((\eta_1 + \eta_2 + \eta_3) + \beta_3\right)e_3\,. \end{aligned} \quad (28)$$

The block diagram of the proposed controller for the closed-loop synchronization system is depicted in Fig. 3.

This controller design procedure roots in the contraction theory and guarantees the stability of the closed-loop system. In this paper, we defined the state vector of the closed-loop system as $E = [e_1, e_2, e_3]^T$ and the generalized state vector as $Z = [z_1, z_2, z_3]^T$, therefore, the state generalization (coordination transition) is:

$$Z = \varphi E\,, \quad (29)$$

in which,

$$\varphi = \begin{bmatrix} 1 & 0 & 0 \\ \eta_1 & 1 & 0 \\ \eta_1\eta_2 & \eta_1 + \eta_2 & 1 \end{bmatrix}. \quad (30)$$

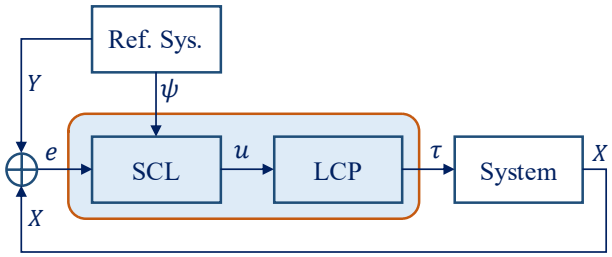

Fig. 3. Block diagram of the proposed controller for the closed-loop synchronization system

Considering (21) and (28), the closed-loop system can be rewritten as:

$$\dot{E} = \begin{bmatrix} 0 & 1 & 0 \\ 0 & 0 & 1 \\ -\zeta_1 & -\zeta_2 & -\zeta_3 \end{bmatrix} E \tag{31}$$

in which, $\zeta_1 = (\eta_1\eta_2\eta_3)$, $\zeta_2 = (\eta_1\eta_2 + \eta_1\eta_2 + \eta_1\eta_2)$, $\zeta_1 = (\eta_1 + \eta_2 + \eta_3)$. In addition, the generalized system is

$$\dot{Z} = \begin{bmatrix} \dot{z}_1 \\ \dot{z}_2 \\ \dot{z}_3 \end{bmatrix} = \begin{bmatrix} -\eta_1 & 1 & 0 \\ 0 & -\eta_2 & 1 \\ 0 & 0 & -\eta_3 \end{bmatrix} Z\,. \tag{32}$$

Therefore, Jacobian of the system is

$$J = \frac{\partial f(E)}{\partial E} = \begin{bmatrix} 0 & 1 & 0 \\ 0 & 0 & 1 \\ -\zeta_1 & -\zeta_2 & -\zeta_3 \end{bmatrix}. \tag{33}$$

The generalized Jacobian is

$$F = \left(\dot{\varphi} + \varphi \frac{\partial f(E)}{\partial E}\right)\varphi^{-1} = \begin{bmatrix} -\eta_1 & 1 & 0 \\ 0 & -\eta_2 & 1 \\ 0 & 0 & -\eta_3 \end{bmatrix}, \tag{34}$$

which is a uniformly negative definite matrix. Therefore, based on the contraction theory, applying the proposed controller, the generalized state (Z) exponentially converges to zero. In addition, since the largest eigenvalue of the symmetric part of the Jacobian matrix ($J = \partial f(E)/\partial E$) is not uniformly strictly negative, the synchronization error dynamics (E) is not exponentially convergent but it is asymptotically stable. Therefore, the synchronization error will converge to zero, despite the initial condition and the reference model. Fig. 4 shows the exponential stability of the generalized state, in which, 1000 runs of the generalized system's trajectory are drawn in gray lines in comparison to the exponential contraction (the largest eigenvalue of the symmetric part of the generalized Jacobian matrix, F).

V. Simulation

In this section, the proposed controller is applied to control the inverted pendulum that is described in section three. The initial conditions of the main system and the reference model are selected with normal random numbers in $[-1, +1]$. The reference model is the same as Eq. (20) with the following time-varying parameters:

$$\begin{cases} \gamma_1 = -1 - \big(2 - sin(5t)\big)e^{-\frac{1}{7}t}, \\ \gamma_2 = -3 - \big(2 - sin(3t)\big)e^{-\frac{1}{9}t}, \\ \gamma_3 = -3 - \big(2 - sin(2t)\big)e^{-\frac{1}{3}t}, \end{cases} \tag{35}$$

To evaluate the performance of the proposed control method, we provide several simulations and comparisons in Matlab/Simulink 2017a in Windows 10. The Simulink blocks are illustrated in Fig. 5.

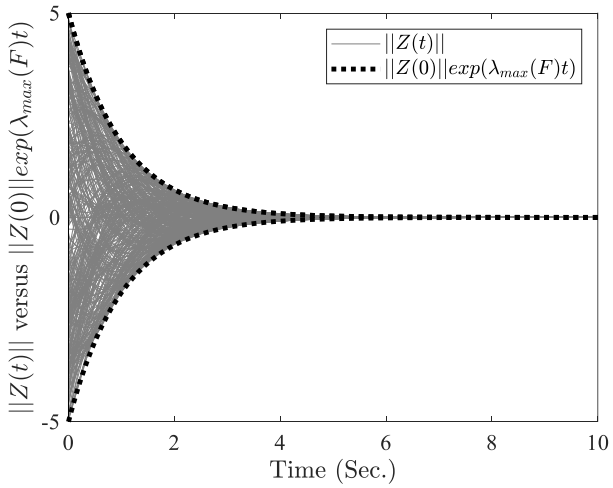

Fig. 4. Exponential convergence of the generalized state

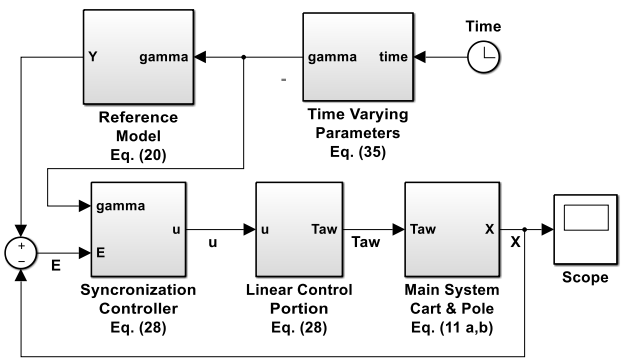

Fig. 5. Simulink blocks of the proposed control method

For a desired closed-loop system dynamics, we set the $\eta_1 = \eta_2 = \eta_3 = 3$. The tracking performance of the closed-loop control system is illustrated in Fig. 6, which shows that the system follows the reference model, which means that all three state variables track the corresponding state from the reference model. Note that there is only one control signal. As proposed in this paper, the controller is first partitioned into two portions, a state-space synchronization control law (SCL) and a linear control portion (LCP). The error is first handed into the SCL, where the signal u is produced, then the LCP converts u to τ as the actual control signal. These two signals are depicted in Fig. 7. The main features of the control signal are its boundedness and smoothness. The trajectory of the reference model and the actual system is drawn in Fig. 8. Since the steady-state response stays at the origin and the curve shows the states' movements, this trajectory illustrates the system's transient response. Since the system is a third-order dynamical system, its trajectory is also drawn in 3D space in Fig. 9 for better illustration. As seen in Fig. 8 and 9, although the initial condition of the two systems is completely random and different, the system follows the reference model. As a comparison study, the proposed method is compared with a recent similar method entitled "Nonlinear Model Predictive Controller Based on Particle Filter: Processor in the Loop Implementation" [32], which is based on particle filters containing normal random sequences of control signals. Weights are assigned to the particles based on their performance in predictive control.

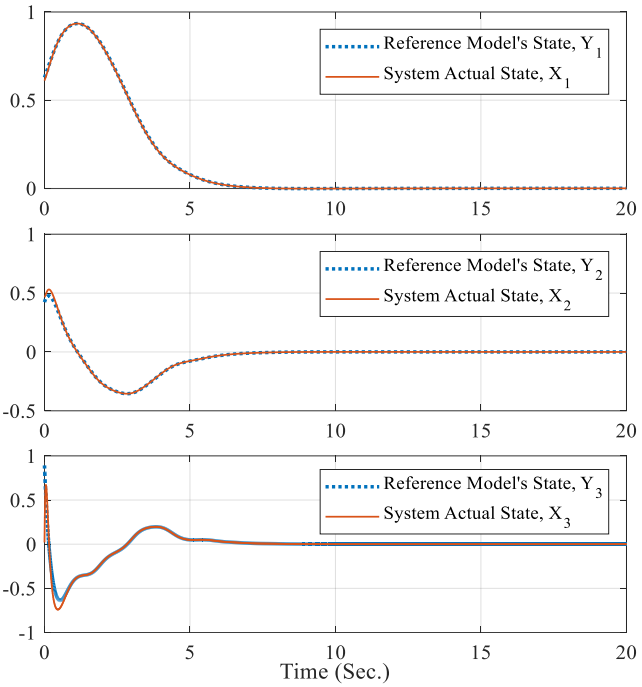

Fig. 6. Reference model synchronization control

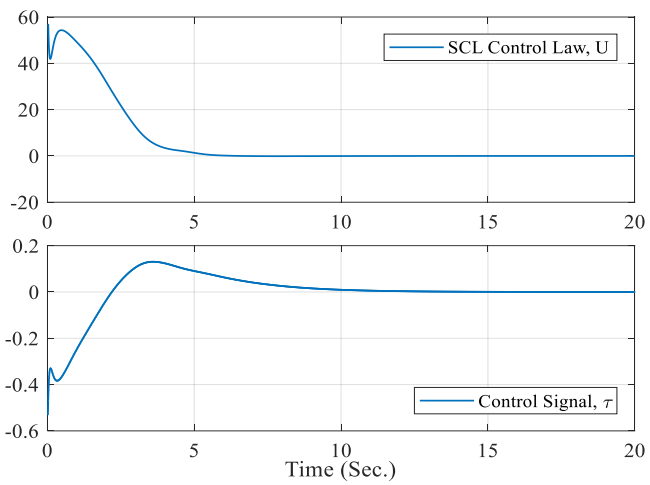

Fig. 7. Control Signals (u and τ)

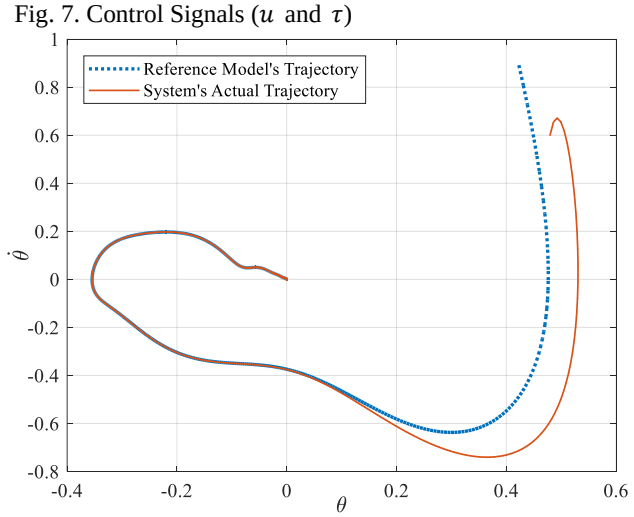

Fig. 8. Trajectory Tracking

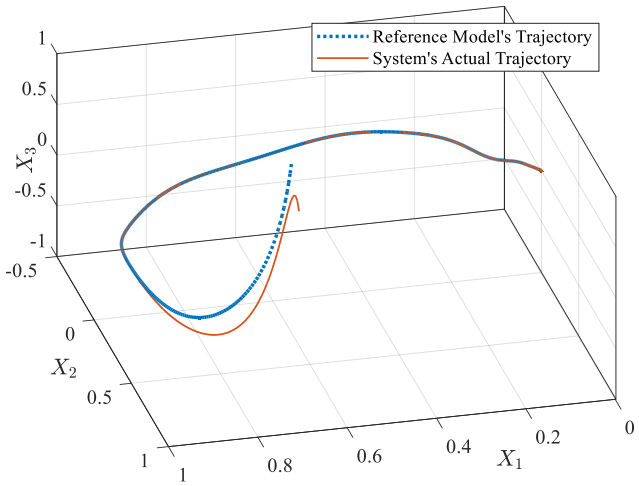

Fig. 9. 3D Trajectory Tracking

The resampling technique is utilized to provide the final control signal from the weighted particles. We simulated the method with 300 particles, a prediction horizon of 10 samples, and random initial weighting factors. The synchronization performances of the two methods are illustrated in Fig. 10, which shows that the proposed method has better performance rather than the compared method. Note that the runtime computational cost of our proposed method is far less than similar methods. The synchronization error is also drawn in Fig. 11, which shows the superiority of the proposed method. Moreover, the maximum value of the proposed control signal is 85.7951, while this value is 96.4092 for the comparative control signal. In general, the superiority of our proposed method can be observed in three perspectives, including (1) better synchronization performance and less error, (2) lower runtime computational cost, and (3) an easier design process.

VI. Conclusions

We proposed a synchronization controller based on contraction theory and control law partitioning for an underactuated two-wheeled self-balancing IP mobile robot. The proposed mechanism consists of a control law partitioning, which divides the control law into two parts, a linear transfer function and a synchronization control system designed based on contraction theory. The reference model is time-varying. The exponential convergence of the generalized state variables to zero and the asymptotic stability of the closed-loop synchronization system are proved. The main achievements of the proposed control method are ease of design, low runtime computational cost, guaranteed stability with exponential convergence, adjustable desired transient response, small synchronization error, and finally the ability of experimental implementation due to its simplicity. The proposed method is applicable for every dynamical system from chaotic to industrial robotics. The comparison study confirms the superiority of the method. In future studies, we will investigate the proposed mechanism for some chaotic mappings.

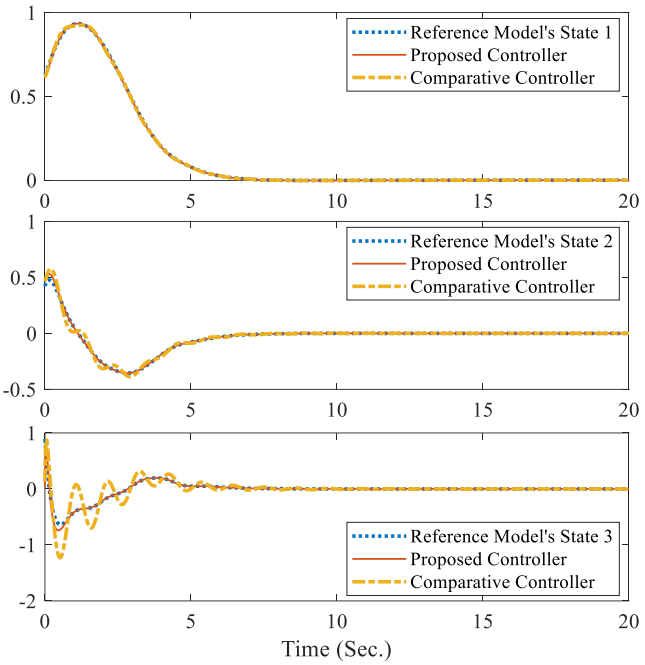

Fig. 10. Comparison study on synchronization performance

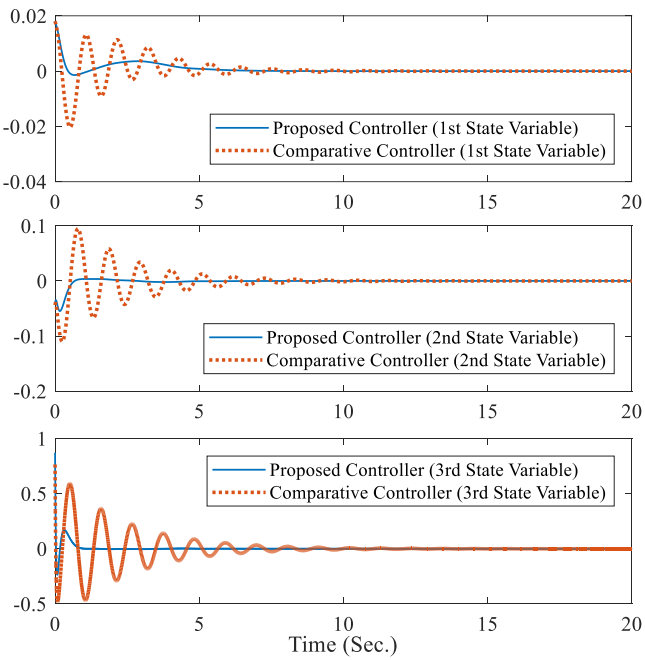

Fig. 11. Comparison study on synchronization error

REFERENCES

[1] M. F. Hamza, H. J. Yap, I. A. Choudhury, A. I. Isa, A. Y. Zimit, and T. Kumbasar, "Current development on using Rotary Inverted Pendulum as a benchmark for testing linear and nonlinear control algorithms," *Mech Syst Signal Process*, vol. 116, pp. 347–369, 2019, doi: https://doi.org/10.1016/j.ymssp.2018.06.054.

[2] S. Gora, S. S. Gupta, and A. Dutta, "Energy-Based Footstep Planning of Biped on Uneven Deformable Terrain Using Nonlinear Inverted Pendulum," J. Mech. Robot., vol. 15, no. 5, Nov. 2022.

[3] P. Frankovský, L. Dominik, A. Gmiterko, I. Virgala, P. Kurylo, and O. Perminova, "Modeling of Two-Wheeled Self-Balancing Robot Driven by DC Gearmotors," *International Journal of Applied Mechanics and Engineering*, vol. 22, no. 3, pp. 739–747, 2017, doi: doi:10.1515/ijame-2017-0046.

[4] M. van Mierlo, M. Vlutters, E. H. F. van Asseldonk, and H. van der Kooij, "Sagittal-plane balance perturbations during very slow walking: Strategies for recovering linear and angular momentum," J. Biomech., vol. 152, p. 111580, 2023.

[5] M. H. Jali, T. A. Izzuddin, R. Ghazali, C. C. Soon, and F. N. Zohedi, "Robust Controller Design with Particle Swarm Optimization for Nonlinear Prosthetic Hand System," *International Journal of Mechanical Engineering and Robotics Research*, vol. 6, no. 5, pp. 406–412, 2017, doi: https://doi.org/10.18178/ijmerr.6.5.406-412.

[6] M. Jalaeian-F., M. M. Fateh, and M. Rahimiyan, "Bi-Level Adaptive Computed-Current Impedance Controller for Electrically Driven Robots," *Robotica*, vol. 39, no. 2, pp. 200–216, May 2020, doi: 10.1017/S0263574720000314.

[7] S. Hanasaki, Y. Tazaki, H. Nagano, and Y. Yokokohji, "Running Trajectory Generation Including Gait Transition between Walking Based on the Time-Varying Linear Inverted Pendulum Mode," in *2022 IEEE-RAS 21st International Conference on Humanoid Robots (Humanoids)*, 2022, pp. 851–857. doi: 10.1109/Humanoids53995.2022.10000112.

[8] A. I. Tătaru and M. I. Baritz, "Development of biomechanical gait analysis based on inverted pendulum theory," *IOP Conf Ser Mater Sci Eng*, vol. 1256, no. 1, p. 12006, 2022, doi: 10.1088/1757-899X/1256/1/012006.

[9] J. Torres-Figueroa, E. A. Portilla-Flores, J. A. Vásquez-Santacruz, E. Vega-Alvarado, and L. F. Marín-Urías, "A Novel General Inverse Kinematics Optimization-Based Solution for Legged Robots in Dynamic Walking by a Heuristic Approach," *IEEE Access*, vol. 11, pp. 2886–2906, 2023, doi: 10.1109/ACCESS.2023.3234315.

[10] P. Narayanan, G.; Syed Ali, M.; Iqbal, Mohammed Mujtaba; Kumar, "Synchronization of fractional-order permanent magnet synchronous generator model based on terminal sliding mode control with switching surface," Math. Eng. Sci. Aerosp., vol. 12, no. 3, pp. 655–667, 2021.

[11] G. Narayanan, G. Muhiuddin, M. S. Ali, A. A. Z. Diab, J. F. Al-Amri, and H. I. Abdul-Ghaffar, "Impulsive Synchronization Control Mechanism for Fractional-Order Complex-Valued Reaction-Diffusion Systems With Sampled-Data Control: Its Application to Image Encryption," *IEEE Access*, vol. 10, pp. 83620–83635, 2022.

[12] F. Grasser, A. D'Arrigo, S. Colombi, and A. C. Rufer, "JOE: A mobile, inverted pendulum," *IEEE Transactions on Industrial Electronics*, vol. 49, no. 1, 2002, doi: 10.1109/41.982254.

[13] C. A. Ibañez, O. G. Frias, and M. S. Castañón, "Lyapunov-Based Controller for the Inverted Pendulum Cart System," *Nonlinear Dyn*, vol. 40, no. 4, pp. 367–374, 2005, doi: 10.1007/s11071-005-7290-y.

[14] N. Muskinja and B. Tovornik, "Swinging up and stabilization of a real inverted pendulum," *IEEE Transactions on Industrial Electronics*, vol. 53, no. 2, pp. 631–639, 2006, doi: 10.1109/TIE.2006.870667.

[15] L. B. Prasad, B. Tyagi, and H. O. Gupta, "Optimal control of nonlinear inverted pendulum dynamical system with disturbance input using PID controller & LQR," in *2011*

IEEE International Conference on Control System, Computing and Engineering, 2011, pp. 540–545. doi: 10.1109/ICCSCE.2011.6190585.
[16] M. Khoshroo, M. Eftekhari, and M. Eftekhari, "Reinforcement learning control of four degree of freedom inverted pendulum," *mdrsjrns*, vol. 18, no. 1, pp. 388–396, Mar. 2018.
[17] S. Irfan, A. Mehmood, M. T. Razzaq, and J. Iqbal, "Advanced sliding mode control techniques for Inverted Pendulum: Modelling and simulation," *Engineering Science and Technology, an International Journal*, vol. 21, no. 4, pp. 753–759, 2018, doi: https://doi.org/10.1016/j.jestch.2018.06.010.
[18] E. Franco, A. Astolfi, and F. Rodriguez y Baena, "Robust balancing control of flexible inverted-pendulum systems," *Mech Mach Theory*, vol. 130, pp. 539–551, 2018, doi: https://doi.org/10.1016/j.mechmachtheory.2018.09.001.
[19] T. Johnson, S. Zhou, W. Cheah, W. Mansell, R. Young, and S. Watson, "Implementation of a Perceptual Controller for an Inverted Pendulum Robot," *J Intell Robot Syst*, vol. 99, no. 3, pp. 683–692, 2020, doi: 10.1007/s10846-020-01158-4.
[20] B. Goswami and A. Chatterjee, "Balancing a Stick With Eyes Shut: Inverted Pendulum on a Cart Without Angle Measurement," J. Dyn. Syst. Meas. Control, vol. 145, no. 4, Feb. 2023.
[21] S. Israilov et al., "Reinforcement learning approach to control an inverted pendulum: A general framework for educational purposes," PLoS One, vol. 18, no. 2, p. e0280071, Feb. 2023.
[22] S. Zeghlache, M. Z. Ghellab, A. Djerioui, B. Bouderah, and M. F. Benkhoris, "Adaptive fuzzy fast terminal sliding mode control for inverted pendulum-cart system with actuator faults," Math. Comput. Simul., vol. 210, pp. 207–234, 2023.
[23] G. M. Moatimid, A. T. El-Sayed, and H. F. Salman, "Dynamical analysis of an inverted pendulum with positive position feedback controller approximate uniform solution," Sci. Rep., vol. 13, no. 1, p. 8849, 2023.
[24] J.-J. E. Lopez, Brett T. and Slotine, "Contraction Metrics in Adaptive Nonlinear Control," *ArXiv*, 2020, doi: https://doi.org/10.48550/arxiv.1912.13138.
[25] B. T. Lopez and J.-J. E. Slotine, "Adaptive Nonlinear Control With Contraction Metrics," *IEEE Control Syst Lett*, vol. 5, no. 1, pp. 205–210, 2021, doi: 10.1109/LCSYS.2020.3000190.
[26] B. B. Sharma and I. N. Kar, "Contraction theory based adaptive synchronization of chaotic systems," *Chaos Solitons Fractals*, vol. 41, no. 5, pp. 2437–2447, 2009, doi: DOI:101016/jchaos200809031.
[27] W. LOHMILLER and J.-J. E. SLOTINE, "On Contraction Analysis for Non-linear Systems," *Automatica*, vol. 34, no. 6, pp. 683–696, 1998, doi: https://doi.org/10.1016/S0005-1098(98)00019-3.
[28] W. Lohmiller and J.-J. E. Slotine, "Control system design for mechanical systems using contraction theory," *IEEE Trans Automat Contr*, vol. 45, no. 5, pp. 984–989, 2000, doi: 10.1109/9.855568.
[29] I. R. Manchester and J.-J. E. Slotine, "Control Contraction Metrics: Convex and Intrinsic Criteria for Nonlinear Feedback Design," *IEEE Trans Automat Contr*, vol. 62, no. 6, pp. 3046–3053, 2017, doi: 10.1109/TAC.2017.2668380.
[30] X. Zhang and B. Cui, "Synchronization of Lurie system based on contraction analysis," *Appl Math Comput*, vol. 223, pp. 180–190, 2013, doi: https://doi.org/10.1016/j.amc.2013.07.080.
[31] A. Ouannas, I.M. Batiha, S. Bekiros, J. Liu, H. Jahanshahi, A.A. Aly, A.H. Alghtani, "Synchronization of the Glycolysis Reaction-Diffusion Model via Linear Control Law," Entropy, vol. 23, no. 11, p. 1516, Nov. 2021, doi: 10.3390/e23111516.
[32] A. Khooshehmehri, S. Nasrollahi, and M. Aliyari, "Chaos Synchronization in Josephson Junction Using a Nonlinear Model Predictive Controller Based on Particle Filter: Processor in the Loop Implementation," Int. J. Ind. Electron. Control Optim., vol. 4, no. 3, pp. 355–366, 2021.
[33] J. Y. Lau, W. Liang, and K. K. Tan, "Enhanced robust impedance control of a constrained piezoelectric actuator-based surgical device," Sensors Actuators A Phys., vol. 290, pp. 97–106, 2019.
[34] J. Y. Lau, W. Liang, and K. K. Tan, "Adaptive sliding mode enhanced disturbance observer-based control of surgical device," ISA Trans., vol. 90, pp. 178–188, 2019.
[35] M. Jalaeian-F, M. M. Fateh, M. Rahimiyan, M. Jalaeian-F., M. M. Fateh, and M. Rahimiyan, "Optimal Predictive Impedance Control in the Presence of Uncertainty for a Lower Limb Rehabilitation Robot," J. Syst. Sci. Complex., vol. 33, no. 3, pp. 1310–1329, May 2020.

Rogayeh Soltani is a Ph.D. candidate in Applied Mathematics at Payame Noor University (PNU). She is also with the Farhangian University of Tabriz as an instructor, since 2001. Her research interests include control, optimization, contraction theory, and control of chaotic systems.

Bashir Naderi received his Ph.D. in Applied Mathematics from Payame Noor University (PNU), Iran, in 2016. Now, he is an Assistant Professor of Mathematics at Payame Noor University (PNU), Iran. His main research interests include Dynamical systems, Optimal control, Chaotic systems, and Secure communications.

Saeed Nezhadhosein received his Ph.D. in Applied Mathematics from Pyame Noor University (PNU), Iran, in 2015. Now he is an Assistant Professor of Mathematics at Payame Noor University (PNU), Iran. His main research interests include Dynamical systems, Optimal control, and Nonlinear optimization.

Aghileh Heydari was born in 1972. She received her B.S. degree in Applied Mathematics in 1994 from Sharif University, Tehran, Iran, and her M.S. degree in Applied Mathematics (Optimal Control) in 1997 from Ferdowsi University of Mashhad (FUM), Iran. She wrote her dissertation under the supervision of Prof. Ali Vahidian Kamyad. She received her Ph.D. degree under the supervision of Prof. Ali Vahidian Kamyad at FUM in March 2002. She is currently a professor of Mathematics at Payame Noor University (PNU), Iran. PNU has numerous branches throughout Iran. Her research interests include Optimization, Optimal Control, Fuzzy Optimal Control Problems, Biomathematics, Modelling & Optimal Control of infectious diseases.

IECO

This page intentionally left blank.

International Journal Of
Industrial Electronics Control and Optimization
Print ISSN: 3517-2645
Online ISSN: 3568-2645
Homepage: https://ieco.usb.ac.ir/

A Cascaded Multilevel Inverter Based on a New Basic Unit

Roya Naderi[1], and Ebrahim Babaei[2]

[1]Department of Electrical Engineering, Heris Branch, Islamic Azad University, Heris, Iran
[2]Faculty of Electrical and Computer Engineering, University of Tabriz, Tabriz, Iran
Corresponding author's e-mail: ro.naderi@iau.ac.ir

Article Info

Article type:
Research Article

Article history:
Received: 2022-November-3
Received in revised form: 2023-May 9
Accepted: 2023- June-14
Published online: 2023-July-1

Keywords:
Cascaded Multilevel Inverter,
Symmetric Cascaded Multilevel Inverter,
Asymmetric Cascaded Multilevel Inverter.

ABSTRACT

In this paper, a new basic unit is proposed for multilevel inverters. Then, a series connection of the proposed basic unit is used to recommend a new topology for multilevel inverters. To determine the magnitude of dc voltage sources, a new algorithm is presented. For the proposed algorithm, different performance parameters such as total voltage rating of switches (TVRS), number of gate drivers, and number of required sources are calculated as a function of the number of output voltage levels and are compared with other topologies. The comparison proves that the proposed cascaded topology requires fewer components and gate driver circuits than most of the other conventional topologies. Moreover, the voltage rating of switches is less than the other topologies which result lower cost and control complexity. Finally, the correctness of the theoretical analysis and the performance of the proposed inverter are verified using the laboratory and simulation results under different scenarios.

I. Introduction

Among conventional inverters, multilevel inverters have been used for many applications and are one of the most popular solutions in medium and high-power applications [1, 2]. Due to the applicability of multilevel inverters in high-voltage direct current (HVDC), hybrid electrical vehicles (HEV), machine drives, and FACTS devices [3-6], researchers have always suggested ways to optimize their topologies by reducing components, gate driver circuits, and rating of switches [7]. These inverters can produce staircase voltage waveforms with high-quality outputs. The desired output voltage is produced by appropriate switching of several dc voltage sources, which leads to lower rating voltage for switches, less total harmonic distortion (THD), and electromagnetic interference (EMI) [8, 9]. In general, the multilevel inverters are divided into three categories: neutral-point-clamped (NPC) [10], flying capacitor (FC) [11], and cascaded H-bridge (CHB) inverters [12]. The CHB inverters, which are formed by the series connection of basic units, consist of various arrays of power electronic switches and dc voltage sources and are divided into symmetric and asymmetric topologies with equal and non-equal magnitudes of dc voltage sources, respectively. It is important to mention that using non-equal magnitudes reduces the number of required components.

The presented topology in [13] uses non-isolated dc voltage sources with equal amplitudes, and this causes to produce a lower number of voltage levels at the output. Also, the presented structure in [14] needs to a transformer and an H-bridge on the primary side. So, it suffers from high voltage rates on the switches. The presented topologies in [15, 16] utilize a high number of IGBTs and gate driver circuits, and the values of rating voltage on switches are much higher. As a result, the cost and volume of the inverter will be high. The presented topology in [17] can operate in both symmetric and asymmetric conditions. Although, this topology can generate

negative and positive levels at the output and also can reduce the number of switches, but it needs a high number of independent dc voltages sources. To solve this problem, the presented algorithm in [18] can be used. In the presented topologies in [13, 17, 19, 20], the H-bridge is used to generate negative output levels. In [21], two topologies based on developed H-bridge (consists of six switches) are presented. The total standing voltage for these topologies is very high. Although the presented topology in [22] can produce even and odd levels at the output without using H-bridge, but it uses a large number of power electronic elements. The presented structures in [23-28] need to less number of voltage sources, but balancing the voltages across capacitors is the main drawback for these topologies. The presented topologies in [29, 30] need to switches with low voltage rating. So, these topologies are suitable for high-voltage applications, but need to high number of IGBTs and gate driver circuits. The presented topologies in [17, 31] need to bidirectional switches which increase the total cost of inverter.

This paper presents a new topology for multilevel inverters in which the number of power electronic components and rating voltage across the switches are lower. The cascaded multilevel inverter structure is presented in Section 2. Then, a new algorithm to determine the magnitude of the dc voltage sources structure is proposed in Section 3. Section 4 compares the proposed topology with other topologies in terms of the number of IGBTs, rating voltages of switches, and the number of gate drivers. Finally, the laboratory results are presented for the production of a 15-level inverter to prove the feasibility of the proposed topology.

II. Proposed Cascaded Multilevel Inverter

Fig. 1 shows the topology of the basic unit for the multilevel inverter. This topology consists of eight unidirectional switches, two bidirectional switches with the common-emitter configuration, and three dc voltage sources (V_1, V_2, and V_3). Clearly, the switches (S_1, S_2), (S_3, S_4), (S_5, S_6), (S_7, S_8), and (S_A, S_B) are fully complementary to have a safe performance and cannot be turned on simultaneously. The switching states of the proposed basic unit to produce different voltage levels are provided in Table 1. In this table, 1 and 0 indicate the on and off states of the switches, respectively. To increase the number of output voltage levels, *n* basic units can be cascaded to form the proposed cascaded multilevel inverter shown in Fig. 2. In this topology, both positive and negative levels at the output are generated. The number of dc voltage sources (N_{source}), the number of IGBTs (N_{IGBT}) used, and the number of gate drivers (N_{driver}) in the proposed cascaded topology can be calculated by the following equations:

$$N_{source} = 3n \quad (1)$$

$$N_{IGBT} = 12n \quad (2)$$

$$N_{driver} = 10n \quad (3)$$

Another important parameter in the cost of inverters is the number of variety voltage sources ($N_{variety}$), which is determined by the variety of the magnitudes of voltage sources. This factor for the topology is calculated by the following equation:

$$N_{variety} = 3n \quad (4)$$

The output voltage of the proposed topology is equal to the sum of the output voltage of all basic topologies. In other words:

$$v_{out} = v_{o,1} + v_{o,2} + v_{o,3} + \cdots + v_{o,n} \quad (5)$$

According to Table 1 and its development for n cascaded units, the maximum output voltage ($v_{o\max,total}$) is obtained as follows:

$$v_{o,total,\max} = \sum_{k=1}^{n}(v_{o,k,\max}) = \sum_{k=1}^{n}(V_{k,1} + V_{k,2} + V_{k,3});\ k = 1,2,3,\ldots,n \quad (6)$$

TVRS is another important parameter in multilevel inverters, which directly affects the price of the inverter. The total rating voltage on the switches of the proposed inverter is as follows:

$$TVRS = TVRS_{us} + TVRS_{bs} \quad (7)$$

where $TVRS_{bs}$ and $TVRS_{us}$ are rating voltage of bidirectional and unidirectional switches, respectively, so that

$$TVRS_{us} = \sum_{k=1}^{n}\sum_{j=1}^{8} V_{S,k,j} \quad (8)$$

where $V_{S,k,j}$ is the value of the rating voltage of the switches $S_{k,1}, S_{k,2}, S_{k,3}, \cdots, S_{k,8}$ of unidirectional switches in the *k*th unit. The rating voltage of unidirectional switches is as follows:

$$V_{S,k,1} = V_{S,k,2} = V_{k,1} \quad (9)$$

$$V_{S,k,3} = V_{S,k,4} = V_{k,1} + V_{k,2} \quad (10)$$

$$V_{S,k,5} = V_{S,k,6} = V_{k,2} + V_{k,3} \quad (11)$$

$$V_{S,k,7} = V_{S,k,8} = V_{k,3} \quad (12)$$

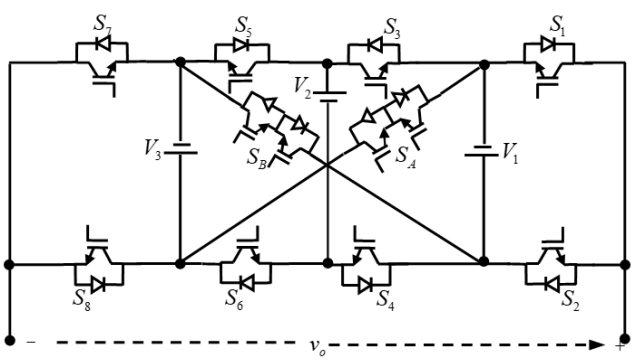

Fig. 1. The structure of the proposed basic unit.

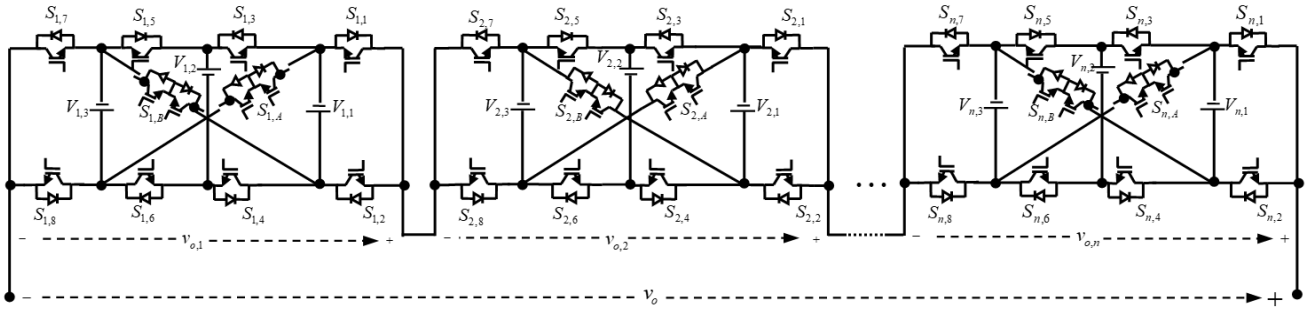

Fig. 2. The proposed cascaded multilevel inverter.

TABLE 1
SWITCHING STATES OF THE PROPOSED BASIC UNIT

S_1	S_2	S_3	S_4	S_5	S_6	S_7		S_8	S_A	S_B	v_o
1	0	1	0	1	0	1		0	0	0	0
0	1	1	0	1	0	1		0	0	0	V_1
1	0	1	0	0	1	0		1	0	0	V_2
0	1	1	0	0	1	0		1	0	0	V_1+V_2
0	1	0	1	0	1	1		0	0	0	V_3
0	1	0	0	0	0	1		0	1	0	V_1+V_3
1	0	1	0	0	1	1		0	0	0	V_2+V_3
0	1	1	0	0	1	1		0	0	0	$V_1+V_2+V_3$
1	0	0	1	0	1	0		1	0	0	$-V_1$
0	1	0	1	1	0	1		0	0	0	$-V_2$
1	0	0	1	1	0	1		0	0	0	$-(V_1+V_2)$
1	0	1	0	1	0	0		1	0	0	$-V_3$
1	0	0	0	0	0	0		1	0	1	$-(V_1+V_3)$
0	1	0	1	1	0	0		1	0	0	$-(V_2+V_3)$
1	0	0	1	1	0	0		1	0	0	$-(V_1+V_2+V_3)$

Now, we can calculate $TVRS_{us}$ as follows:

$$TVRS_{us}=4\sum_{k=1}^{n}(V_{k,1}+V_{k,2}+V_{k,3}) \quad \textbf{(13)}$$

The relation of $TVRS_{bs}$ is given by

$$TVRS_{bs}=(V_{S,k,A}+V_{S,k,B}) \quad \textbf{(14)}$$

Considering the following equation:

$$V_{S,k,A}=V_{S,k,B}=V_{k,1}+V_{k,2}+V_{k,3} \quad \textbf{(15)}$$

Eq. (14) can be simplified as follows:

$$TVRS_{bs}=2\sum_{k=1}^{n}(V_{k,1}+V_{k,2}+V_{k,3}) \quad \textbf{(16)}$$

Using (6), (13), and (16), the relation of TVRS is obtained as follows:

$$TVRS=6\sum_{k=1}^{n}(V_{k,1}+V_{k,2}+V_{k,3})=6v_{o,toal,\max} \quad \textbf{(17)}$$

Determining the magnitudes of dc voltage sources is important to calculate (6) and (17). Therefore, it is necessary to determine the magnitudes of input dc voltage sources for calculating the output voltage and rating voltage on the switches.

III. Determination of the Magnitude of DC Voltage Sources

Estimating the dc voltage source values is very important for determining the number of output voltage levels. For the proposed topology, it is possible to present different algorithms for determining the magnitude of dc voltage sources. Here, one of them is presented.

In the proposed algorithm, to generate high voltage levels, the following method is proposed to determine the magnitude of dc voltage sources.

First unit:

$$V_{1,1}=V_{dc} \quad \textbf{(18)}$$

$$V_{1,2}=2V_{dc} \quad (19)$$

$$V_{1,3}=4V_{dc} \quad (20)$$

Second unit:

$$V_{2,1}=2V_{o\max,1}+V_{dc}=14V_{dc}+V_{dc}=15V_{dc} \quad \textbf{(21)}$$

$$V_{2,2}=2V_{2,1}=30V_{dc} \quad (22)$$

$$V_{3,2}=4V_{2,1}=60V_{dc} \quad (23)$$

***n*th unit:**

$$V_{n,1}=2\sum_{k=1}^{n-1}(V_{o\max,k})+V_{dc}=15^nV_{dc} \quad \textbf{(24)}$$

$$V_{n,2}=2V_{n,1} \quad (25)$$

$$V_{n,3}=4V_{n,1} \quad (26)$$

In this algorithm, the number of output voltage levels, the maximum output voltage ($N_{step,3}$), and the total value of the rating voltage of the switches ($TVRS_3$) are obtained by the following equations:

$$N_{step,3}=15^n \quad \textbf{(27)}$$

$$V_{out,3,\max}=\frac{(15^n-1)}{2}V_{dc}=\frac{(N_{step,3}-1)}{2}V_{dc} \quad (28)$$

$$TVRS_3 = 3(N_{step,3} - 1)V_{dc} \quad (29)$$

IV. Comparison of Results

This section compares the advantages and disadvantages of the proposed topology with other structures. Fig. 3(a) shows the number of IGBTs against the number of output voltage levels. This comparison confirms the advantage of the proposed multi-level inverter based on the third algorithm due to the use of the least number of IGBTs compared to other topologies. The number of gate drivers against levels in different structures is shown in Fig. 3(b), which indicates that the number of drivers in the recommended structure based on the third algorithm is the same as the topology presented in [16] and it requires a minimum number of drivers compared to other structures. Fig. 3(c) depicts the number of dc voltage sources against the number of output voltage levels. This figure proves that based on the proposed algorithm, the proposed multilevel inverter requires the least number of these sources as compared with the topologies presented in [23, 25, 26, 28], but the topologies presented in [22-25, 28] use capacitors. Considering the importance of rating voltage on the switches, which is one of the most important parameters in determining the cost of multilevel inverters, this parameter is also discussed and compared. Rating voltage of the switches against the number of levels for all three algorithms of the proposed topology has the same relation and does not depend on the magnitude of dc voltage sources.

Fig. 3(d) compares the rating voltage of the switches against the number of levels for the topologies proposed in other references. This comparison indicates that the rating voltage of the switches in the proposed topology is lower than that in the other topologies. Table 2 compares the number of IGBTs, drivers, dc voltage sources, capacitors, diodes, and rating voltage for the switches of different topologies with 69 levels in output voltage and verifies the advantage of the proposed topology. It is worth noting that according to Fig. 1 and Table 1, to generate the output voltage levels, three transistors and one diode or four transistors are instantaneously in the current path. Therefore, the maximum number of components in the current path in the proposed multilevel inverter, is four.

To compare the efficiency of different topologies, it is assumed that all topologies generate 69 levels with the same load and same maximum output voltage. Also, it is assumed that the same switches are used. Under these conditions, based on simulation results, the efficiency of all compared topologies are calculated and summarized in Table 3. According to this table, the efficiency of the proposed topology is better than in comparison to most of the already presented topologies.

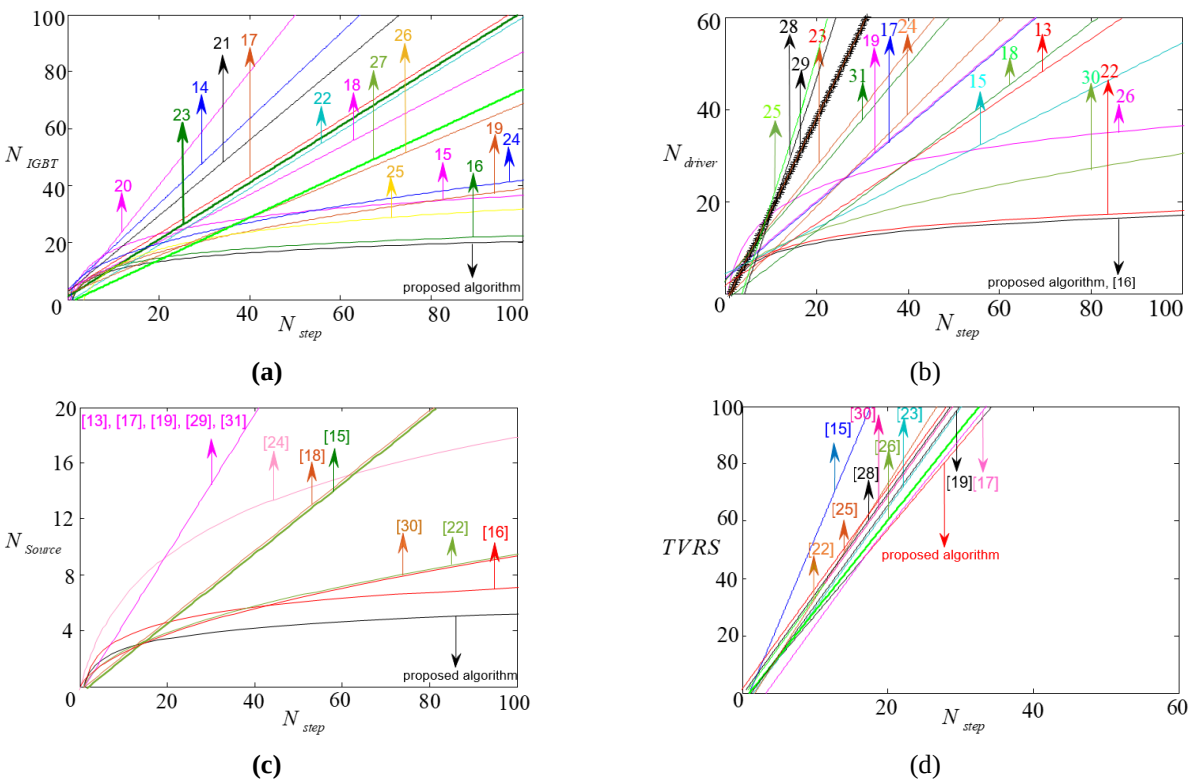

Fig. 3. The results of the comparison: (a) N_{IGBT}, (b) N_{driver}, (c) N_{source}, (d) $TVRS$ versus N_{step}.

TABLE 2
THE COMPARISON RESULTS WITH OTHER STRUCTURES FOR PRODUCING 69-LEVEL

Parameters	N_{step}	N_{IGBT}	N_{driver}	N_{source}	Capacitors	Diodes	*TVRS*
[13]	69	61	35	30	-	-	-
[15]	69	32	32	11	-	-	$354V_{dc}$
[16]	69	20	15	6	-	-	-
[17]	69	63	53	30	-	-	$187V_{dc}$
[18]	69	42	42	11	-	-	-
[19]	69	54	54	30	-	-	$206V_{dc}$
[22]	69	22	16	8	-	-	$289V_{dc}$
[23]	69	93	78	1	30	-	$205V_{dc}$
[24]	69	59	59	15	30	103	-
[25]	69	170	170	1	34	-	$236V_{dc}$
[26]	69	27	27	2	4	8	$199V_{dc}$
[28]	69	169	169	1	33	-	$235V_{dc}$
[29]	69	120	118	30	-	-	-
[30]	69	30	24	7	-	-	$233V_{dc}$
[31]	69	83	73	30	-	-	-
Proposed Topology	69	18	15	5	-	-	$177V_{dc}$

TABLE 3
EFFICIENCY COMPARISON

Parameters	Efficiency [%]
[13]	93.2
[15]	95.7
[16]	96.1
[17]	92.9
[18]	94.4
[19]	91.3
[22]	95.1
[23]	87.4
[24]	93.1
[25]	85.2
[26]	95.9
[28]	85.1
[29]	89.7
[30]	94.9
[31]	90.7
Proposed Topology	94.1

V. Experimental and Simulation Results

In this section, according to Fig. 1, a 15-level inverter with a maximum output voltage of 400V is designed and analyzed. For the simulation and experimental tests, an R–L load with the values of R=280.39Ω and L=373.1mH is used. The switching frequency is 5kHz, and the minimum error method is used to control the proposed structure. The values of dc voltage sources V_1, V_2 and V_3 are 57, 114, 228V, respectively. Figs. 4 and 5 illustrate the built prototype and experimental results of the output voltage and current waveforms, respectively. Also, the processor AVR ATMEGA 32 was used in the construction of this circuit. Fig. 6 represents the rating voltage on $S_1, S_2, \cdots, S_8, S_A, S_B$ switches with the maximum rating voltage on the switches as 57, 57, 171, 171, 343, 343, 229, 229, 400, and 400V, respectively. The total value of the rating voltage on the switches for the 15-level inverter (the sum of the rating voltage on the switches) is 2400V, which corresponds to Eq. 17. Positive or zero voltages in Fig. 6(a) indicates that the switch S_1 is unidirectional and positive, and negative voltages in Fig. 6(i) Fig. 6 shows that the switch S_A is bidirectional.

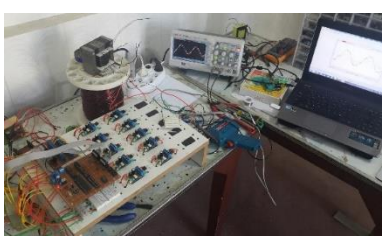

Fig. 4. Laboratory prototype.

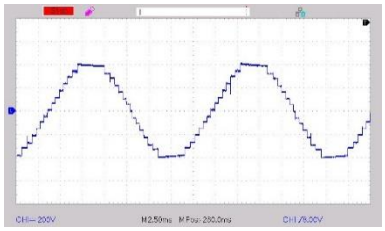

(a)

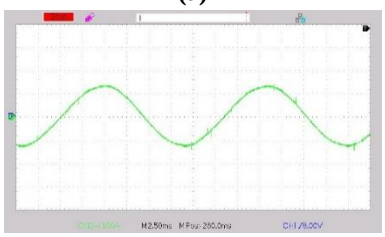

(b)

Fig. 5. Experimental results: (a) output 15-level voltage (200 V/div), (b) output 15-level current (1 A/div).

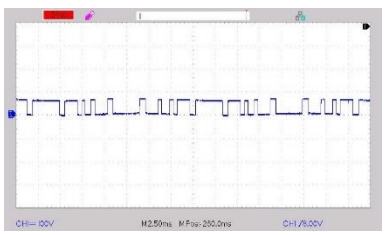

(a)

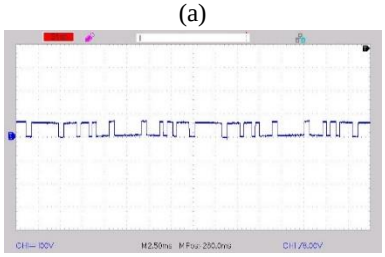

(b)

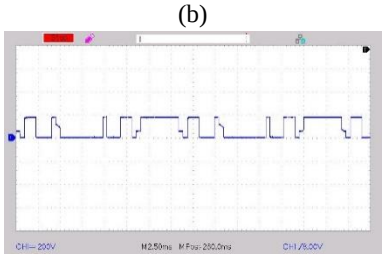

(c)

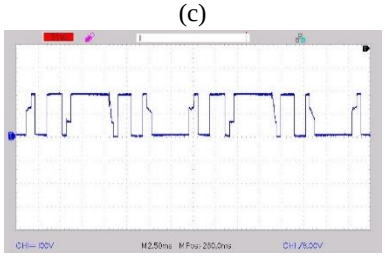

(d)

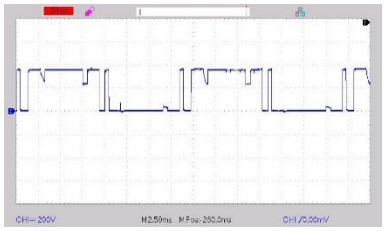

(e)

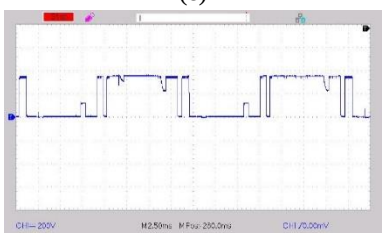

(f)

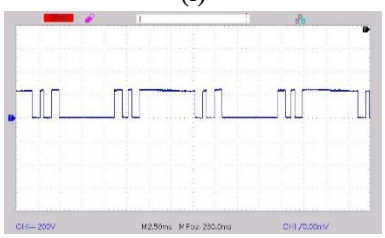

(g)

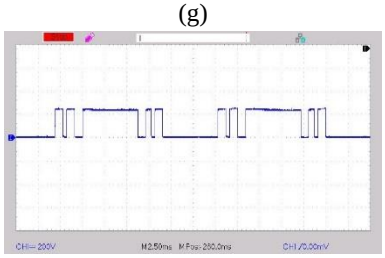

(h)

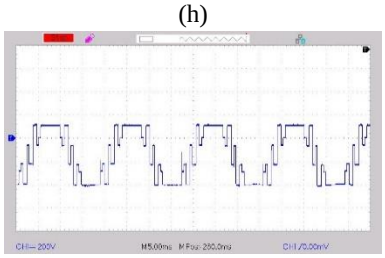

(i)

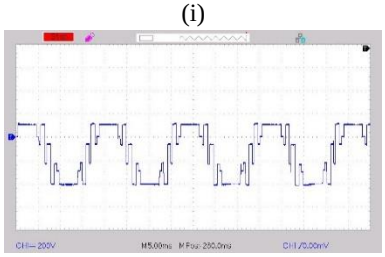

(j)

Fig. 6. Voltage of switches: (a) S1 (100 V/div), (b) S2 (100 V/div), (c) S3 (200 V/div), (d) S4 (100 V/div), (e) S5 (200 V/div), (f) S6 (200 V/div), (g) S7 (200 V/div), (h) S8 (200 V/div), (i) SA (200 V/div), (j) SB (200 V/div).

To reconfirm the given theories, the simulation results in PSCAD software are given. Fig. 7 shows the simulation results for output voltage and current. Comparing these waveforms with experimental results, shows that there is a good agreement between the simulation and experimental results. Fig. 8 shows the simulation results for switches' current. The maximum value of these waveforms shows the current rating of the switches. It is clear that the current rating of switches depends on the load. By changing the load, these values are changed. Fig. 9 shows the power delivered by each source. To show the correct operation of the proposed topology in different power factors, more simulation results are shown in Fig. 10.

As mentioned before, by series connection of the proposed basic unit, it is possible to generate more levels at the output. For example, by using series connection of two units with the values of dc voltage sources V1, V2, and V3 are 3V, 6V, and 12V, respectively, 225 levels with a maximum output voltage equal to 336V is obtained. The simulation result in PSCAD software for this inverter is shown in Fig. 11.

VI. Conclusion

This paper presented a new topology for a cascaded multilevel inverter which comprises a cascaded connection of basic units. The proposed topology was analyzed in symmetric and asymmetric modes of operation with the ffundamental frequency switching control method. To highlight the advantages of the proposed topology to the previous topologies, it was compared with a number of other topologies. Based on the results of the comparison, it is found that the proposed cascaded topology has the minimum number of power components, gate driver circuits, and rating voltage on the switches as compared to most of other conventional topologies, resulting in lower cost, volume, and complexity of the control circuits. A 60-level inverter based on the third algorithm proposed technology requires 18 IGBTs and 15 driver circuits and its total rating voltage on the switches is 177V. While to generate the same number of output voltage levels, structures in [23, 17] require 93 and 63 IGBTs and 78 and 53 gate driver circuits, and the total rating voltage on the switches is 205V and 354V respectively. To study the feasibility of the operation of the 15-level inverter based on the third algorithm, experimental results are provided.

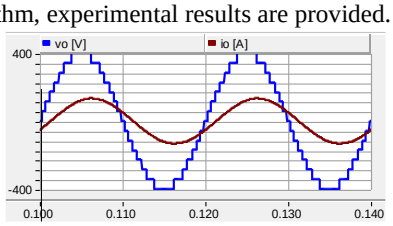

Fig. 7. Simulation results: output voltage and current.

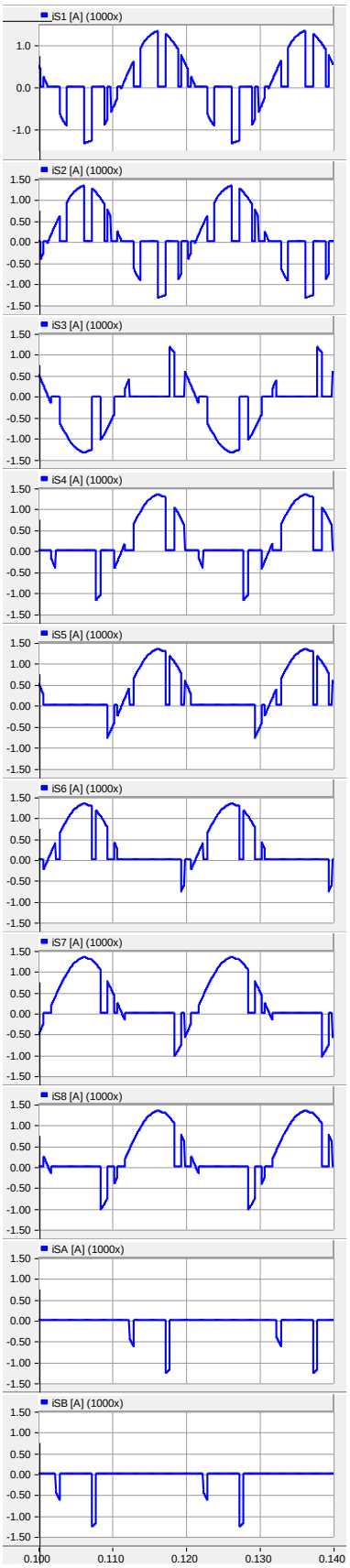

Fig. 8. Simulation results: switches' currents.

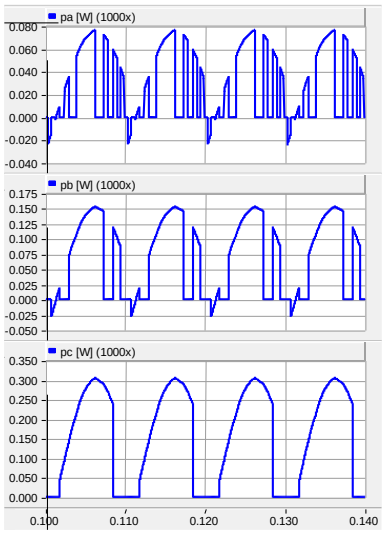

Fig. 9. Power delivered by sources.

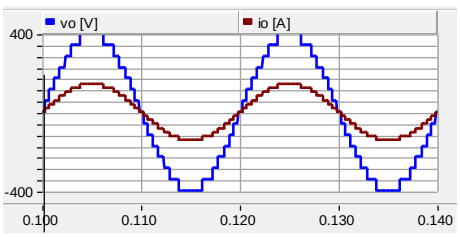

R = 280.39Ω

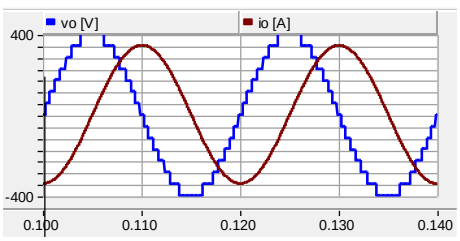

L=373.1mH

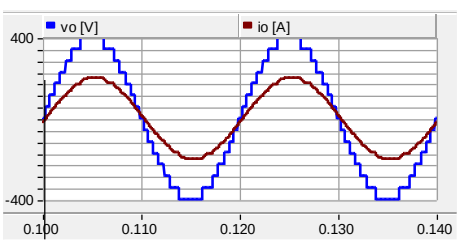

R = 200Ω, L=55mH

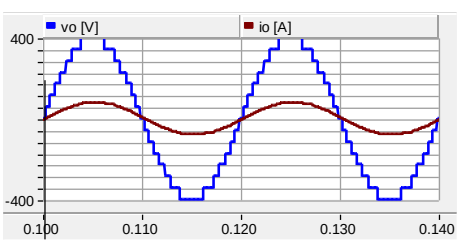

R = 50Ω, L=120mH

Fig. 10. Simulation results for different power factors.

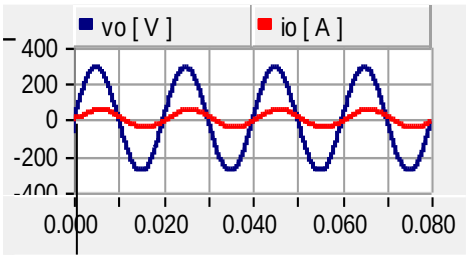

Fig. 11. The output voltage and current waveforms for 225-level cascaded inverter.

REFERENCES

[1] I. Saady, M. Karim, B. Bossoufi, N. El Ouanjli, S. Motahhir, and B. Majout, "Optimization and control of photovoltaic water pumping system using kalman filter based MPPT and multilevel inverter fed DTC-IM," Results in Engineering, 17, pp.100829, 2023.

[2] M.B. Sambhani, and N. BL, "A new generalized symmetrical/asymmetrical boost integrated multilevel inverter with reduced components for PV/UPS applications," International Journal of Electronics, in press, 2023, DOI:10.1080/00207217.2022.2164075.

[3] G.P. Adam, I.A. Abdelsalam, K.H Ahmed, and B.W. Williams, "Hybrid multilevel converter with cascaded H-bridge cells for HVDC applications: operating principle and scalability," IEEE Transactions on Power Electronics, vol. 30, no. 1, pp. 65-77, Jan. 2015.

[4] S. Debnath, J. Qin, B. Bahrani, M. Saeedifard, and P. Barbosa, "Operation, control, and applications of the modular multilevel converter: a review," IEEE Transactions on Power Electronics, vol. 30, no. 1, pp. 37-53, Jan. 2015.

[5] X. Zeng, D. Gong, M. Wei, and J. Xie, "Research on novel hybrid multilevel inverter with cascaded H-bridges at alternating current side for high-voltage direct current transmission," IET Power Electronic, vol. 11, no. 12, pp. 1914-1925, Oct. 2018.

[6] R. Picas, J. Zaragoza, G. Konstantinou, and G.J. Capella, "Study and comparison of discontinuous Modulation for modular multilevel converters in motor drive applications," IEEE Transactions on Industrial Electronics, vol. 66, no. 3, pp. 2376-2386, March 2019.

[7] M.R.J. Oskuee, M. Karimi, Y. Naderi, S.N. Ravadanegh, and S.H. Hosseini, "A new multilevel voltage source inverter configuration with minimum number of circuit elements," Journal of Central South University, vol. 24, no. 4. pp. 912-920, 2017.

[8] S.K. Maddugari, V.B. Borghate, and S. Sabyasachi, "A reliable and efficient single-phase modular multilevel inverter topology," International Journal of Circuit Theory and Applications, vol. 47, no. 5, pp. 718-737, 2019.

[9] M. Sarebanzadeh, M.A. Hosseinzadeh, C. Garcia, E. Babaei, M. Hosseinpour, A. Seifi, and J. Rodriguez, "A 15-level switched-capacitor multilevel inverter structure with self-balancing capacitor," IEEE Transactions on Circuits and Systems II: Express Briefs, vol. 69, no. 3, pp. 1477-1481, March 2022.

[10] X. Yuan and I. Barbi, "Fundamentals of a new diode clamping multilevel inverter," IEEE Transactions on Power Electronics, vol. 15, no. 4, pp. 711-718, Jan. 2000.

[11] Y. Ye, G. Zhang, X. Wang, Y. Yi, and K. W. E. Cheng, "Selfbalanced switched-capacitor thirteen-level inverters with reduced capacitors count," IEEE Transactions on

Industrial Electronics, vol. 69, no. 1, pp. 1070-1076, Jan. 2022.

[12] B. Sharma, R. Dahiya, and J. Nakka, "Capacitor voltage balancing in cascaded H-bridge multilevel inverter and its modelling analysis for grid integrated wind energy conversion system application," International Journal of Circuit Theory and Applications, vol. 47, no. 8, pp. 1323-1339, Aug. 2019.

[13] M. Farhadi. Kangarlu, E. Babaei, and S. Laali, "Symmetric multilevel inverter with reduced components based on non-insulated dc voltage sources," IET Power Electronics, vol. 5, no. 5, pp. 571-581, 2012.

[14] A.J.P. Nascimento, B.F. de Menezes, S.J. de Mesquita, K.R. Costa, F.L. Tofoli, S. Daher, and F.L.M. Antunes, "Bidirectional isolated aAsymmetrical multilevel inverter," IEEE Transactions on Circuits and Systems II: Express Briefs, vol. 70, no. 1, pp. 151-155, Sep. 2022.

[15] S. Saeidabadi, A. Ashraf. Gandomi, S.H. Hosseini, M. Sabahi, and Y. Ashraf. Gandomi, "New improved three-phase hybrid multilevel inverter with reduced number of components", IET Power Electronics, vol. 10, no. 12, pp. 1403-1412, 2017.

[16] F. Masoudinia, E. Babaei, M. Sabahi, and H. Alipour, "New basic unit and cascaded multilevel inverters with reduced power electronic devices," International Journal of Electronics, vol. 107, no. 7, pp. 1177-1194, Feb. 2020.

[17] M.F. Kangarlu and E. Babaei, "A generalized cascaded multilevel inverter using series connection of submultilevel inverters," IEEE Transactions on Power. Electronics, vol. 28, no. 2, Jun. 2012.

[18] S. Laali, K. Abbaszades, and H. Lesani, "A new algorithm to determine the magnitudes of dc voltage sources in asymmetrical cascaded multilevel converters capable of using charge balance control methods," in Proc. Int. Conf. Elect. Mach. Syst, 2010, Incheon, South Korea, pp. 56-61.

[19] E. Babaei, S. Laali, and Z. Bayat, "A single-phase cascaded multilevel inverter based on a new basic unit with reduced number of power switches," IEEE Transactions on Industrial Electronics, vol. 62, no. 2, Jul. 2014.

[20] A. Taheri and A. Rasulkhani, "A new multilevel inverter topology with component count reduction," International Journal of Industrial Electronics Control and Optimization., vol. 2, no. 4, 2019.

[21] M. Ghodsi, and S.M. Barakati, "New generalized topologies of asymmetric modular multilevel inverter based on six-switch H-bridge," International Journal of Circuit Theory and Applications, vol. 48, no. 5, pp. 789-808, 2020.

[22] R. Naderi, E. Babaei, M. Sabahi. and A. Daghigh, "Optimization of a new extended cascaded multilevel inverter topology to reduce DC voltage sources and power electronic components," International Journal of Industrial Electronics Control and Optimization, vol. 4, no. 4, pp.465-474. 2021.

[23] M. Khenar, A. Taghvaie, J. Adabi, and M. Rezanejad, "Multi-level inverter with combined T-type and cross-connected modules," IET Power Electronics, vol. 11, no. 8, pp. 1407- 1415, 2018.

[24] S. P. Gautam, L. K. Sahu, and S. Gupta, "Reduction in number of devices for symmetrical and asymmetrical multilevel inverters," IET Power Electronics, vol. 9, no. 4, pp. 698-709, Mar. 2016.

[25] Y. Wang, J. Ye, R. Ku, Y. Wang and J Liang, "Novel extensible multilevel inverter based on switched-capacitor structure," Journal of Power Electronics, vol. 22, no. 9, pp.1448-1460, 2022.

[26] E. Zamiry, N. Vosoughi, S. Hossein. Hosseini, R. Barzegarkhoo and M. Sabahi, "A new cascaded switched-capacitor multilevel inverter based on improved series–parallel conversion with less number of components," IEEE Transactions on Industrial Electronics, vol. 63, no. 6, Jun. 2016.

[27] M. Ghodsi, and S. M. Barakati, "A Generalized cascade switched-capacitor multilevel converter structure and its optimization analysis," IEEE Journal of Emerging and Selected Topics in Power Electronics, vol. 8, no. 4, pp. 4306-4317, 2019.

[28] Y. Wang, J. Ye, R. Ku, Y. Shen, G. Li, and J. Liang, "A modular switched-capacitor multilevel inverter featuring voltage gain ability," Journal of Power Electronics, vol. 23, no. 1, pp. 11-22. 2023.

[29] K.K. Gupta and Sh. Jain, "A multilevel voltage source inverter (VSI) to maximize the number of levels in output waveform," Electric Power Energy, vol. 44, no. 1, pp. 25–36, Jan. 2013.

[30] N. Prabaharan, Z. Salam,C. Cecati, and K. Palanisamy, "Design and implementation of new multilevel inverter topology for trinary sequence using unipolar pulsewidth modulation," IEEE Transactions on Industrial Electronics, vol. 67, no. 5, pp. 3573-3582, May. 2019.

[31] M. Patra, M. Ghosh. Majumder, B. Das, A. Chakraborty, and P. Ranjan. Kasari, "A new modular multilevel converter topology with reduced number of power electronic components," in Proc. ICIIECS, 2017, Coimbatore, India.

Roya Naderi was born in Tabriz, Iran in 1980. received her B.Sc. and M.Sc. degrees in Electronics Engineering both from Islamic Azad University of Tabriz in 2003 and 2009, respectively and her Ph.D. degree in Electrical Engineering (power electronics) from Islamic Azad University of Shabestar in 2020. She joined Islamic Azad University of Heris in 2012. She is the author of two books and 10 journal and conference papers. Her current research interests include the analysis and control of power electronic inverters and multilevel inverters.

Ebrahim Babaei received the Ph.D. degree in Electrical Engineering from the University of Tabriz, in 2007. He is the author and co-author of one book and more than 660 journal and conference papers. He also holds 26 patents in the area of power electronics. His current research interests include the analysis, modelling, design, and control of Power Electronics Converters and their applications, Renewable Energy Sources, and FACTS Devices. Prof. Babaei has been the Editor-in-Chief of the Journal of Electrical Engineering of the University of Tabriz, since 2013. He is also currently an Associate Editor of the IEEE Transactions on Industrial Electronics, IEEE Transactions on Power Electronics, IEEE Open Journal of the Industrial Electronics Society, Iranian Journal of Science and Technology, Transactions of Electrical Engineering, and International Journal of Circuit Theory and Applications.

IECO

This page intentionally left blank.

International Journal Of
Industrial Electronics Control and Optimization
Print ISSN: 3517-2645
Online ISSN: 3568-2645
Homepage: https://ieco.usb.ac.ir/

Four-Switch Inverter-Based Hybrid Power Filter Optimized By Meta-Heuristic Algorithm of SPEA-II

P. Rahmati-kahkha [1] | A. Hosseinpour [1] | A. Khajeh [2]

Department of Electrical Engineering, University of Zabol, Zabol, Iran.[1]
Department of Electrical Engineering, University of Sistan and Baluchestan, Zahedan, Iran.[2]
Corresponding author's email: a.hoseinpour@uoz.ac.ir

Article Info

Article type:
Research Article

Article history:
Received: 2023- April-21
Received in revised form: 2023- June 24
Accepted: 2023-July-1
Published online: 2023-July-1

Keywords:
Hybrid power filter,
four-switch inverter,
SPEA-II

ABSTRACT

Power electronics converters application has increased in modern distribution systems due to their advantages to control and process the power flow. Unfortunately, these converters generate harmful harmonics and inject them into the grid. The modern standards of the systems accept that the grid includes harmonics but they have to be less than the specified value. To satisfy standards, power filters must be added to nonlinear loads. This paper proposes a new hybrid power filter to achieve them. Furthermore, the conventional six-switch inverter of active power filters is substituted to decrease the overall cost and complexity of the system. To design the parameters of the passive part of the filter, the SPEA-II meta-heuristic optimization algorithm is used which minimized the overall cost as well as harmonics suppression. Consequently, the four-switch inverter along with the optimized design of the passive part makes the proposed hybrid active filter attractive for practical applications. The THD of the injected current to the grid as a critical index in different nonlinear and dynamic loads is less than 2%. Simulation results in different scenarios show the effectiveness of the proposed hybrid filter.

NOMENCLATURE

V_a	Source Voltage Phase a	P	Active Power
V_b	Source Voltage Phase b	q	Reactive Power
V_c	Source Voltage Phase c	$\bar{P}$	Average Active Power
I_a	Source current Phase a	$\tilde{P}$	Oscillating Active Power
I_b	Source current Phase b	$\bar{q}$	Average Reactive Power
I_c	Source current Phase c	$\tilde{q}$	Oscillating Reactive Power
V_α	instantaneous voltages in the α axis	I_{sn}	Source current in the n-th harmonic
V_β	instantaneous voltages in the β axis	I_1	Main current component
I_α	instantaneous Line Current in the α axis		
I_β	instantaneous Line Current in the β axis		

I. Introduction

Due to the destructive effects of harmonics in the power systems, it is necessary to decrease their amplitudes. Power electronics converters are used in modern power systems diversely which caused the loads to behave nonlinear [1]. These nonlinear loads could inject harmonics into the grid and deteriorate the power quality. To reject tripled harmonics, a common solution is using the delta winding of transformers. To decrease more harmonics power filters must be added.

Three types of filters are proposed in power systems: Passive power filter (PPF), Active power filter (APF), and Hybrid power filter (HPF) [2-4]. The design of APFs and HPFs is a complex nonlinear optimization problem. PPFs consist of RLC circuits and are tuned to reject a special frequency. Variations of system impedance, during faults, and so on, could decrease the performance of these filters. Therefore, APFs are proposed to overcome the drawbacks of PPFs. The APFs require high-power inverters to handle harmonics and reactive power. It is proposed to utilize HPFs to decrease the overall cost of the system [5-7].

A hybrid passive filter consisting of two passive filters, a series filter and another parallel filter based on TCR, is proposed in [8,9] to suppress the harmonics and compensate for reactive power. The proposed filter has a fast dynamic response and is non-sensitive to source impedance variation, but the series part of the system that the full load current must be handled is the main drawback of this structure. In [10], a new modulation scheme, named variable modulation index, is applied to a parallel active filter to reduce current harmonics in a wind turbine system based on PMSG and a rectifier.

A four-leg eight-switch voltage source inverter is utilized in [11] to reduce the harmonics of the current and unbalanced single-phase nonlinear current. The model predictive control scheme is implemented on the eight-switch inverter in this structure. An APF with Transformer multilevel inverter in a three-phase three-wire system is used in [12] that brings dc-link voltage regulation in addition to current harmonics compensation. In [13], a Transformer HPF based on a two-leg six-switch inverter is proposed to accomplish the injected harmonics standard of IEEE-59.

Due to the nonlinearity nature of designing parameters of the filters, some authors are proposed to use meta-heuristic algorithms to solve the optimization problem. PSO algorithm is used in [14] to optimize the filter parameters to minimize the harmonics content and the cost of the filter. The authors of [15] have proposed to utilize ant colony optimization to optimally design the parameters of a single-tuned filter operating in a non-sinusoidal power system. The objective functions in this study are maximization of efficiency and power factor in addition to harmonics reduction.

The main goal of the authors in [16] is to minimize the overall cost of the filter, including initial cost and maintenance costs. To achieve this goal, the crow search algorithm is used. Genetic algorithm and Monte Carlo simulation are proposed in [17] to optimize the passive filter parameters in a single-tuned filter installed on a distribution system with photovoltaic generation.

H-infinity optimal control design is used in [18] to find the optimal controller parameters of the hybrid active filter via a convex optimization algorithm. An Adaptive Sine-Cosine Moth-Flame Optimization Algorithm for Parameter Identification of Hybrid Active Power Filters is proposed in [19]. The authors claimed a new population-based algorithm named ASC-MFO to optimally design the parameters of the hybrid active power filter. In [20] a hybrid shunt active power filter is optimized by hybrid Particle Swarm Optimization-Grey Wolf Optimization (PSO-GWO) and fractional order proportional-integral-derivative controller. Utilizing space vector modulation instead of sinusoidal pulse width modulation is investigated in [21]. The grasshopper optimization algorithm for optimizing hybrid active power filters' parameters is proposed in [22]. The authors in [23] proposed finite-set model predictive control for a hybrid active power filter. Moreover, a hybrid filter that is equipped with a three-level converter reduces current THD to 3.11 % [24]. In addition, a parallel hybrid filter decreases both current and voltage THD to 16.49% and 5.3%, respectively [25].

It is clear from investigating the previously published works on this topic that the active filters are very effective in case of harmonics cancelation in some steps [26] and complicated methods [27] but the cost of the filter would be high if we just utilize the active filter. Therefore, hybrid power filters could be used in high-power applications to bring the benefits of both active and passive filters. Designing the inductive and capacitive elements of the passive part of a hybrid power filter is a challenging issue that researchers work on the better methods.

Therefore, in this paper, the conventional six-switch inverter is replaced with a four-switch inverter to reduce the cost of HPF [28]. Consequently, the number of switches and drivers in this structure is lessened which could increase the overall reliability of the system. To design the THD and overall cost of the HPF, in this paper, the parameters of the HPF are optimized based on a meta-heuristic algorithm of Strengthen Pareto Evolutionary Algorithm-II (SPEA-II).

This paper is organized as follows. In section II, the structure of the proposed hybrid power filter is discussed. Optimization of the parameters of the passive filter based on the SPEA-II method is presented in section III. In section tor to investigate the performance of the proposed HPF, in nonlinear case study system is presented. The simulation results in different scenarios are discussed in this section. Finally, section 5 concludes the paper.

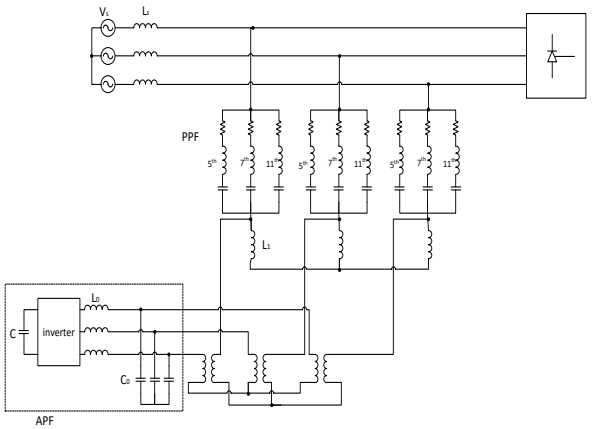

Fig. 1. The structure of the proposed HPF.

II. Methodology

A. THE STRUCTURE OF THE PROPOSED HPF

To reduce the harmonics content and overall cost of the filter, in this paper it is proposed to utilize a HPF. The passive filter of the proposed structure is selected to remove the harmonics orders of fifth, seventh, and eleventh. Furthermore, the parameters of the passive part of the filter are optimized based on the two-objective SPEA-II algorithm. The structure of the proposed HPF is depicted in Figure 1.

B. Reference current generation

Methods of reference current production could be classified into two categories time-based and frequency based. Time-based methods, such as instantaneous active-reactive power theory, relied on measurements and three-phase transformation. FFT is utilized for frequency-based methods such as bandstop filters. In this paper, the instantaneous active-reactive power theory is utilized. Three-phase voltages and currents measured in abc-frame are transformed to αβ-frame as follows:

$$\begin{bmatrix} V_\alpha \\ V_\beta \end{bmatrix} = \sqrt{\frac{2}{3}} \begin{bmatrix} 1 & -\frac{1}{2} & -\frac{1}{2} \\ 0 & \frac{\sqrt{3}}{2} & -\frac{\sqrt{3}}{2} \end{bmatrix} \begin{bmatrix} V_a \\ V_b \\ V_c \end{bmatrix} \quad (1)$$

$$\begin{bmatrix} I_\alpha \\ I_\beta \end{bmatrix} = \sqrt{\frac{2}{3}} \begin{bmatrix} 1 & -\frac{1}{2} & -\frac{1}{2} \\ 0 & \frac{\sqrt{3}}{2} & -\frac{\sqrt{3}}{2} \end{bmatrix} \begin{bmatrix} I_a \\ I_b \\ I_c \end{bmatrix} \quad (2)$$

Therefore, the powers are calculated as:

$$\begin{bmatrix} p \\ q \end{bmatrix} = \begin{bmatrix} V_\alpha & V_\beta \\ -V_\beta & V_\alpha \end{bmatrix} \begin{bmatrix} I_\alpha \\ I_\beta \end{bmatrix} \quad (3)$$

In the presence of harmonics, an oscillatory term is added to the average power that could be formulated as:

In the presence of harmonics, an oscillatory term is added to the average power that could be formulated as:

$$p = \bar{p} + \tilde{p} \quad (4)$$

$$q = \bar{q} + \tilde{q} \quad (5)$$

Where the average terms are denoted with the bar and oscillatory terms with tilde signs. To suppress harmonics components of line currents, the oscillatory terms of powers must be compensated by HPF. Hence, the reference currents of HPF could be derived as:

$$\begin{bmatrix} I_{c\alpha} \\ I_{c\beta} \end{bmatrix} = \frac{1}{V_\alpha{}^2 + V_\beta{}^2} \begin{bmatrix} V_\alpha & -V_\beta \\ V_\beta & V_\alpha \end{bmatrix} \begin{bmatrix} -\tilde{p} \\ -\tilde{q} \end{bmatrix} \quad (6)$$

$$\begin{bmatrix} I_{ca} \\ I_{cb} \\ I_{cc} \end{bmatrix} = \sqrt{\frac{2}{3}} \begin{bmatrix} 1 & 0 \\ -\frac{1}{2} & \frac{\sqrt{3}}{2} \\ -\frac{1}{2} & -\frac{\sqrt{3}}{2} \end{bmatrix} \begin{bmatrix} I_{c\alpha} \\ I_{c\beta} \end{bmatrix} \quad (7)$$

C. Four-switch inverter

It is beneficial to decrease the cost of inverters in active filters. Therefore, the four-switch structure is proposed in this paper to substitute the conventional six-switch structure. Consequently, the number of active power switches and required drivers was reduced to four instead of six which is attractive in HPFs due to cost reduction and improved reliability of the system.

III. OPTIMIZATION OF PASSIVE FILTER

The parameters of the passive filter are optimized based on meta-heuristic algorithms in this paper. The optimization process is briefly discussed as follows. The main factor to assess the performance of a filter is harmonics reduction. Hence, the first objective is considered as:

$$f_1: \min \left\{ \sqrt{\sum_{n=3,5,7,\ldots} \left(\frac{I_{sn}}{I_1}\right)^2} \right\} \quad (8)$$

Where I_{sn} is the source current in the nth harmonic and I_1 is the main current component. The second objective is the overall cost of the filter which is formulated as:

$$f_2: \min\{\text{Cost}(R.L.C) = K_R R_n + K_L L_n + K_C C_n\} \quad (9)$$

Where the cost coefficients of the filter are given by, K_R=100($/KW), K_L=250($/Kvar), and K_C=0.05($/Kvar).

A. SPEA-II ALGORITHM

In this study, SPEA-II is selected as the optimizing algorithm to solve the multi-objective problem of designing the passive filter. SPEA-II is a multi-objective optimization method that the evolution of the population carried on a probabilistic method. In contrast to the other evolutionary algorithms, in SPEA-II the direction and the distance of the current population from other members of the population are selected to teach the search process to a desirable direction. Therefore, the high quality of the produced responses is guaranteed in this method.

For the i^{th} member, a strength value S(i) is assigned, which expresses the number of solutions which it defeats. They are calculated by equation (10).

$$S(i) = |\{j | j \in P_t + \bar{P}_t \cap i \succ j\}| \quad (10)$$

Where, $P_t \; and \; \bar{P}_t$ are populations and archives, respectively. The initial fitness is calculated based on (11), which is computed for all members of the population and archive.

$$R(i) = \sum_{j \in P_t + \bar{P}_t, i \succ j} S(j) \quad (11)$$

When all its members are non-dominant, to compare two Pareto fronts, the Pareto fronts which has the same variety of answers and can spread the answers with more variety in the space of objectives is preferred. For this reason, only using the raw fitness function is not enough, and a secondary criterion is needed to be able to provide the answers in the space of the objective functions, with a suitable variety. Zeitler et al. [15] used the density estimation technique in SPEA-II, which uses the concept of the k^{th} nearest neighbor, where the density at each point is up to the k^{th} nearest neighbor. It is according to relation (12)

$$D(i) = \frac{1}{\sigma_i^k + 2} \quad (12)$$

where σ_i^k is the distance of the i^{th} member from its k^{th} nearest neighbor. k is equal to the square root of the sample size [15] as a result we will estimate the density of responses:

$$k = \sqrt{N + \bar{N}} \quad (13)$$

Finally, the final fitness value is calculated as the sum of the raw fitness and compression as equation (13).

$$F(i) = R(i) + D(i) \quad (14)$$

The lower F(i) is more popular.

In the following, the process of this algorithm is briefly discussed [29]:

Step 1: Create an initial population P_0 and a null external file $(\bar{P}_0 = \emptyset)$, determine generation size as N and generation count as t=0.

Step 2: Calculate the fitness of the population in each of P_t and $\bar{P}_t$ members.

Step 3: Move non-dominated solutions of P_t and $\bar{P}_t$ to. If the archived Pareto solutions size of $\bar{P}_{t+1}$ is greater than the maximum limit cut the size to $\bar{N}$, but if the size of $\bar{P}_{t+1}$ is less than $\bar{N}$, the dominated solutions in the end to the $\bar{P}_{t+1}$ until the size of $\bar{P}_{t+1}$ is equal to $\bar{N}$.

Step 4: If the stop condition is reached, select the non-dominated solutions as the final solution.

Step 5: select parents from $\bar{P}_{t+1}$ based on the championship rule.

Step 6: Implement crossover and mutation operators on parents on $\bar{P}_{t+1}$. Set t=t+1 and go to step 2.

IV. SIMULATION RESULTS

At first, the system under study, schematic in Figure 2, is simulated without any compensation method. The currents injected into the grid are depicted in Figure 3. a. Also, the harmonics content of the current is shown in Figure 3. b. To generate the current's harmonics, in this paper, a nonlinear load with a three-phase diode bridge is used. The parameters of the studied system are presented in Table 1. In the following, the performance of the system is studied in different scenarios. As it is shown in Figure 3. b, the harmonics content of the injected current is very high and it is necessary to compensate these harmonics to comply with the required standards such as IEEE-519.

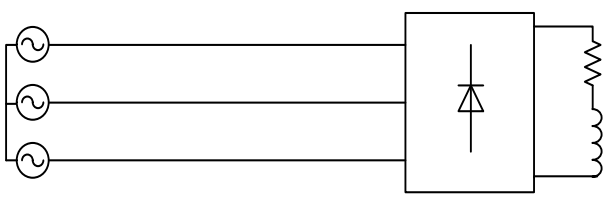

Fig. 2. Schematic of the studied system.

TABLE 1
PARAMETERS OF THE STUDIED SYSTEM

Item	Parameter	Value
1	Source Voltage	380 V
2	Frequency	60 Hz
3	Active power of the load	50 KW
4	Reactive power of the load	62.5 Kvar
5	Line resistance	0.0989 Ω
6	Line inductance	1.58mH

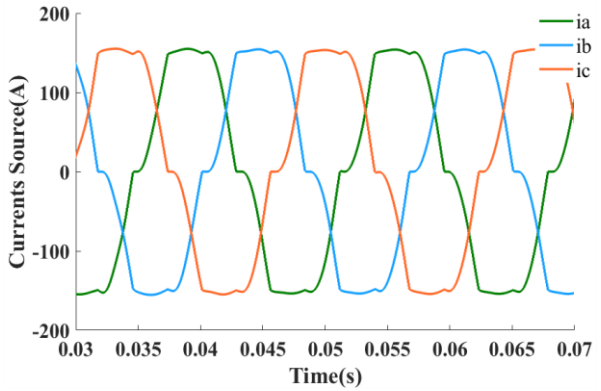

(a)

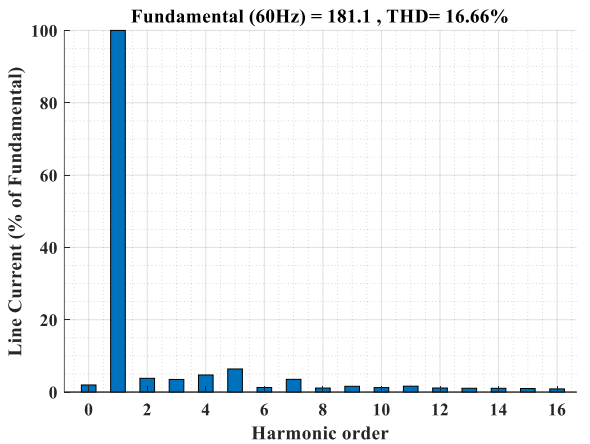

(b)

Fig. 3. The injected currents in the case of the active filter: a) real-time b) harmonics content.

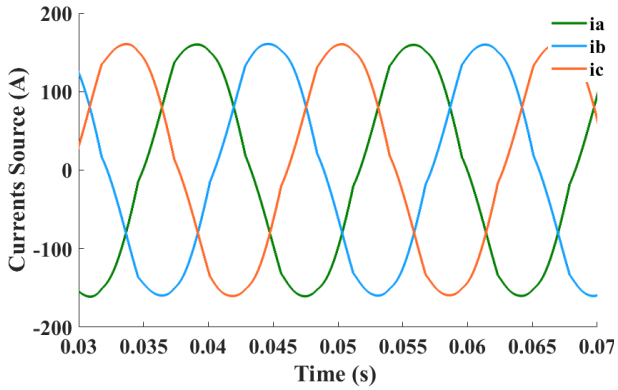

(a)

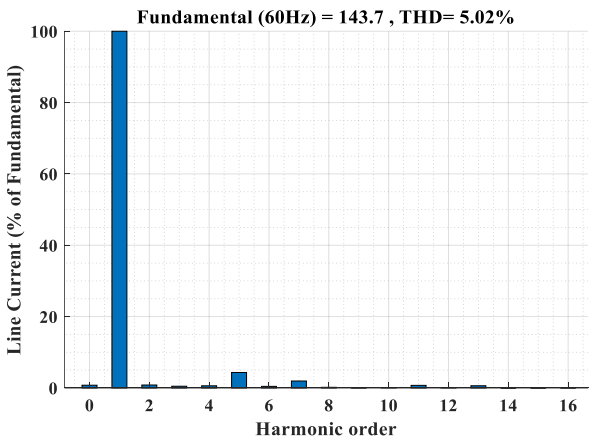

(b)

Fig. 4. The injected currents in the case of the active filter: a) real-time b) harmonics content.

A. Active Filter

If the active filter is utilized to compress the harmonics, the currents injected to the grid are depictedreal-timetime and frequency domain in Figures 4. a and b respectively. In the case of active filter compensation, the harmonics content is reduced but still more than the required standard of IEEE-519. Moreover, the required inverter in this scheme is high power which could limit the selection of this type of compensation in point of the overall system cost.

B. Passive Filter

The conventional method is to use passive filters for harmonics reduction. Even triple harmonics amplitude is very low. Therefore, the passive filter is designed to compress the 5th, 7th, and 11th harmonics. According to eq.15, the values of resistors, inductors, s, and capacitors are effective on the overall cost of the filter and must be designed to minimize the cost in addition to harmonics reduction. Hence, the problem is a two-objective optimization given by:

$$\begin{aligned} &\min F(x) = [f_1(x), f_2(x)] \\ &subject\ to \quad C_i^l \le C_i \le C_i^u \ , \ i = 5,7,11 \\ &\qquad\qquad L_i^l \le L_i \le L_i^u \ , \ i = 5,7,11 \\ &\qquad\qquad R_i^l \le R_i \le R_i^u \ , \ i = 5,7,11 \end{aligned} \tag{15}$$

To solve the above multi-objective problem, the meta-heuristic algorithm of SPEA-II is utilized. The obtained Pareto front is presented in Figure 5 for this problem (one point from it is selected based on the fuzzy min. max method). The designed parameters in this study are presented in Table.2. The compensated system based on the passive filter designed as described above is simulated. The real-time currents and harmonics content of the injected currents to the grid are depicted in Figures 6. a and b, respectively. As it is clear from Figure 6. b, the total harmonics distortion of the system is decreased to 4.96% which is less than the required standard, but the passive filter could not adapt to the changes of the grid and load. Therefore, it is proposed to use the hybrid filter in this paper.

A. The Proposed Hybrid Filter

It is proposed to use the hybrid filter to overcome the deficiencies of the active and passive filters. The power of the inverter of the hybrid filter is less than the active filter resulting in a cost reduction compared with the active filter. Also, including an active filter in the structure of the hybrid filter adds to the system adaptation due to changes in load and the grid.

TABLE 2
OPTIMIZED PARAMETERS OF THE PASSIVE FILTER

Item	Parameter	Value
1	C5	26.5807 μF
2	C7	33.248 μF
3	C11	24.725 μF
4	L5	10.6 mH
5	L7	4.3 mH
6	L11	2.4 mH
7	R5	0.33 Ω
8	R7	0.189 Ω
9	R11	0.166 Ω

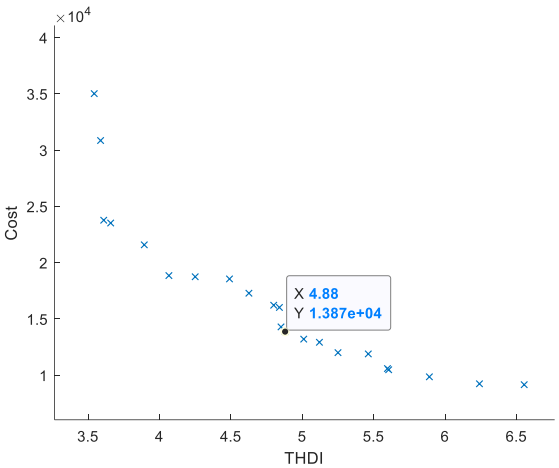

Fig. 5. Pareto front to optimize the passive filter.

TABLE 3
OPTIMIZED PARAMETERS OF THE PASSIVE FILTER

Item	Parameter	Value
1	C5	25.0496μF
2	C7	20.3711μF
3	C11	17.6754μF
4	L5	11.2mH
5	L7	7mH
6	L11	3.3mH
7	R5	0.35Ω
8	R7	0.31 Ω
9	R11	0.23 Ω

Moreover, two-stage filtering brings more effectiveness to the overall quality of the system.

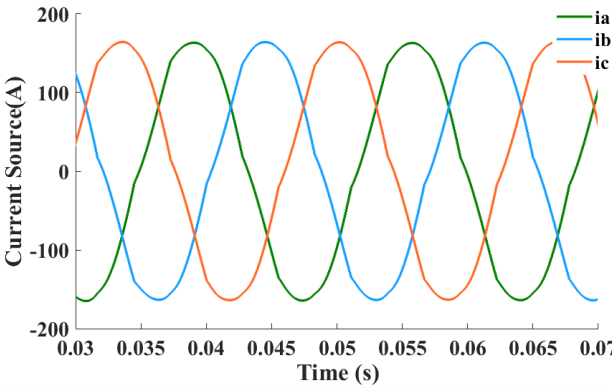

(a)

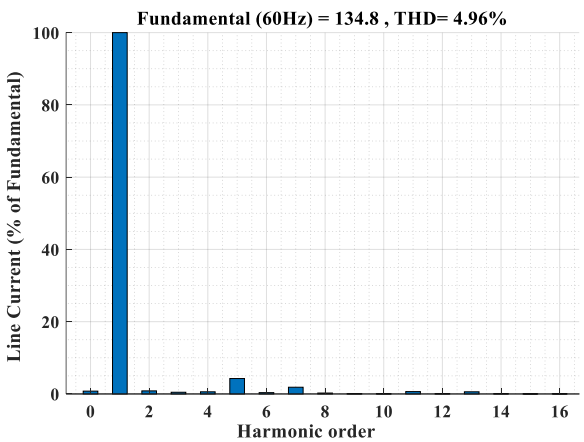

(b)

Fig. 6. The injected currents in the case of the Passive filter: a) real-time b) harmonics content.

To optimize the passive filter parameters in the hybrid filter, the meta-heuristic algorithm of SPEA-II is used. The obtained Pareto front is presented in Figure 7 for this case. The designed parameters, in this case, are presented in Table.3. Comparing results presented in Figures 3 and 8, it is clear that both objectives are improved in the case of the proposed hybrid filter.

The real-time currents and harmonics content of the injected currents to the grid in this case are depicted in Figures 8. a and b, respectively. The proposed hybrid filter not only overcome the deficiencies of high power inverter and adaptation due to changes in system parameters but also reduced the THD of the injected current to 1.75% which is very less than the threshold required standard of 5%.

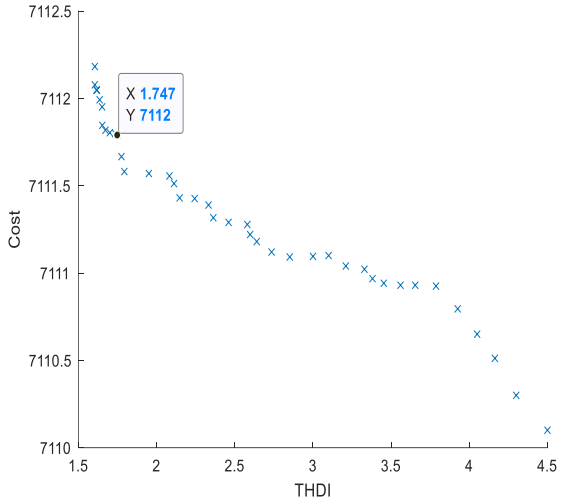

Fig. 7. Pareto front to optimize the proposed hybrid filter.

currents of the induction motor, a well-designed filter must be able to ensure high-quality currents are injected into the grid in all types of loads.

In this case, the hybrid load consists of an induction motor and a nonlinear load. The effective currents of the induction motor and the nonlinear load are 53 A and 120 A, respectively. Figure 9 shows the injected currents to the grid in real time and the frequency domain in this case. As it is measured from harmonics spectrum analysis, the THD of the injected current is 15.84% which could not satisfy the utility standards.

The above simulation is repeated adding the proposed filter in Figures 10. a and b, respectively. The proposed hybrid filter reduced the THD of the injected current to 1.22% which is very less than the threshold required standard of 5%.

The previous methods decrease THD to 3.11% [24], 2.15% [26] and 1.86% [27]. Therefore, the proposed hybrid filter profit more superiority.

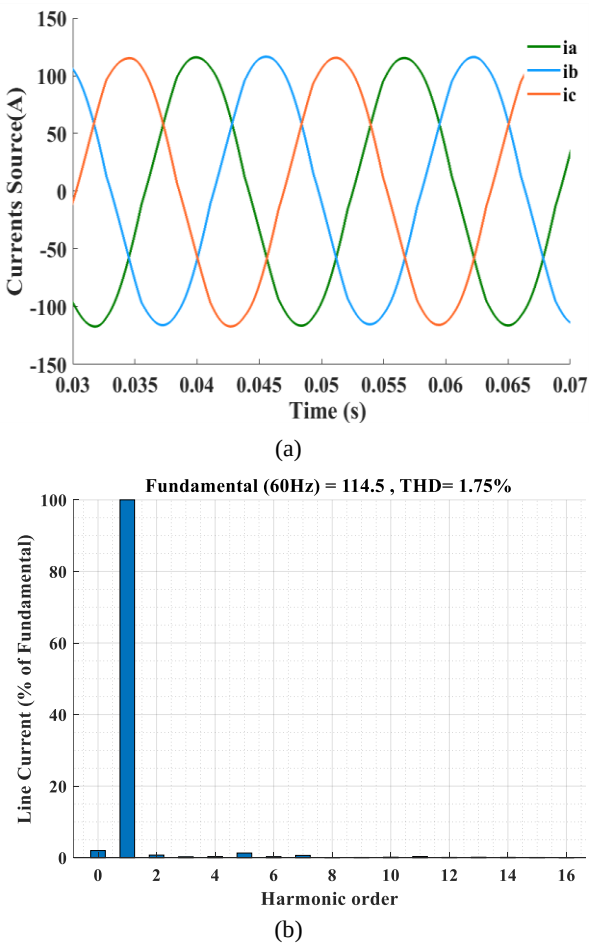

(a)

(b)

Fig. 8. The injected currents in the case of the Proposed Hybrid filter: a) real-time b) harmonics content.

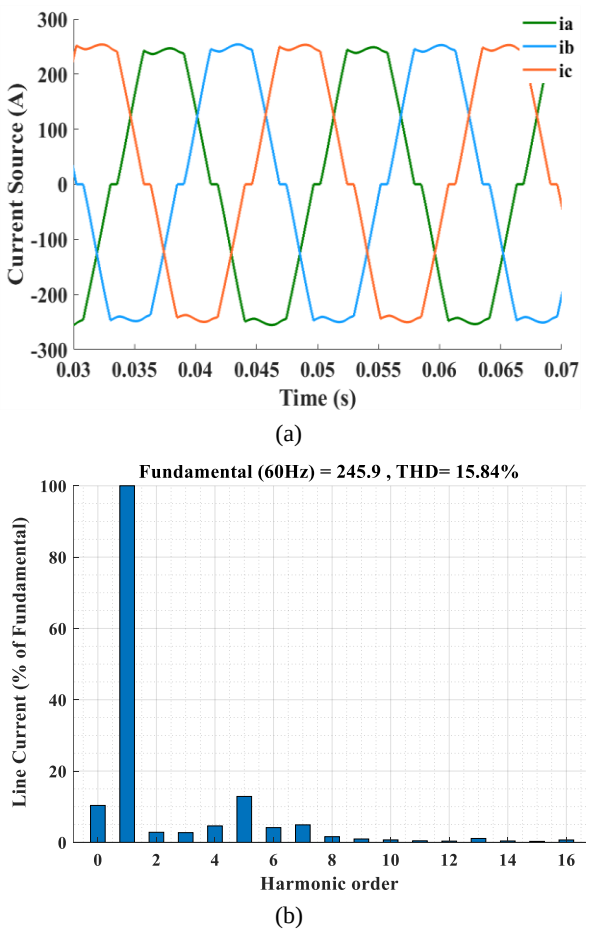

(a)

(b)

Fig. 9. The injected currents in case of the Dynamic load: a) real-time b) harmonics content.

D. Dynamic Load

To investigate the proposed filter's performance in different environments, an induction motor is added to the previous load as a dynamic load. Due to the non-sinusoidal and variable

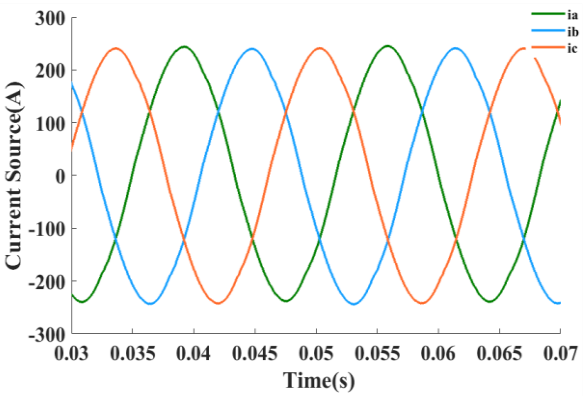

(a)

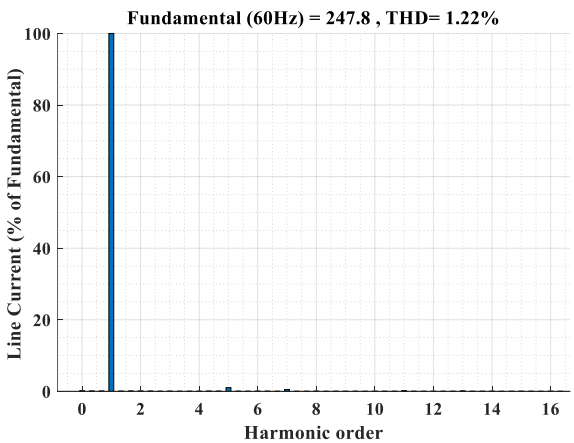

(b)

Fig. 10. The injected currents in the case of the proposed hybrid filter and dynamic load: a) real-time b) harmonics content.

V. Conclusions

In this paper, a hybrid filter is proposed based on a four-switch inverter that is decreased the power of the inverter compared with the conventional active filters. Moreover, compared with passive filters the proposed system is capable of adaptation with variations in load and grid parameters. To improve the performance of the hybrid filter, two objective functions related to current harmonics and the overall cost of the system are considered. Therefore, utilizing a four-switch inverter with two switches than the conventional structures and optimized design of the passive filter makes the proposed hybrid filter an attractive choice for selection.

The parameters of the system are optimized based on a meta-heuristic algorithm of SPEA-II. Simulation results show that the THD of the injected currents to the grid is reduced from 16.66% in the original system to 5.02%, 4.96%, and 1.75% with active, passive, and the proposed hybrid filters respectively. Therefore, the proposed filter is effective based on performance and overall cost of the system.

References

[1] S. Ronnberg, M. Bollen, Power quality issues in the electric power system of the future, Electr. J. 29 (2016) 49-61.

[2] F. N. Belchior, L. R. De Lima, P. F. Ribeiro, and J. F. C. Castro, “A novel approach towards passive filter placement,” in IEEE Power and Energy Society General Meeting, 2015, vol. 2015–Septe.

[3] Hong-Seok Song and Kwanghee Nam; “New hybrid PWM converter having APF function,” in Proc. 2001 IEEE International Symposium on Industrial Electronics Conf., pp. 1015 – 1020.

[4] S. J. Chang, H. S. Hou, and Y. K. Su, “Automated passive filter synthesis using a novel tree representation and genetic programming,” IEEE Trans. Evol. Comput., 2006.

[5] J. Yu, Y. Li, Y. Cao, and Y. Xu, “An impedance-match design scheme for inductively active power filter in distribution networks,” Int. J. Electr. Power Energy Syst., vol. 99, pp. 638–649, 2018.

[6] A. Khan, A. Gastli, and L. Ben-Brahim, “Modeling and control for new LLCL filter based grid-tied PV inverters with active power decoupling and active resonance damping capabilities,” Electr. Power Syst. Res., vol. 155, pp. 307–319, 2018.

[7] D. Li, K. Yang, Z. Q. Zhu, and Y. Qin, “A novel series power quality controller with reduced passive power filter,” IEEE Trans. Ind. Electron., vol. 64, no. 1, pp. 773–784, 2017.

[8] Abdelhamid Hamadi, Salem Rahmani, and Kamal Al-Haddad, “A Hybrid Passive Filter Configuration for VAR Control and Harmonic Compensation”, IEEE TRANSACTIONS ON INDUSTRIAL ELECTRONICS, VOL. 57, NO. 7, JULY 2010.

[9] Salem Rahmani, Abdelhamid Hamadi, Kamal Al-Haddad, and Louis A. Dessaint, “A Combination of Shunt Hybrid Power Filter and Thyristor-Controlled Reactor for Power Quality”, IEEE TRANSACTIONS ON INDUSTRIAL ELECTRONICS, VOL. 61, NO. 5, MAY 2014.

[10] Alireza Hoseinpour, S. Masoud Barakati, Reza Ghazi, “Harmonic reduction in wind turbine generators using a Shunt Active Filter based on the proposed modulation technique”, Electrical Power and Energy Systems 43 (2012) 1401-1412.

[11] Pablo Acuna, Luis Moran, Marco Rivera, Juan Dixon, and Jose Rodriguez, “Improved Active Power Filter Performance for Renewable Power Generation Systems”, IEEE TRANSACTIONS ON POWER ELECTRONICS, VOL. 29, NO. 2, FEBRUARY 2014.

[12] Anup Kumar Panda, Sushree Sangita Patnaik, “Analysis of cascaded multilevel inverters for active harmonic filtering in distribution networks”, Electrical Power and Energy Systems 66 (2015) 216-226.

[13] Leonardo R. Limongi, Luis R. Silva Filho, Luiz G. B. Genu, Fabricio Bradaschia, Marcelo C. Cavalcanti, “Transformerless Hybrid Power Filter Based on a Six-Switch Two-Leg Inverter for Improved Harmonic Compensation Performance”, Volume 62 Issue 1, Jan.-2015.

[14] Na He, Dianguo Xu, and Lina Huang “The Application of Particle Swarm Optimization to Passive and Hybrid Active Power Filter Design”, IEEE TRANSACTIONS ON INDUSTRIAL ELECTRONICS, VOL. 56, NO. 8, AUGUST 2009.

[15] Nor H.B. Abdul Kahar, Ahmed F. Zobaa, “Application of mixed integer distributed ant colony optimization to the design of undamped single-tuned passive filters based harmonics mitigation”, Swarm and Evolutionary

Computation xxx (2017) 1–13.
[16] Shady H.E. Abdel Aleem, Ahmed F. Zobaa, Murat E. Balci, “Optimal resonance-free third-order high-pass filters based on minimization of the total cost of the filters using Crow Search Algorithm”, Electric Power Systems Research 151 (2017) 381-394.
[17] Mohammad Rasol Jannesar, Alireza Sedighi, Mehdi Savaghebi, Amjad Anvari-Moghaddam, Josep M. Guerrero, “Optimal probabilistic planning of passive harmonic filters in distribution networks with high penetration of photovoltaic generation”, Electrical Power and Energy Systems 110 (2019) 332-348.
[18] C. Gong, W. -K. Sou and C. -S. Lam, "H∞ optimal control design of static var compensator coupling hybrid active power filter based on harmonic state-space modeling," in CPSS Transactions on Power Electronics and Applications, vol. 6, no. 3, pp. 227-234, Sept. 2021, doi: 10.24295/CPSSTPEA.2021.00021.
[19] Y. Wu, R. Chen, C. Li, L. Zhang, and W. Dai, "An Adaptive Sine-Cosine Moth-Flame Optimization Algorithm for Parameter Identification of Hybrid Active Power Filters in Power Systems," in IEEE Access, vol. 8, pp. 156378-156393, 2020, doi: 10.1109/ACCESS.2020.3005717.
[20] A. K. Mishra, S. R. Das, P. K. Ray, R. K. Mallick, A. Mohanty, and D. K. Mishra, "PSO-GWO Optimized Fractional Order PID Based Hybrid Shunt Active Power Filter for Power Quality Improvements," in IEEE Access, vol. 8, pp. 74497-74512, 2020, doi: 10.1109/ACCESS.2020.2988611.
[21] M. -C. Wong, Y. Pang, Z. Xiang, L. Wang and C. -S. Lam, "Assessment of Active and Hybrid Power Filters Under Space Vector Modulation," in IEEE Transactions on Power Electronics, vol. 36, no. 3, pp. 2947-2963, March 2021, doi: 10.1109/TPEL.2020.3017750.
[22] J. Huang, C. Li, Z. Cui, L. Zhang, and W. Dai, "An Improved Grasshopper Optimization Algorithm for Optimizing Hybrid Active Power Filters’ Parameters," in IEEE Access, vol. 8, pp. 137004-137018, 2020, doi: 10.1109/ACCESS.2020.3007602.
[23] W. -K. Sou, P. -I. Chan, C. Gong and C. -S. Lam, "Finite-Set Model Predictive Control for Hybrid Active Power Filter," in IEEE Transactions on Industrial Electronics, vol. 70, no. 1, pp. 52-64, Jan. 2023, doi: 10.1109/TIE.2022.3146550.
[24] E. Akbari, A.Zare Ghaleh Seyyedi, "Power quality enhancement of distribution grid using a photovoltaic based hybrid active power filter with three-level converter," Ennergy reports, pp. 5432-5448, 2023.
[25] R. Venkatesh, R. Anandhakumar, G. Renukadevi, "THD reduction in measurement of H - Bridge multilevel inverter using pulse modulated switching integrated with linear quadratic Regulator," Measurement sensor, pp.1-9, 2022.
[26] A. Hosseinpour and M. Mukti Sadeq "Harmonic reduction of current by using phase shifting and shunt-active filter trained by fuzzy particle swarm optimization" International journal of fuzzy system, Vol. 24, pp. 2729-2739, 2022.
[27] A. Hosseinpour and R. Ghazi "Using of a three-phase four-switch inverter equipped with a variable index PWM to improve the power quality of a wind power plant" International Journal of industrial electronics control and Optimization, Vol. 3, No. 3, pp. 213-222, July 2020.
[28] A. Hoseinpour "Three phases active filter with four switching inverter and variable index modulation" IEEE Power Quality Conference September 2010
[29] Ruifeng Shi, Kwang Y. Lee, “Multi-Objective Optimization of Electric Vehicle Fast Charging Stations With Spea-II”, International Federation of Automatic Control (2015) 535-540.

Poorya Rahmati Kahkha was born in Zabol, Iran in 1994. He received his B.Sc. degree with honors from University of Zabol, Iran in 2017. In 2021, he received his M.Sc. degree with honor from the University of Zabol, Iran. His main research interests are renewable energy, four-switch three-phase inverter and power electronic. He had done a great project on the application of the four-switch and six-switch optimized inverter in wind turbine.

Alireza Hoseinpour was born in Zabol, Iran in 1985. He received his B.Sc. degree with honors from Sistan and Baluchestan University of Zahedan, Iran in 2007. In 2010, he received his M.Sc. degree from the Ferdowsi University of Mashhad, Iran and Ph.D. degree in 2018 from the Shiraz University of Technology all in electrical engineering. Following receipt of the Ph.D. degree, he joined the University of Zabol, Iran. His main research interests are wind turbine, renewable energy, permanent magnet synchronous machine drive, four-switch three-phase inverter, power electronic, and design of hybrid electrical vehicle.

Ahmad Khajeh was born in Zabol, Iran in 1982. He received the B.Eng. degree from Sistan and Baluchestan University, Zahedan, Iran, in 2004 and the M.Eng. and Ph.D. degrees from the AmirkabirUniversity of Technology and Ferdowsi University of Mashhad, Iran in 2007 and 2014, all in electrical engineering, respectively. Currently, he is an Assistant Professor with the Faculty of Electrical and Computer Engineering, University of Sistan and Baluchestan, Zahedan, Iran. His current research interests include power electronics, wind power, adjustable speed drives, and photovoltaic system.

IECO

This page intentionally left blank.

International Journal Of
Industrial Electronics Control and Optimization
Print ISSN: 3517-2645
Online ISSN: 3568-2645
Homepage: https://ieco.usb.ac.ir/

Thermal Comfort-Based Heat Pumps Utilization for Wind Power Uncertainty Management

Mohammadmehdi Sedaghatzadeh[1] | Mohsen Gitizadeh[2] Saeed Hasanvand[3]

Department of Electrical and Electronics Engineering, Shiraz University of Technology, Shiraz, Iran[1,2].
Department of Electrical Engineering, Firouzabad Institute of Higher Education, Firouzabad, Fars, Iran[3].
Corresponding author's email: Gitizadeh@sutech.ac.ir

Article Info

Article type:
Research Article

Article history:
Received: 2023- February-24
Received in revised form: 2023- June-09
Accepted: 2023- June-1
Published online: 2023- June-1

Keywords:
Congestion,
Distribution system,
IGDT
Renewable energy,
Uncertainty management,

ABSTRACT

Objective: Demand response programs (DRPs) are considered a promising solution to address the variability and uncertainty of renewable generations. Heat pumps (HPs) as responsive loads are prone to participate in DRPs. HPs participation in DRPs will lead to changes in the buildings' temperature and, correspondingly, the occupants' thermal comfort (OTC). If these programs are not planned wisely, HPs owners' tendency to participate in DRPs will reduce, and power system operators will be deprived of the DRPs benefits. This work proposes a new ASHRAE55-based framework to guarantee the OTC. Information gap decision theory (IGDT) is also used to address the uncertainty of renewable generation. Then, an objective function is defined to simultaneously optimize the power consumption of HPs and the uncertainty of wind turbine generators. To find the optimal solution, the standard and adaptive fuzzy PSO algorithms are used. For determining the participation of HPs in the DRPs, there is a conventional scenario in which the temperature of each residence should be limited to the range defined by the occupant(s). The simulation results verify the superiority of the proposed scenario over the conventional one.

Nomenclature

DG	Distributed generation
DSO	Distribution system operator
$DRPs$	Demand response programs
DLC	Direct load control
HPs	Heat pumps
$IGDT$	Information gap decision theory
MIT	Massachusetts Institute of Technology
OTC	Occupants' thermal comfort
PMV	Predicted mean Vote
PSO	Particle swarm optimization process
RA	Risk-averse strategy
RS	Risk-seeker strategy
$TABS$	Thermally Activated Building System
VFD	Variable frequency drive
$VSHPs$	Variable speed heat pumps
$TABS$	Thermally Activated Building System
VFD	Variable frequency drive
$VSHPs$	Variable speed heat pumps
WT	Wind turbin
A	Area of room surface (m^2)
COP	Compressor coefficient of performance
csh_c	Specific heat capacity [J/kg.K]
h	Convective heat transfer coefficient [W/(m2.K)]
Icl	Clothing insulation[m2°C/W]
k	Clothing insulation[m2°C/W]
k_ω, k_C, k_e	VSHP steady state linear model coefficients
L	Thickness of the room surface (m)
k_{offset}	VSHP steady state linear model coefficients

R_{cv}	Convective resistance[m2 K w-1]	X	Vector of decision variables
R_{cd}	Conductive resistance[m2 K w-1]	$\bar{\psi}$	Predicted value of the uncertain parameter
T_{e-air}	Ambient temperature [°C]	ψ	Realized value of the uncertain parameter
T_{C-amb}	Outdoor air temperature [°C]	α	Uncertain radius of uncertainty
ρ	Density of the surface materials [kg/m3]]	$\hat{\alpha}$	Maximum radius of uncertainty
ω_r	Compressor speed [rad/s]	H	Vector of inequality constraints
$P_{HPs,n}$	Heat pumps consumption in bus no.n [kW]	Γ	Set of all equality and inequality constraints
P_{min}	Heat pump minimum consumption [kW]]	G	Vector of equality constraints
P_{max}	Heat pump maximum consumption [kW]	Λ	Critical value of the objective function
P_{max}	Heat pump maximum consumption [kW]	P_{net}	Network power provision [kW]
$P_{T_{min}}$	Heat pump consumption correlated to T_{min}[kW]	P_{loss}	Network power loss[kW]
$P_{T_{ideal}}$	Heat pump consumption correlated to T_{ideal}[kW]	P_{HPs}	HPs power consumption[kW]
T_{min}	Indoor air temperature correlated to PMV=-0.5 [℃]	$\overline{W_T}$	Predicted value of the WT active power generation
T_{ideal}	Indoor air temperature correlated to PMV=0 [℃]	CI	Congestion index [MVA]
T_{max}	Indoor air temperature correlated to PMV=+0.5 [℃]	CI_C	Critical value of the CI [MVA]
f	Objective function	S_L	Power flow in line L [MVA]
		S_{Lmax}	Maximum power flow in line L [MVA]
		M	Metabolic Rate[met]
		P_m	Compressor mechanical input power [kW]
		Q_{hp}	Heat pump thermal energy [kW]

I. Introduction

The global warming phenomenon and its devastating effects have compelled many countries to sign international agreements to clear the way for the world's energy policy. The Paris Agreement [1] is a landmark in this regard. Decarbonizing the power sector by increasing the integration of renewable energy and electrification of transportation and heating/cooling sectors should be considered as two steps to implement the agreements. Solar photovoltaic and wind turbines have experienced the fastest expansion among different renewable generation technologies. These technologies accounted for 90% of the new renewable generating capacity in 2022. However, the rising penetration level of renewable energy sources leads to the mismatch between renewable supply and demand because of the unpredictable and variable nature of wind and solar resources. One option to address the problem is to shift the paradigm of energy use and production from "production p Within the UK domestic sector, space and water heating comprise 80% of the energy consumption. Furthermore, by 2030, the UK might have 9 million Heat Pumps (HPs), shifting a portion of heating energy resources from gas to electricity. A survey found that nearly 90 percent of American households have HPs of some sort; hence, these loads have a high potential to be deployed by demand response programs (DRPs).ursuing demand" to "demand pursuing generation". Therefore, one promising DRPs option is HPs consumption control for managing the uncertainty and curtailment of renewable energy resources [2, 3]. This paper investigates the effect of using HPs in managing wind power uncertainty. Controlling the consumption of HPs in the form of DRPs affects the temperature of people's living/working environment and their thermal comfort.

Therefore, the thermodynamic model of residences should also be considered. Since a few numbers of papers simultaneously examined three topics including the OTC, uncertainty management, and buildings thermal networks, the review of references has three subsections including uncertainty management, OTC, and thermodynamic models of buildings.

a) OTC related publications: From the OTC perspective, three different visions were investigated by authors:

• Feedback based: In this category, the data from an experimental room provided the main foundation of the method. With the aid of a supervisory control strategy called smart zoning in every room of the building, set points were regulated so that the whole building's performance was optimized from energy consumption and OTC perspectives [4]. In [5], a two-level supervisory closed-loop feedback strategy was exploited. At the first level, each building used a local closed-loop feedback controller that only analyzed local measurements; at the upper level, a centralized unit monitored

updated the local controllers to optimize energy cost and thermal comfort. Anand et al. [6] utilized three occupancy-based HPs operational strategies to optimize energy consumption and indoor air quality when a typical variable air volume system served multiple zones inside a building. Based on the duration residents occupied a specific room, the amount of air entering the area and the temperature were set. In the abovementioned references, OTC was utilized only to prove the effectiveness of the proposed methods and not as their foundation. Moreover, the main reason for HPs introduction into electrical surveys is their remedial capability in the future operational issues of renewable-dominated energy systems. Therefore, ignoring operational objectives, constraints, and interactions of these loads with power systems (especially low-voltage grids) would not be appropriate. Moreover, as each occupant would have his behavior or each room in a building could have a different occupancy pattern, the control algorithm will be too elaborate for distribution system operator (DSO) or load aggregator to adopt for a large number of HPs.

• Consumer ideal temperature range: For the day-ahead and intra-day scheduling of the operation of heating units within a city section, Diekerh et al. [7] used a hierarchical robust distributed optimization algorithm. The paper concentrated on optimization methods, and each consumer introduced a separate objective function (OF) to be optimized. In [8], considering self-defined occupant thermal comfort, a mixed-integer linear programming approach provided optimal scheduling for electrical loads in a smart building. The OTC defined the degree of flexibility offered by the HPs. A consumer could define the degree of flexibility; however, it should be determined by the DSO so that OTC is assured while operational and power market issues are managed. Marco Pau [9] quantified customer flexibility with an optimization method. Each consumer introduced an ideal range for temperature variations.

• OTC ignorance: An economic model of predictive control was proposed in [10] to explore how district heating companies can use power-to-heat devices and traditional central cogeneration to balance the generation and consumption of electric energy in smart grids. The authors of [11] proposed a method that controls HPs based on local price to avoid the overload in systems; however, they ignored the OTC. Mendeza et al. [12] represented a control model for HPs. DR signals from the power market altered the loads' thermal setting to improve the magnitude of the network voltage; however, the effect of HPs set points alteration on the OTC was not investigated. The authors of [13] introduced an aggregated electro-thermal model for a group of houses. Energy consumption moved in time to balance the grid. Thermal discomfort was permitted. They considered large energy storage capacities to shift energy consumption to the periods in which high penetration of renewable energy sources happened. In [14], no calculation was carried out to understand if users-defined thermal comfort is following their real thermal needs. An optimization procedure achieved coincident power peak shaving in the distribution grid and provided the required thermal comfort for end-users. Kim et al. [15] modeled the thermal dynamics of variable speed heat pumps (VSHPs) using a set of piecewise linear equations for two different methods of room temperature control; however, the results were so contingent upon how an occupant defined his suitable thermal comfort. Abyaneh et al. [16] introduced a probabilistic nonlinear model for maximizing multi-energy storage and demand response flexibility. The proposed model has provided adjusted temperatures for consumers. The temperature was not based on occupants' real thermal needs, and no specific index was proposed for evaluating the OTC.

• b) Uncertainty related studies: In [17], to obtain the optimal locations of wind power plant installation, the uncertainty of electrical loads and wind power and their correlation have been considered. Considering the correlation between hourly loads and wind power variations mitigates the mismatch between the load profile and wind power. Malekijavan et al. have proposed a method to optimize the operating and reliability costs of an energy hub while considering uncertainties of loads, energy price, electrical vehicle demand, and equipment availability [18]. In this study, the OTC is ignored to be considered as a constraint in the optimization problem. In [19] micro-grid operation was optimized by considering reliability, flexibility, and environmental constraints. In this study, the renewable energy generation uncertainty was addressed using stochastic programming. The optimal energy management and operation of networked microgrids using dispatchable (fuel cell and microturbine) and non-dispatchable units (wind turbine and solar units) have been investigated by Vosoogh et al. [20]. In this study, a stochastic framework has been utilized to solve the optimal economic dispatch of the units and investigate the uncertainty effects of renewable energy resources, electric vehicles, and load demand. The abovementioned references utilize stochastic planning methods to deal with uncertainties of renewable generations which were not as helpful as the IGDT when micro-grids are subject to severe uncertainty. In [21] a multi-timescale economic scheduling model considering the uncertainty of wind power has been proposed. Day-ahead, intraday, and real-time scheduling periods were considered in which wind power prediction accuracy was improved, and optimal planning was carried out using the appropriate methods. In the presented model, the prediction error range must be specified in advance. Otherwise, the model will not be applicable, and the IGDT should be substituted for the proposed method. In [22], the interval optimization method considers the uncertainty of wind power and photovoltaic units in a combined cooling, heating, and power system. The advantage of this study is that, in addition to the energy cost, carbon oxide emissions are also minimized. The interval

optimization method requires the lower and upper limits of uncertainty parameters. So, this method is impossible to implement without knowing these boundaries. Authors in [23] minimize the total energy cost of the multi-carrier microgrids and decrease CO2 emission rates by considering HPs. Uncertainties associated with a wind turbine (WT), electrical loads, electricity market price, and behavior of the electric vehicle are considered. Coelho et al. propose an optimization model to use the flexibility of multi-energy systems to mitigate the uncertainty associated with wind generation [24]. Correa et al. present an optimization model for home energy management systems while the uncertainty of energy prices, PV production, and load are considered [25]. OTC has been ignored in all the above-mentioned references. Probability density or the membership function-based, IGDT-based and hybrid-based frameworks were proposed in researches to deal with the renewable energy resources uncertainty. In a network with severe uncertainty in the wind power profile, the IGDT-based method was proved to be more effective with less computational burden [26]. In [27], a hybrid stochastic/IGDT approach is utilized to optimally schedule a wind-based energy hub and manage the electricity price uncertainty while the OTC was ignored. Murphy et al. study both opportunistic and conservative effects of a WT uncertain generation on the standard distribution system congestion [28]. Fixed integrated pre-determined multi-level of load flexibility has been assigned to the nodes (one node for each level of flexibility) with the dominant effect on the congestion (as the OF) to exhibit the effectiveness of the DRPs on uncertainty management problem. A two-step optimal operating procedure for a community-integrated energy system was presented by Wang et al., addressing multiple uncertainties and integrated demand response [29]. In [30], a stochastic framework for residential energy management in multi-carrier buildings has been proposed. Thermal and electrical loads are categorized as price-responsive and non-responsive loads. The authors of [31] consider the electrical chiller as the cooling supplier of an office building. A two-step hierarchical microgrid energy management method for an office building is proposed that accounts for uncertainties from renewable generation, electric load demand, outdoor temperature, and solar irradiance while ignoring the OTC impacts on the system flexibility. A resilience-oriented stochastic framework considering integrated demand response is proposed in [32] to improve the overall economy and system resiliency, whereas HPs' high potential for managing uncertainty is ignored.

- c) Thermodynamic models for buildings: Simplified dynamic models of buildings are gaining more and more attention recently. TABULA and EPISCOPE are two European projects that provided a compatible structure for classifying building types and constructing building archetypes based on statistical analyses of large building samples [33]. Detailed analyses of buildings' models are proposed in [34-36] as well as international standard ISO 13790 and the German Guideline VDI 6007. The system domain in these models is approximated by a series of nodes connected by thermal resistances and capacitances. Their main advantage is that once the parameters are identified, the system can be solved analytically, avoiding the problems that arise in numerical schemes. In [34] an elaborated thermodynamic model of an experimental room is introduced. The reference did not study the distribution system operational limits and system-wide effects of HPs consumption alteration. The model is developed in [35] for HPs control methods investigations. In [36], reduced-order thermal response models of twelve representative German building types in three insulation states were proposed. The DRPs potential of the buildings' structural thermal mass (called passive storage) was used in two predefined cases. In the discharge case, HPs are actively switched off, while the heat demand is covered by the passive storage discharge. In charge case, HPs are actively switched on regardless of the current heat requirements by overheating the passive storage. HPs have an on-off controller which is an old control method and could create power quality consequences, especially if the degree of HPs penetration grows in the future; 20℃ to 22℃ is considered as the comfort band without introducing any criterion.

In the abovementioned references, RC models are used for the electro-thermal simulation of buildings. Consequently, each model can be selected to demonstrate the effectiveness of the proposed method in WT uncertainty management. The thermal network introduced in [34] is a thermodynamic model modified for electrical applications. Therefore, the model is utilized by this paper for the investigations of the building's thermal behavior.

ASHRAE55 standard [37-38] creates a framework for the OTC determination that depends on occupants' physical and environmental status. In other words, this standard will transform the OTC from a personal interpretation-based factor to a measurable and calculable one. This work evaluates temperature ranges that guarantee the OTC. Consequently, DSO would count on steady and maximum HPs flexibility to overcome operational problems and postpone low voltage grids' future expansion. HPs consumption is a decision variable in this work's optimization algorithm rather than the source of uncertainty. HPs consumption control is considered a tool to save/benefit the DSO and the low voltage network to a specific level of decrease/increase in the WT power generation. Finally, DSO with direct load control (DLC) signals changes HPs set points or consumption in each bus of the test system. The contributions of this study are summarized as follows:

- Based on the ASHRAE55 standard and RC-network representations of examined building models, a new OTC-ensured HPs DRPs participation framework is proposed to introduce the loads as tools of WT uncertainty management.

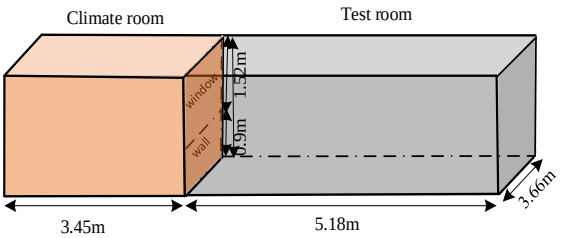

Fig1. Experimental room.

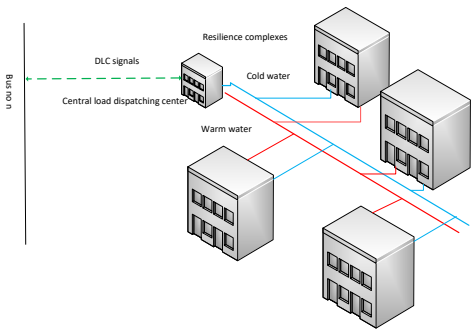

Fig2. Heat loads in a bus.

• The core of the IGDT method is an OF which is used for optimizing the permissible renewable energy forecast error.

This work adds a HPs consumption-related term to the function which has a positive influence on the forecast.

The rest of this paper is organized as follows. System modeling, thermal comfort and calculation of OTC-assured HPs consumption boundary are explained in section 2. The IGDT and optimization process are proposed in section 3. Simulation results are depicted in section 4. Finally, the conclusion is drawn in the last section.

II. System modeling

A. MIT experimental room' thermal network

The building is located at MIT and divided into two parts: Climate Room and Test Room. The outdoor temperature changes are simulated by changing the climate room temperature. The test room is equipped with Thermally Activated Building System (TABS) ventilation system (Fig.1). The system provides resilience complexes with warm water. Hot water pipes pass through the floor. The walls are made of layers of thermal insulation and concrete. Each layer is defined by its thickness, thermal conductivity, specific heat capacity, and density. The test room has a heater and lighting. The heat generated by these sources simulates thermal losses.

In this work, DLC signals, via a Variable Frequency Drive (VFD), control compressor speed, rate of the working fluid, and power consumption of a VSHP in a central load dispatching center or local control center (Fig.2). The signals are applied according to the DSO operational /power market goals, while the indoor air temperature is maintained at hourly based, OTC-assured limits. All residents' complexes are assumed to have the same structure as the experimental room.

In Fig.3 thermal network of the room is introduced. Conductive and convective resistances are modeled by electrical resistances. The electrical equivalent of temperature is the voltage source, and heat gains are modeled by voltage and current sources, respectively [35]. Qhp is the thermal energy injected into the building, and Te-air is the operative temperature. The values of convective thermal resistance (Rcv), conductive thermal resistance (Rcd), and thermal capacitance (C) could be obtained via (1)-(3).

$$Rcd = L.(k.A)^{-1} \quad (1)$$

$$Rcv = (h.A)^{-1} \quad (2)$$

$$C = c_{shc}.L.A.\rho \quad (3)$$

L and A are the thickness and area of the room surface, respectively. ρ and cshc are the density and specific heat capacity of the surface materials. Also, k and h are the conductive and convective heat transfer coefficients; indeed, h is set to 5W/ (m2.K), regardless of the surface characteristics, although all the convective resistors are denoted as Rcv. All parameters in the RC model are calculated based on the experimental room characteristics proposed in [34].

B. Occupants' thermal comfort

Thermal comfort is a mental state that expresses the degree of satisfaction of a person from the thermal conditions of the environment. There are several physical parameters involved in thermal comfort. Two conditions must be fulfilled to create thermal comfort: 1-The composition of the temperature produced inside the body and the skin temperature create a neutral thermal sensation (not cold or warm), and 2- The energy balance is created in the body, which means that the heat generated by the metabolism is equal to the temperature exchanged between the body and the environment. Relationships between skin temperature parameters, the degree of heat inside the body, and the amount of physical activity create a neutral sense of warmth in experimental studies. In these experiments, transpiration rate and skin temperature are measured for different amounts of body metabolism, while the person under the test has thermal comfort in all conditions. What makes looking into thermal comfort vital is its remarkable impact on residents' satisfaction with consistent DRPs participation. Therefore, HPs DRPs will be reduced if the OTC is ignored by the DSO.

Predicted Mean Vote (PMV) is a seven-point scale for heat sensation. This index allocates a number for the degree of thermal sensation of individuals. According to an occupant's clothing, metabolism, and physical conditions, the room temperature equals a specified PMV. PMV could be positive or negative. The positive values of the table (1) are equivalent to the temperatures in which the residents feel a little heat, and the negative values of the table correspond to the temperatures that will cause the residents to feel a little cold. The ideal residence's temperature is the one that occupants feel

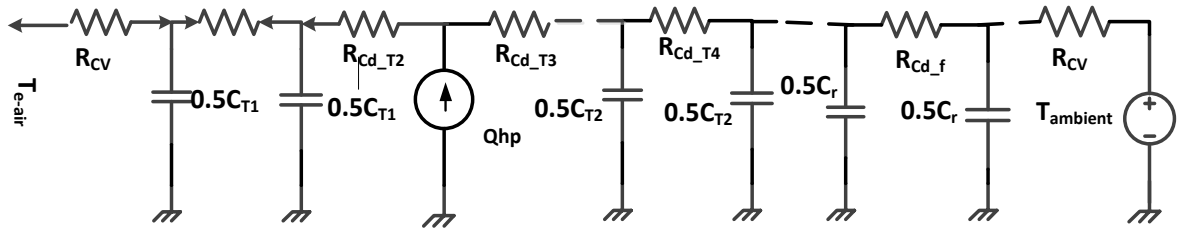

Fig.3. Electro-thermal network of the experimental room.

TABLE 1
PMV AND THERMAL SENSATION

PMV	THERMAL INDICATION
+3	Too warm
+2	Warm
+1	A little warm
0	Neutral
-1	A little cold
-2	Cold
+3	Too warm
+2	Warm
+1	A little warm
0	Neutral

thermally neutral. The ASHRAE55 standard introduces (4) as the allowable range for PMV deviation from the ideal value (PMV=0).

$$-0.5 \le PMV \le +0.5 \qquad (4)$$

In the following section, the temperature range in which the constant regulation of the indoor air temperature ensures the OTC is determined (the temperature range equivalent of (4)).

For the internal space temperature of a house, this work defines 'Tideal' as a temperature in which the PMV index is zero; 'Tmin' is the minimum permissible temperature in which PMV=-0.5 and occupants feel a tolerable sense of coldness, and 'Tmax' is the maximum allowable temperature in which PMV=+0.5 and occupants have an endurable sense of warmth. Tmin, Tmax, and Tideal are determined using a relationship between the operative temperature and PMV [37- 39].

C. OTC-assured temperature boundary

PMV equation is denoted as follows:

$$PMV = f(T_{e\_air}, t_r, M, W, I_{cl}) \qquad (5)$$

Two different groups of information should be provided:

• Occupants' physical characteristics include their metabolic rate (M), effective mechanical power (W) that is dependent on the type of activity, and thermal insulation of occupants' clothing (Icl).

• Environmental characteristics include airspeed, relative humidity, operative temperature (Te_air), and mean radiant temperature (tr). Te_air describes the combined effects of convective and radiant heat transfer, and tr shows the radiation temperature of surrounding surfaces.

Most of the needed parameters could be estimated by statistical methods. In system-wide investigations, the number of HPs is high, and each occupant would feel thermal discomfort even if the indoor temperature is maintained in the OTC-assured boundary (Eq.5); therefore, in this work, a day is divided into three time periods. In each period, all effective parameters on residents' sense of warmth, except HPs injected thermal energy (Qhp), are assumed to have minimum possible values defined by the standard (Table.2). The assumptions are:

TABLE 2
TYPICAL CLOTHING INSULATION AND ACTIVITY

Time period	ICL	Residents' clothes	M	Resident's activity
10PM-7AM	1	Typical winter indoor clothing	40	Sleeping
8AM-4PM	0.85	Long sleeve shirt	65	Typing
5PM-9PM	0.96	Sleep wear pajama tops	100	Housework
5PM-9PM	0.96	Sleep wear pajama tops	100	Housework

• The mean radiant temperature is assumed to be the minimum ASHRAE55-defined value (10℃). In this way, the effect of residents surrounding objects in heating the building is minimized; especially in the daytime, the radiant temperature is higher than 10℃, and residents' sense of warmth increases. In other words, HPs are assumed as the only means of providing thermal energy for residents.

• Tables in Appendix B of the ASHRAE55 standard are used to estimate the clothing insulation parameter (Icl). The maximum value of the parameter is 1, which represents typical winter indoor clothing. For the period between 9 PM-7 AM, Icl is assumed to be 1. Usually, at night time residents wear clothes with higher insulation values. For example, using a multi-purpose quilt and wearing full-slip sleepwear at night can raise the Icl to 4.56 [40]; the PMV and thermal sensation of occupants will be more than what is considered by the DSO.

• The parameters related to the weather have been selected based on Tehran's monthly and annual statistics [41-42].

• For 9 PM-7 AM and 5 PM-9 PM periods, archetypal activity levels (M) are supposed for occupants. From 8 AM to 4 PM, an activity with a low metabolic rate is assumed for occupants. More common daytime activities increase the metabolic rate, PMV, and occupants' thermal sensation. Based on the above assumptions and Eq.4, Tmin, Tideal, and Tmax are calculated and depicted in Fig.4.

The operative temperature should be held at the boundary

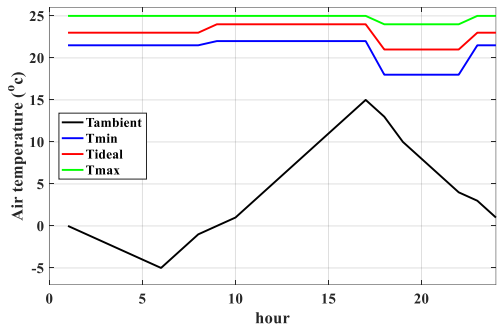

Fig4. Tmin, Tideal and Tmax in a winter day.

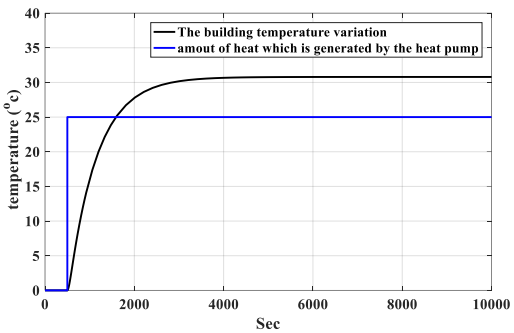

Fig. 5. *Step response of the building*.

known as the OTC-assured temperature boundary (6).

$$T_{\min} \le T_{e\_air} \le T_{\max} \quad (6)$$

D. The relationship between OTC-assured temperature boundary and VSHP power consumption

The thermal network of the experimental room can be utilized to calculate the energy needed to maintain the operative temperature in the OTC-assured boundary.

The equivalent network is a thermodynamic circuit; nonetheless, the dynamic behavior of the building model is ignored. The reason is that the presented approach in this work changes the temperature of a building in a range that, at all points, OTC is assured. In other words, in all temperature values between initial and steady-state values, the OTC is guaranteed, and HPs are exploited for handling network operational issues. Therefore, the steady-state response of the building is considered.

For example, the OTC-assured boundary is between 18°C and 21°C on a winter night. According to the step response (Fig.5), it takes 4000 sec. (nearly 1 hour) for the indoor air temperature to rise from 18°C to 21 °C and vice versa. If the DLC signal is applied an hour before the schedule (in the form of the day-ahead operational planning), then the temperature will be set at the intended value; therefore, the thermal behavior of the building between initial and steady-state values could be ignored.

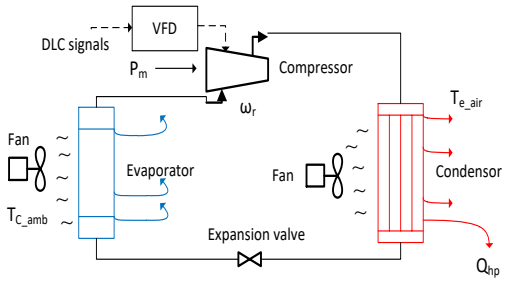

Fig. 6. Schematic diagram of a heat pump heating cycle.

E. Modeling of a DLC-enabled VSHP

Fig.6 shows that VSHP comprises an evaporator, a compressor, a condenser, and an expansion valve. The heating cycle of a heat pump extracts heat from the air outside, raises its temperature, and heats indoor air with warm air. Liquid refrigerant transforms into a gas by absorbing the outdoor air heat in the evaporator. The compressor raises the gas pressure and temperature. The hot gas passes through a condenser coil in the indoor space. Its temperature is higher than the indoor air temperature. Therefore, the gas transfers heat to the indoor space and condenses into a liquid. Eventually, the fluid passes through the expansion valve. The cycle terminates by lowering the liquid's pressure and temperature.

The shaft speed (ωr), condenser ambient temperature (TC-amb), and evaporator air temperature (Te-air) are the input variables for the VSHP model. Only ωr is controlled. Compressor mechanical power (Pm) and heat rate (Qhp) are the output variables. Additionally, the coefficient of performance (COP), which is defined as the ratio of Qhp to Pm, is used to assess the VSHP performance. The power usage of the fan is disregarded. Compression consumes the majority of the VSHP input power. VSHP has a dynamic behavior in response to the DLC signals; however, as stated earlier, the DLC signal was applied long enough before the instant of operation; therefore, in this work, a linear steady state function has been utilized for VSHP modeling (7).

$$P_m = k_\omega \omega_{r0} + k_C T_{C-amb0} + k_e T_{e-air0} + k_{offset} \quad (7)$$

In [31], multiple polynomial regressive algorithms were applied to 2210 different combinations of the input variables over typical VSHP operating points to find the coefficients kω, kC, ke, and koffset. Te-air0 is the indoor air temperature ensuring the OTC. It is determined by the PSO algorithm; Tc-amb0 is the outdoor air temperature and a known variable; therefore, the equation is deployed to find the speed ωr0 which is necessary for producing the mechanical power Pm. Subscript '0' denotes the parameter values at steady condition.

F. HPs minimum and maximum consumption calculation for winter

In this section Tideal, Tmin, and Tmax are employed to calculate the minimum and maximum HPs power consumption (Pmin and Pmax, respectively). In the following sections, Pmin and Pmax are utilized in the optimization procedure to

determine HPs flexibility in DRPs. Any value for HPs consumption between Pmin and Pmax determined by the PSO will satisfy the OTC.

In winter, if the outdoor temperature becomes lower than Tmin, then the minimum power consumption of the HPs is equal to the power needed for heating the temperature to Tmin. The maximum consumption of the HPs is the power for heating the temperature to Tideal. When the temperature is in other areas, the minimum and maximum consumption of HPs are determined using the Eq. (8).

$$P_{HP_{\max,\min}} \begin{cases} \begin{pmatrix} P_{\max} = P_{T\,ideal} \\ P_{\min} = 0 \end{pmatrix} & T_{\min} \le T \le T_{ideal} \\ P_{\max} = P_{\min} = P_{T\,ideal} & T \ge T_{ideal} \; or \; T \ge T_{\max} \end{cases} \tag{8}$$

P_(T_ideal) is the power needed to maintain indoor air temperature at Tideal.

Temperature is a constant parameter; therefore, in [35], a 'voltage source' is considered the electrical equivalent of temperature. The current source is the electrical equivalent of HPs thermal power (Qhp). In the experimental room model (Fig.3), at a specific hour, for a definite value of ambient temperature ($T_{ambient}$), a certain value of Qhp is needed for heating the building to Tmin /Tideal. T_{e_air} (the indoor air temperature) is replaced by a voltage source with the value Tmin /Tideal. HPs power consumption for generating Qhp is determined using the COP. The index is supposed to be 0.7.

G. Test network

The chosen test network under examination is a modified IEEE 33-bus test system. The technical data of the network is provided in [43]. The modification includes a WT installation in bus no.18 and 20% of HPs penetration in each bus (Fig.7).

III. Uncertainty management of renewable generations using HPs

This work introduces a decision-making framework that exploits HPs and a WT reactive power generation capability to manage the uncertainty of wind power. Occupants' thermal comfort is assured consistently. PSO is employed to determine optimized decision variables.

A. Uncertainty Modeling

The general optimization problem is defined in (9) - (11), where a series of decision variables optimize the OF. Equality and inequality constraints will limit the optimized decision variables' values.

$$\min_{X} f(X, \bar{\psi}) \tag{9}$$

$$\mathbf{H}_{n}(\mathbf{X}, \bar{\psi}) \le 0, n \in \Gamma_{ineq} \tag{10}$$

$$\mathbf{G}_{\mathbf{m}}(\mathbf{X}, \bar{\psi}) = 0, m \in \Gamma_{eq} \tag{11}$$

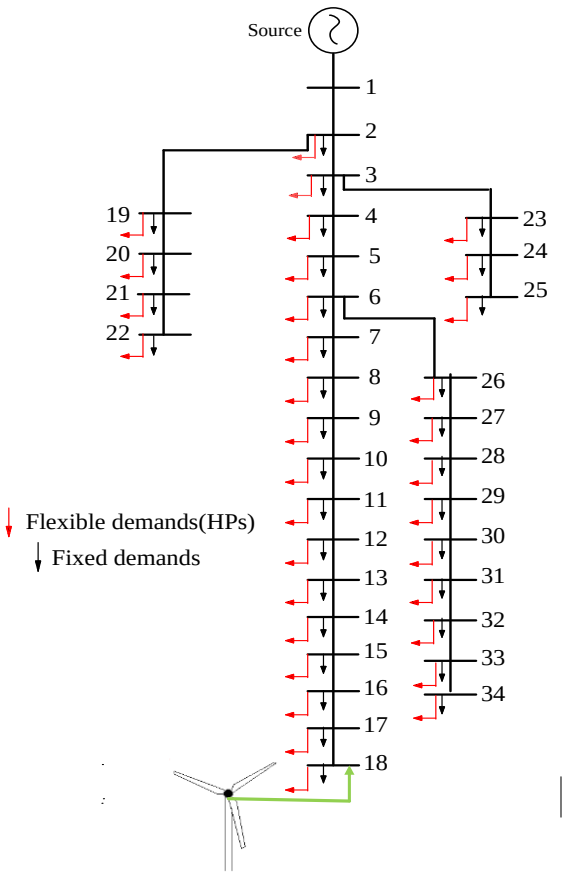

Fig7.Modified IEEE 33-bus test system.

X is the vector of decision variables, $\bar{\psi}$ is the predicted value of the uncertain parameter, Γ is the set of all constraints, H and G are the set of inequalities and equalities for the variables X.

B. IGDT Risk Averse (RA) strategy

If the OF is optimized based on $\bar{\psi}$, then underestimation of the wind forecast will deteriorate the OF from the optimized value. In this case, the DSO, as the decision maker, specifies the maximum tolerable deterioration in the optimized value of the OF(15). In return, IGDT determines X and the maximum manageable underestimation of wind forecast ($\hat{\alpha}$ in (12)). If the DSO operates the network based on the vector X, then for the uncertainty gap between zero and $\hat{\alpha}$, the value of the OF is restricted to the DSO pre-specified critical limitation (15) and all constraint equations remain true ((13) and (14)). IGDT Risk Averse (RA) strategy is formulated as:

$$\max_{\mathbf{X}} \hat{\alpha}(\mathbf{X}, \psi) \tag{12}$$

$$\mathbf{H}_{n}(\mathbf{X}, \psi) \le 0, n \in \Gamma_{ineq} \tag{13}$$

$$\mathbf{G}_{\mathbf{m}}(\mathbf{X}, \psi) = 0, m \in \Gamma_{eq} \tag{14}$$

$$\hat{\alpha} = \left\{ \max \alpha \mid \mathrm{f}(\mathbf{X}, \psi) \le \Lambda_{C} = (1+\beta_{c})\mathrm{f}_{b} \right\} \tag{15}$$

$$\psi \in \mathrm{U}(\bar{\psi}, \alpha) = \left| \frac{\psi - \bar{\psi}}{\bar{\psi}} \right| \le \alpha \tag{16}$$

C. IGDT Risk Seeker (RS) strategy

Overestimation of the wind forecast will improve the value of the OF. IGDT in the RS approach calculates a minimum value for the radius of uncertainty (17) that leads to a pre-defined improvement of the OF (20).

$$\min_{\mathbf{X}} \hat{\alpha}(\mathbf{X}, \psi) \tag{17}$$

$$\mathbf{H}_{n}(\mathbf{X}, \psi) \le 0, n \in \Gamma_{ineq} \tag{18}$$

$$\mathbf{G}_{m}(\mathbf{X}, \psi) = 0, m \in \Gamma_{eq} \tag{19}$$

$$\hat{\alpha} = \left\{ \min \alpha \mid f(\mathbf{X}, \psi) \le \Lambda_{O} = (1 - \beta_{O}) f_{b} \right\} \tag{20}$$

$$\psi \in U(\overline{\psi}, \alpha) = \left| \frac{\psi - \overline{\psi}}{\overline{\psi}} \right| \le \alpha \tag{21}$$

Λ_O as a pre-defined opportunistic limit, is hoped to be achieved when the realized values are the improved version of the forecasted ones. The expected level of the OF improvement is βo. The minimum value of α is which should be determined, while the value of the OF is kept below the parameter Λ_O.

D. Decision variables

Decision variables include HPs consumption in each bus.

E. Optimization procedure

The objective of an optimization problem is to identify a variable represented by a vector X=[x1,x2,x3,...xn] that minimizes or maximizes a cost function known as the fitness function or the objective function. The position vector, X, is an n-dimensional variable vector where n is the total number of variables in the problem. The OF evaluates the quality of a specific position vector X. Particle Swarm Optimization (PSO) is a metaheuristic optimization technique that solves challenging optimization problems with high efficiency and simplicity. However, several PSO variations exist because the performance of the normal PSO is prone to be caught in local extrema. Fuzzy logic concepts have widely improved the PSO algorithm. In this study, the performance of a modified version of PSO algorithms known as Adaptive Particularly Tunable Fuzzy Particle Swarm Optimization (APT-FPSO) is compared with the performance of the standard PSO. The standard PSO compares the outputs of this work's presented scenarios. Section 5 demonstrates that APT-FPSO produces more acceptable results than the standard PSO. In [38], PSO and in [39], APT-PSO optimization methods are, respectively, introduced. The standard PSO compares the outputs of this work's presented scenarios. Section 5 demonstrates that APT-FPSO produces more acceptable results than the standard PSO. In [38], PSO and in [39], APT-PSO optimization methods are, respectively, introduced.

PSO for each iteration generates a swarm of P position vectors (X). The velocity vector (V) moves the position vector from one iteration to the other one (toward a more optimal version).

$$\mathbf{X}_{i}^{t+1} = \mathbf{X}_{i}^{t} + \mathbf{V}_{i}^{t+1} \tag{22}$$

Identification: Uses the previous solutions, determines the best solution of a specific region.

Diversification: Looks for novel solutions and identifies areas that may have the solutions.

$$V_{i}^{t+1} = wV_{i}^{t} + c_{1}r_{1}\left(pbest_{i}^{t} - X_{i}^{t}\right) + c_{2}r_{2}\left(gbest^{t} - X_{i}^{t}\right) \tag{23}$$

Inertia: Makes particles move in the same direction and at the same speed.

Personal influence: Improves the individual. Using the previous position

Social influence: Makes the particle follow the best neighbors' direction

The parameter w is the inertia weight with a positive constant. The parameter balances the global and local searches. The first search is known as exploration, and the second search is known as exploitation. Higher values of w dominate exploration; however, lower values of the parameter dominate exploitation. $pbest_i^t$ is the personal best record of the ith particle in the t^{th} iteration, and $gbest^t$ is the global best in the tth iteration; r_1 and r_2 are random numbers within the range [0; 1]; c_1 and c_2 and are constants known as the personal and global learning coefficients, respectively.

F. The developed adaptive particularly tunable fuzzy PSO algorithm

As already mentioned, the standard PSO variants have facilitated the algorithm from premature convergence phenomena. The main objective of PSO variants is to achieve an adaptive, dynamic, well-balanced strategy for adjusting PSO's setting parameters during exploration and exploitation. Fuzzy Adaptive algorithms are more useful than other variants of the PSO. They utilize fuzzy logic concepts to tune the setting parameters of the PSO algorithm adaptively and dynamically. The Adaptive Particularly Tunable Fuzzy Particle Swarm Optimization (APT-FPSO) proposes the best strategy for balancing between exploration and exploitation [46]. Section IV demonstrates that APT-FPSO produces more acceptable results than the standard PSO. In [44], PSO and in [45], APT-PSO optimization methods are, respectively, introduced. The standard PSO compares the outputs of this work's presented scenarios.

The Mamdani fuzzy inference system (FIS) has two inputs. The first input normalizes the iterations (NIt) from the start (NIt = 0) to the end (NIt = 1) of the algorithm. Eq. (24) represents the normalized iterations.

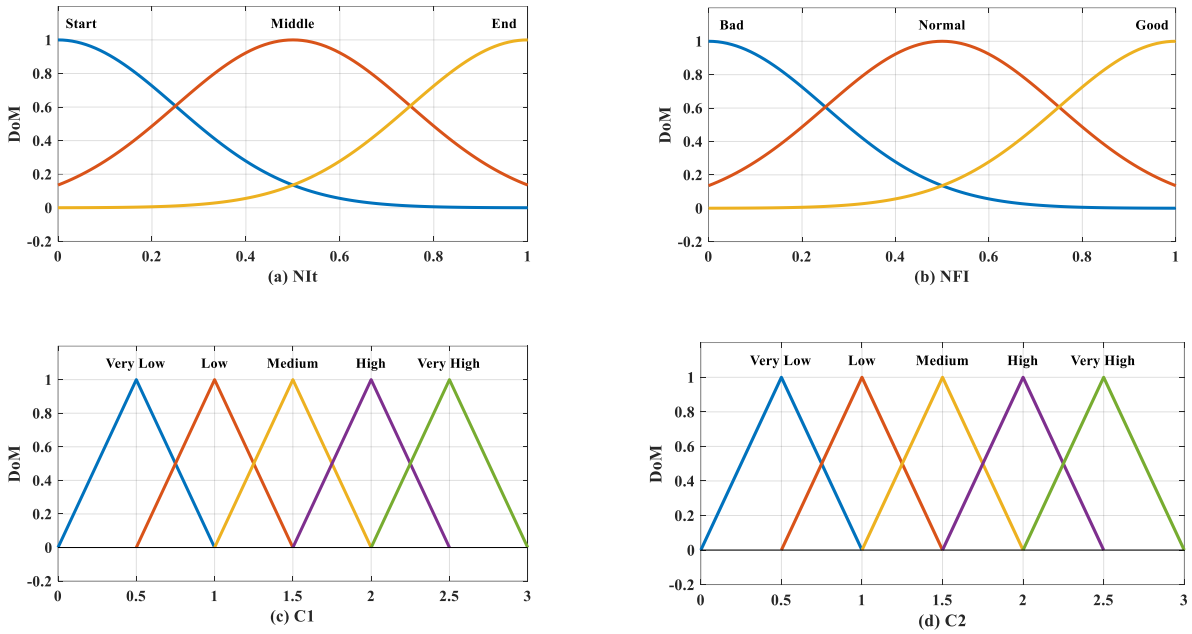

Fig.8 Membership functions of inputs (a, b) and outputs (c, d) of the developed FIS

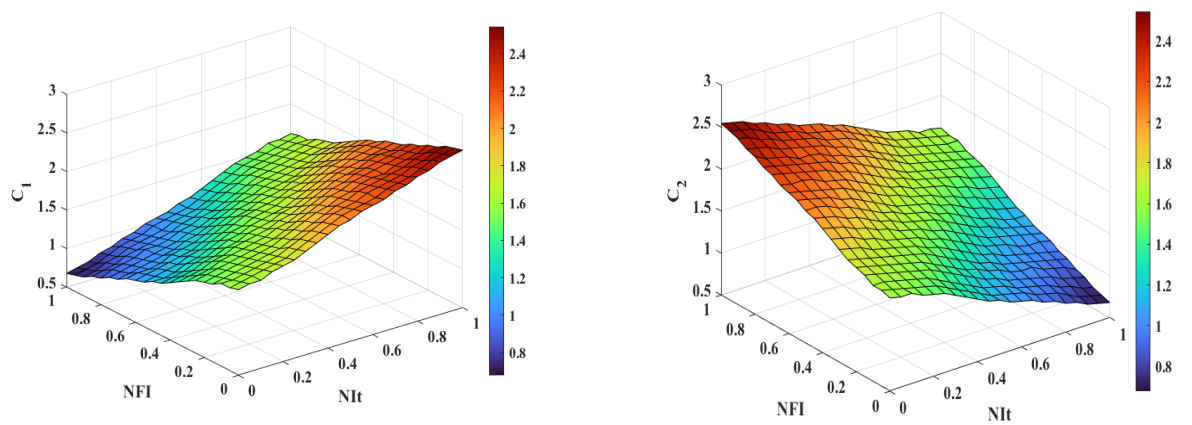

(a) (b)

Fig9. Surfaces of the inputs and the outputs for the rule-base structure No.1.

$$NIt = \frac{\text{Current iteration}}{\text{Maximum number of iterations}} \quad (24)$$

Three linguistic variables "Low", "Medium", and "High" and corresponding three Gaussian Membership Functions (MFs) fuzzify the normalized iterations. The second input of the developed FIS is the fitness value of each particle. The APT-FPSO algorithm uses the best and worst swarm fitness values at each iteration to normalize particle fitness. (25) formulates the normalized fitness index (NFI).

$$NFI = \frac{fitness_{t,i} - \min(fitness_t)}{\max(fitness_t) - \min(fitness_t)} \quad (25)$$

$fitness_{t,i}$ is the fitness value of the i^{th} particle in the t^{th} iteration. The $\max(fitness_t)$ and $\min(fitness_t)$ are the maximum and minimum fitness values of the swarm in the t^{th} iteration, respectively. Three Gaussian MFs are the second input NIt linguistically called low, medium, and high. Fig. 8 (a) and Fig.8 (b) indicate the inputs of the developed FIS. The outputs of the proposed FIS are personal and global learning coefficients, i.e., $c_{1,t}^{i}$ and $c_{2,t}^{i}$. Their values are proved to be within the range [0.5, 2.5] in [41, 42]. $c_{1,t}^{i}$ and $c_{2,t}^{i}$ are the learning coefficients of c_1 and c_2 for the i^{th} particle in the t^{th} iteration respectively. Five triangular MFs represent the outputs of the developed FIS known as, very low, low, medium, high, and very high ($c_{1,t}^{i}$ and $c_{2,t}^{i}$). Briefly, the developed FIS

has normalized iteration and normalized fitness index as the inputs, and two outputs known as $c_{1,t}^{i}$ and $c_{2,t}^{i}$.

The outputs of the algorithm are shown in Fig.8(c) and Fig.8(d) For the proposed inputs and outputs, many rule bases can be introduced with unique performances. The rule-base surfaces utilized by this work are shown in Fig.9.

G. Objective function

In this work, the OF is formulated as:

$$f(X, W_T, \beta) = k_1 \left| \sum_{n=2}^{33} \left(\frac{P_{HPs,n}}{P_{DR0,n}} \right) \right| + k_2 W_T + G \quad (26)$$

$P_{HPs,n}$ is the optimized consumption of HPs in bus No.n. $P_{DR0,n}$ shows the consumption of the loads when HPs offer no flexibility in bus No.n. G is a penalty factor which is a linear summation of constraints. PSO minimizes both terms in (26). The PSO utilizes HPs DRPs participation minimizing the first term. The second term is the IGDT OF and is defined as follows:

$$W_T = (1-\alpha)\overline{W}_T \quad (27)$$

$$W_T = (1+\alpha)\overline{W}_T \quad (28)$$

In RA and RS strategies, WT, as the realized value of the uncertain parameter, is related to the forecasted value by (27) and (28). $\overline{W}_T$ is the wind power predicted value.

H. Constraints

• *IGDT constraints*: Critical and opportunistic values of CI are utilized as the DSO or the decision maker inputs to the IGDT-based PSO algorithm ((29) and (30)).

$$\Lambda_C = CI_c = (1+\beta)CI = (1+\beta)\sum_{L=1}^{32} S_L \quad (29)$$

$$\Lambda_O = CI_O = (1-\beta)CI = (1-\beta)\sum_{L=1}^{32} S_L \quad (30)$$

• The power flow constraint: The power flow equation ensures that the power which the network and the WT provide (P_{net} and P_{WT}, respectively) is equal to the summation of HPs consumption (P_{HPs}) and the network power loss (P_{loss}).

$$P_{net} + P_{WT} = P_{HPs} + P_{loss} \quad (31)$$

• The operating limits of WT, HPs and bus voltages: The OTC-assured operating limit of HPs is (32). Safe operating limit for bus voltages is formulated in (33).

$$P_{min} \le P_{HPs} \le P_{max} \quad (32)$$

$$0.9\,pu \le V_{busj} \le 1.1\,pu \quad (33)$$

I. The role of heat pumps in uncertainty management

The decision maker (DSO) defines specific values for the indices Λc, Λo, or β. Moreover, the limitations denoted in section 4.9.2, are inequality constraints of the optimization algorithm (the flowchart in Appendix A). The OF optimizes HPs consumption and the radius of uncertainty(α) simultaneously. Sections 4.9.2 and 4.9.3 prove that placing the term related to HPs consumption along with the one related to the IGDT will improve the output of the theory in both RA and RS strategies

J. RA strategy

For each iteration of the PSO, after determining the population, the Congestion Index (CI) is calculated by carrying out power flow while the constraint provided by the IGDT is examined (34).

$$CI < \Lambda_C or \Lambda_O \quad (34)$$

Candidate solutions with α closer to 1 are more liable to be selected as the final solution; according to (27), the network and the DSO will be protected against losing a higher portion of the WT generation. The higher value of α̂ corresponds to the lower value of the WT generation (27) and a higher value of CI. Because of the IGDT constraint (34), candidate solutions with α closer to 1 may not be the final solution. Therefore, the only obstacle to achieving values is the limitation provided by the IGDT. Placing the sentence related to the optimization of the HPs consumption in the OF and trying to reduce their consumption is an attempt to reduce the CI and achieve the PSO to populations with α closer to 1.

K. RS strategy

Candidate solutions with $\check{\alpha}$ closer to 0 are more liable to be selected as the final solution; according to (28), the amount of improvement desired by the DSO will occur for a lower increase in the WT generation. Therefore, the decision-maker can be more hopeful of realizing his optimism about the WT generation increase and the improvement defined in the CI. Reducing the consumption of HPs can have the same effect as increasing the generation of the WT on the CI. Therefore, the desired improvement will be achieved with a lower increase in WT generation.

IV. Simulation results and discussion

In section *A* and *B* conservative and opportunistic approaches have been taken into consideration, respectively. For every single case, the outputs are compared for two scenarios:

• **Scenario I (user-defined)**. Occupants' pre-defined favorite temperature boundary is utilized for HPs consumption determination. The temperature is assumed to be 28 ℃ for winter and 18 ℃ for summer. Based on the typical wear of occupants in winter it is assumed that occupants intrinsically introduce temperatures which are equal to PMV +2 for winter and -2 for summer (Table.1).

• **Scenario II (DSO-defined)**. In this scenario which has been proposed by this paper, instead of using occupants' personal view of the suitable temperature range (which is the most common way of HPs DRPs participation), ASHRAE55

is exploited to find the real thermal needs and the appropriate boundary for occupants. Consequently, the utmost HPs degree of flexibility will be achievable in DRPs.

A. Conservative approach

The first group of simulations are performed in a case in

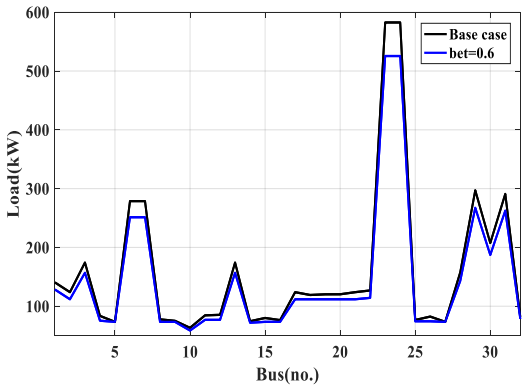

Fig.10. Scenario I HPs consumption alteration versus the base case.

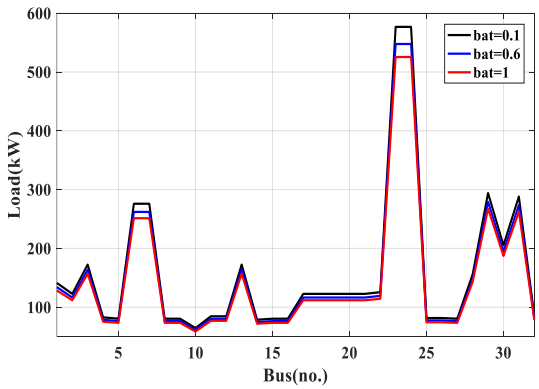

Fig.11. Scenario I HPs consumption alteration versus β.

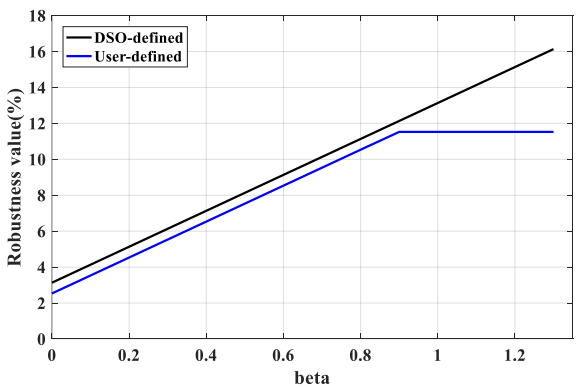

Fig.12. Radius of uncertainty.

which underestimation of the wind forecast is of interest. Thus, the WT will generate less than what is expected (27). A 'base case study' is considered in which no uncertainty exists in the WT power generation. The results of HPs consumption optimization by PSO can be seen in Fig.10.

As can be seen, the loads consumption related to a specific level of critical congestion index (β=0.6) is less than the base case. DSO has decreased the loads opportunity for increasing $\alpha\hat{}$ to a higher value. As the β value rises, the power consumption has been set to lower values (Fig.11), and consequently the value of $\alpha\hat{}$ will be raised (Fig.12).

Contrary to [28] in which a fixed predefined value of load flexibility is assigned to a bus with the most influence on

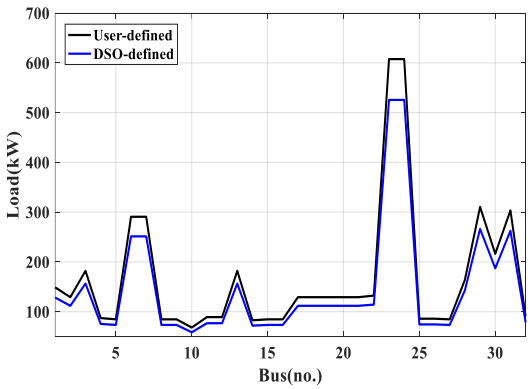

Fig.13. Scenario I & scenario II HPs consumption alteration for β=0.6

the OF, in this work, a more realistic situation is taken into consideration for HPs flexibility. Accordingly, HPs are distributed all over a practical distribution system; therefore, HPs in each bus are considered to provide flexibility for uncertainty management. Moreover, HPs in each bus are considered to offer a different level of flexibility in a way that buses with higher penetration of HPs offer higher levels of flexibility; therefore, without violating the OTC, peak shaving has been performed by β increment and the proposed operating point (set of decision variables) would be more attractive for the DSO to be selected.

a. Scenarios comparison from uncertainty management point of view

Two proposed scenarios have approximately the same reaction to β increment; but, for a definite value of β, scenario II determines a lower consumption for HPs (Fig.13). Fig.13 depicts the results for β=0.6 but the same results can be obtained for other values of β. Fig.12 compares $\alpha\hat{}$ for both scenarios. In fact, higher values of α and a wider range of possible increase for β, are defined by Scenario II ($0.1\leq \beta\leq 0.9$ for the scenario I and $0.1\leq \beta\leq 1.4$ for scenario I). For β values higher than 0.9, HPs consumption in scenario I remain constant (PHPs=Pmin or Pmax in Appendix A). It means HPs' consumption will no longer be the decision variable or be effective in uncertainty management. Higher values for β in scenario II mean more effective usage of HPs in uncertainty regulation. Therefore, from an uncertainty management point of view, scenario II would lead to higher levels of wind forecast underestimation (29) and more acceptable results.

b. WT power reduction capability

In the conservative approach, the realized values of WT power generation are lower than the forecasted ones. For a specific value of ΛC 'dispatchable DG output' refers to the minimum value of WT power generation which can be accommodated by the network. Therefore, in the proposed method, wider WT power generation variations are allowed which are more appropriate from a conservative approach perspective (Fig.14).

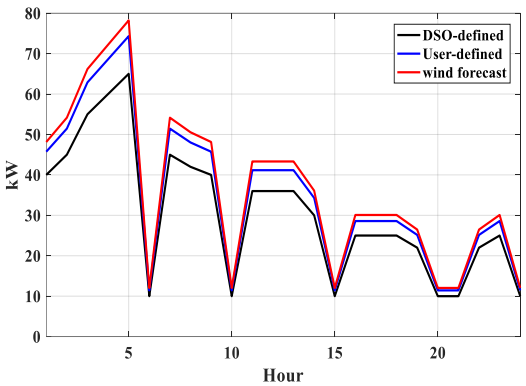

Fig.14. Scenarios WT manageable WT power generation with critical limit ΛC=0.7

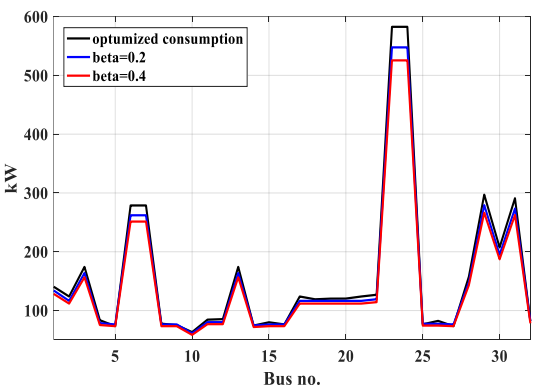

Fig.15. Scenario I HPs consumption vs. β increment (opportunistic approach).

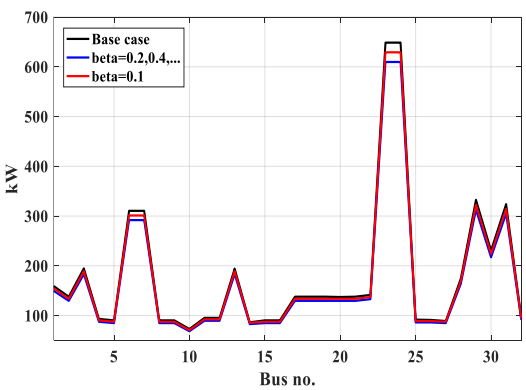

Fig.16.Scenario II HPs consumption vs. β increment (opportunistic approach).

B. *Opportunistic approach*

In the test system, if the wind power goes higher than the predicted value, then the congestion index will decrease. In the proposed scenarios, higher values of β are accompanied by lower values of HPs consumption (Fig.15 and Fig.16). According to (30) increasing the β value leads to CI index improvement. Moreover, in comparison with the conservative approach, β could not grow higher than 0.4 (40% improvement in the OF). This is

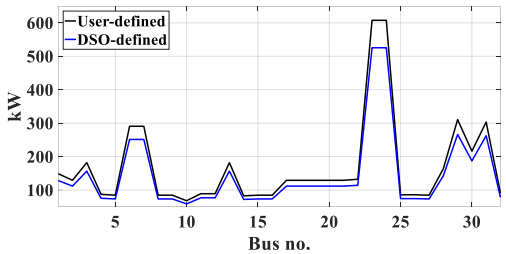

Fig.17. Scenario I & scenario II HPs consumption (β=0.6, opportunistic approach)

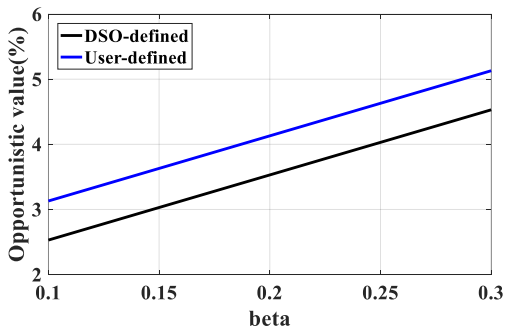

Fig.18. Scenario I scenario II radius of uncertainty.

because of the fact that the WT generation increment could only provide a limited improvement and would never cause the opportunistic congestion index to lower values.

a. Scenarios comparison from uncertainty management point of view

Fig.17 and Fig.18 compare HPs consumption and radius of uncertainty for both scenarios, respectively. Scenario II offers lower values for HPs consumption and $\hat{\alpha}$. Therefore, from the uncertainty management point of view, scenario II would lead to more acceptable results because, with lower HPs consumption, a lower wind power generation increment is required to produce the same enhancement in the CI parameter.

b. WT power generation for opportunistic scenario

For a specific value of ΛO, "opportunistic WT power generation" refers to the minimum value of WT power generation increment which is needed to meet the DSO predefined congestion index while all constraints are met. As can be seen in Fig.19, the proposed method assigns lower values for opportunistic WT power generation which are more desirable.

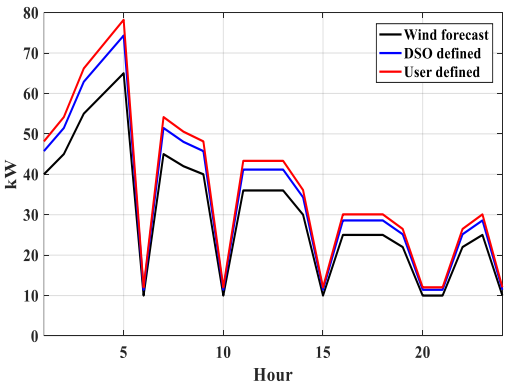

Fig.19. Scenarios WT opportunistic WT power generation with opportunistic limit Λ_O=0.1.

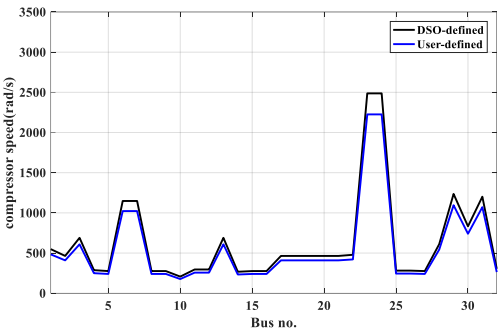

Fig.20. Scenario I and scenario II compressor speed

C. Technical and operational comparison

To show the technical superiority of scenario II, a number of parameters that are effective in the operation of equipment and network have been examined for a conservative approach.

a. Compressor speed

As it was stated earlier, A VFD which is driven by DLC signals controls the compressor speed. So, power consumption of HPs is controlled by the speed adjustment. Lower VSHPs power consumption in scenario II means that the VFD drives compressor at lower speed which reduces the wear in the mechanical components. Fig.20 compares compressor speed variations between two scenarios.

b. Compressor Coefficient of Performance

As was stated in section 2.4, COP can be calculated by (35).

$$COP = \frac{Q_{hp}}{P_m} \tag{35}$$

The larger the COP, means that a fixed amount of Pm produce higher thermal energy. In other words, less mechanical power is required to produce a certain amount of thermal energy. Therefore, higher COP, higher efficiency, lower energy (power) consumption and thus lower operating costs are the results of the proposed method (Fig.21).

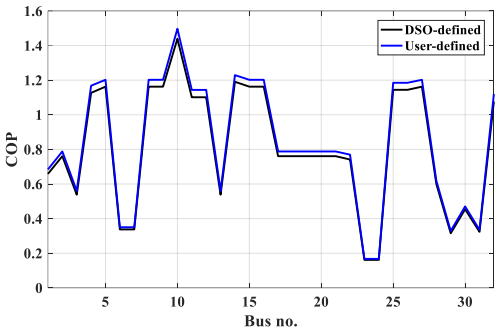

Fig.21. Scenario I & scenario II COP.

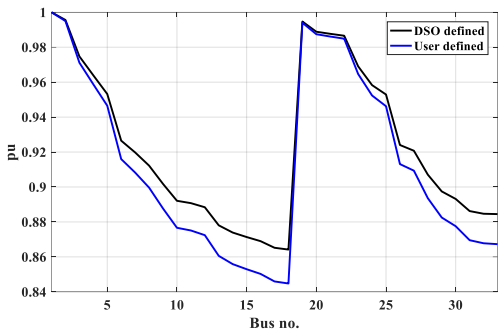

Fig.22. Scenario I and scenario II voltage profile.

c. Voltage profile

For β=0.1, the voltage profiles are examined for two scenarios. In the proposed method, due to lower HPs consumption, the voltage profile is improved across the network. As can be seen in Fig.22, it is obvious that buses 13-18 and 29-33 have the lowest voltage magnitude.

D. PSO and APT-FPSO results comparison

Applying the APT-FPSO optimization method to both risk-seeker and risk-averse strategies can improve some results. In terms of radius of uncertainty, this optimization method will produce the same results in both strategies. But the amount of consumption in the network will be reduced to an acceptable level due to the use of the APT-FPSO method. In the following, these two optimization methods will be compared for two risk-seeker and risk-averse strategies for scenario II.

a. Risk-averse strategy

In Fig.23, the test system power consumption is compared for β=0.2. Although the APT-FPSO strategy has slightly increased the consumption in some buses, in total, by using this method the amount of consumption in the entire network has decreased by 176 kW. This amount is 20 kilowatts more than the typical consumption in bus bar No. 32 of the IEEE 33-bus network.

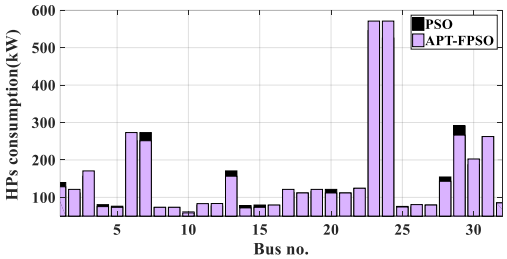

Fig. 23. PSO and APT-FPSO HPs consumption for RA strategy.

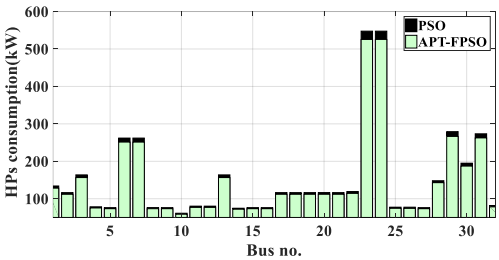

Fig.24. PSO and APT-FPSO HPs consumption for RS strategy.

b. Risk-seeker strategy

In Fig.24, the amount of network power consumption per bus is compared for b=0.2 and using two optimization methods. The APT-FPSO strategy has reduced the consumption in all buses and, the total amount of consumption reduction is 200 kilowatts, which is equivalent to the typical consumption in bus No. 33 of the IEEE 33-bus network.

V. Conclusion

To simultaneously achieve two main aims, a framework based on the ASHRAE55 standard for determining the optimal flexibility of HPs in DRPs has been proposed. To achieve the first goal means guaranteeing the OTC, a new method to control the consumption of HPs was presented. In the first step, the ASHRAE55 standard determines the temperature ranges in which the OTC is assured during the day. Then, using the electro-thermal network of the experimental room at MIT, the boundary of thermal energy required to stabilize the room temperature in the abovementioned ranges and the corresponding HPs power consumption boundaries were determined. The results of using this method were compared with the common one in which the temperature of the building is adjusted within the predetermined limits by the residents. The method has been proposed by this work reduces the consumption of HPs by an average of 13%. To achieve the second goal means managing the uncertainty of the WT, The DSO handles this uncertainty by controlling the power consumption of HPs. The effectiveness of two methods of controlling the consumption of HPs in managing uncertainty is compared using two risk-averse and risk-seeker strategies provided by the IGDT. Using the proposed method, in the first strategy, the radius of uncertainty increases by an average of 6%, and in the second strategy, it decreases by an average of 5.5%. The proposed method results are also more acceptable for network voltage profile and compressor mechanical wear.

A. Future works

• Uncertainty management using IGDT by coordinated operation of energy storage and HPs while considering OTC as a constraint can be an attractive topic for future research.

• To further convince the DSO and HPs owners to adopt the proposed scenario, the environmental and economic objectives could be considered in the optimization problem which can be considered as future work.

• To determine a complete framework for HPs participation in DRPs using classical and fuzzy approaches to find the superior one is also an attractive topic that can be investigated in future work.

REFERENCES

[1] The Paris Agreement [Online]. https://unfccc.int/process-and-meetings/the-paris-agreement/the-paris-agreement.

[2] Lingxi, Z., Chapman, N., et al.:' Exploiting electric heat pump flexibility for renewable generation matching'. Int. Conf. IEEE Manchester Power Tech, Manchester, UK, June 2017; pp.1-6. lingxi.zhang@manchester.ac.uk

[3] Residential Energy Consumption Survey (RECS) [Online].https://www.eia.gov/consumption/residential/reports/2015/overview

[4] Baldib, S., Korkasa, C., et al.: 'Automating occupant-building interaction via smart zoning of thermostatic loads A switched self-tuning approach', Appl. Energy,vol. 231, pp. 1246–1258, 2018

[5] Korkas, C., Baldi S., et al.:' Occupancy-based demand response and thermal comfort optimization in micro grids with renewable energy sources and energy storage', Appl. Energy, vol. 163, pp. 93–104, 2016

[6] Anand, P., Sekhar,C., Cheong D., et al.:' Occupancy-based zone-level VAV system control implications on thermal comfort, ventilation, indoor air quality and building energy efficiency', Appl. Energy ,vol. 204, pp. 1–14, 2019

[7] Diekerh, M., Peterssen F.:' Hierarchical distributed robust optimization for demand Response Services', IEEE Trans. smart grid ,vol. 9, pp. 6018-6029,2018.

[8] Angelis,F., Boaro, M., et al.:' Optimal home energy management under dynamic electrical and thermal constraints', IEEE Trans. Industr. Inform., 2013, 9, (3), pp.1518-1527 vol. 9, pp. 1518-1527, 2013.

[9] Marco,Pau., Jochem, C.:' Impact of customers flexibility in heat pumps scheduling for demand side management'. IEEE.Int. Conf. on Environment and Electrical Engineering, Milan, Italy, pp.1-6, 2017.

[10] Khatibi, M., Bendtsen, J., et al.:' Exploiting Power-to-Heat Assets in District Heating Networks to Regulate Electric Power Network'. IEEE Trans. Smart Grid, vol. 12, no. 3, pp.2048-2059, 2021.

[11] Csetvei, Z., Ostergaard, J., Nyeng P.:' Controlling price responsive heat pumps for overload elimination in distribution systems', 2nd IEEE PES Int. Conf. and exhibition on Innovative Smart Grid Technologies,

Manchester, UK, Dec 2011, pp.1-8 vol. ---, no. ---, pp.1-8, 2011.
[12] Mendaza, C., Szczesny, I., et al.:'Demand Response Control in Low Voltage Grids for Technical and Commercial Aggregation Services', IEEE Trans. Smart Grid vol. 7, no. 6, pp.2771-2780, 2016.
[13] Pedersen, T., Nielsen, K. Andersen, P:' Maximizing Storage Flexibility in an Aggregated Heat Pump Portfolio', IEEE Conf. on Control Applications, Juan Les Antibes, France, pp.1-6, 2014.
[14] Ponci,F., M., Monti, A.:' Optimal scheduling of heat pumps for power peak shaving and customers thermal comfort', Int. Conf. EEEIC/ I& CPS Europe, Palermo, Italy,pp.23-34, 2018.
[15] Kim, Y., Norford, L.K., Kirtley J.L.:' Modeling and analysis of a variable speed heat pump for frequency regulation through direct load control', IEEE Trans. Power Syst.,vol. 30, no.1, pp.397-408,2015.
[16] Kazemi-Razi M., Abyaneh H. a, Nafisi H. a, Ali Z. b, Marzband M.:' Enhancement of flexibility in multi-energy microgrids considering voltage and congestion improvement: Robust thermal comfort against reserve calls', sustainable cities and society, vol.74, pp.1-13, 2021.
[17] Jadidoleslam M., and Ghaseminezhad M.:' Reliability-based probabilistic wind power planning considering correlation of load and wind', Industrial electronics control and optimization,vol.5, no. 4, pp.305-315, 2022.
[18] Malekijavan A., Aslinezhad M., and Zaferani H.' Reliability-Based Operation in Energy Hubs with Several Energy Networks', Industrial electronics control and optimization, vol.4, no. 4, pp.433-444, 2021.
[19] Shirmardi A., Joorabian M., and Barati H.' Green Micro-Grid Operation Constrained to Reliability and Flexibility Indices in the Presence of Distributed Generations and Energy Storage Systems', Industrial electronics control and optimization, 2021,4, (4), pp. 397-407. vol. 4, no. 4, pp.397-407, 2021.
[20] Vosoogh M., Rashidinejad M., Abdollahi A., and Ghaseminezhad M.' Efficient networked microgrid management considering plug-in electric vehicles and storage units', Industrial electronics control and optimization,vol. 4, no. 2, pp.245-255,2021.
[21] Haiyan X., Yuqing C. et al.:' A new multi-timescale optimal scheduling model considering wind power uncertainty and demand response', International journal of electrical power and energy systems, vol. 147, pp.1-11, 2023.
[22] Linjun Z, Jiazhu X et al.:' Day-ahead interval optimization for CCHP system considering uncertainty of wind power and PV', International journal of electrical power and energy systems, 2022, 138: pp.1-9. vol.138,pp.1-9, 2022.
[23] Ding, Guo, Qiannan, and Jermsittiparsert, Lekvan et al.:' Economic and environmental assessment of multi-energy microgrids under a hybrid optimization technique', sustainable cities and society,vol. 65, pp.1-12, 2021.
[24] Coelho A. Neyestani N. et al.:' Wind variability mitigation using multi-energy systems', Electrical power and energy system, vol. 118, no. pp.1-9, 2020.
[25] Correa C.A, Michiorri A., Kariniotakis G.:' Optimal Participation of Residential Aggregators in Energy and Local Flexibility Markets', IEEE Trans. on smart grid, vol. 11, no. 2, pp.1644-1656, 2020.
[26] Yakov Ben-Haim, "Information Gap Decision Theory," The Technion Haifa, Israel, Feb, 2006
[27] A. Dolatabadi, M. Jadidbonab and B. Mohammadi-ivatloo, "short-term scheduling strategy for wind-based energy hub: a hybrid stochastic/IGDT approach," IEEE Trans. Sustainable Energy, vol. 10, no. 1, pp. 438–448, 2019.
[28] C. Murphy,Soroudi.A and A.Keane, "Information Gap Decision Theory-based congestion and voltage management in the Presence of uncertain wind power," IEEE Trans. Sustainable Energy, vol. 7, no. 2, pp. 841–849, Nov. 2015.
[29] P.Li, Z.Wang, et al. "Two-stage optimal operation of integrated energy system considering multiple uncertainties and integrated demand response," Energy, vol. 225, pp. 1–12, Jun. 2021.
[30] A. Kazemdehdashti , M. Mohammadi , A.R. Seifi , M. Rastegar. "Stochastic energy management in multi-carrier residential energy systems," Energy, vol. 225, pp. 1–12, May. 2020.
[31] X.Jina,b, J.Wua,Y.Mu, et al. "Hierarchical microgrid energy management in an office building," Appl.Energy, vol. 208, pp. 480–494, Oct. 2017.
[32] X.Jina,b, J.Wua,Y.Mu, et al. "Resilient configuration approach of integrated community energy system considering integrated demand response under uncertainty," IEEE Access, vol. 7, pp. 87513 - 87533, Jun. 2019.
[33] I. Ballarini, S.P. Corgnati, V. Corrado,' Use of reference buildings to assess the energy saving potentials of the residential building stock: The experience of TABULA project', Energy Policy 68 vol. 68, pp.273-284, 2014.
[34] Zakula T, 'Model predictive control for energy efficient cooling and dehumidification,' Dept. Arch Massachusetts Inst. Technol, Massachusetts, Ph.D. thesis (2013).
[35] Kim Y, Norford LK, Kirtley JL, 'Modeling and analysis of a variable speed heat pump for frequency regulation through direct load control,' IEEE Trans Power, vol. 30,no.1, pp.397–408, 2015.
[36] Evelyn Sperber, Ulrich Frey, Valentin Bertsch,' Reduced-order models for assessing demand response with heat pumps -insights from the German energy system', Energy & Buildings,vol. 223-,pp.1-18, May 2020.
[37] ANSI/ASHRAE Standard 55-2004: 2004.
[38] 2020 ASHRAE Handbook—HVAC Systems and Equipment',https://ashrae.org/technicalresources/ASHRAE-handbook/description-2020.
[39] ISIRI 14384 1st. Edition: 2011
[40] Zhongping Lina, Shiming Deng,' A study on the thermal comfort in sleeping environments in the subtropics—Measuring the total insulation values for the bedding', Building and Environment, 2008,43, pp.905-916. vol.43, pp.905-916, 2008.
[41] Iran's Provinces annual average of total monthly solar radiation[Online].https://www.researchgate.net/figure/Irans-Provinces-annual-average-of-total-monthly-solar-radiation
[42]Climatein Tehran [Online]. https://www.worlddata.info/asia.
[43] Line data of the IEEE 33-bus radial distribution system [Online]. https://www.researchgate.net/figure/Line-data-of-the-IEEE-33-bus-radial-distribution-system.
[44] Koohi, Iraj:' Optimizing Particle Swarm Optimization algorithm', IEEE 27th Canadian Conf. Electrical and Computer Engineering, (CCECE), Toronto, Canada, May 2014.
[45] N. Bakhshinezhad, S.A. Mir Mohammad Sadeghi, et al.:' Adaptive particularly tunable fuzzy particle swarm optimization algorithm', Iranian Journal of Fuzzy Systems, vol. 17, no. 1, pp. 65–75, 2020. vol.17, no. 1, pp. 65-75, 2020.
[46] P. Melin, "Optimal design of fuzzy classification systems using PSO with dynamic parameter adaptation through fuzzy logic", Expert Systems with Applications,vol. 40,

no.8-, pp.3196-3206,2013.
[47] A. P. Engelbrecht, Fundamentals of computational swarm intelligence, John Wiley & Sons, 2005.

Mohammadmehdi Sedaghatzadeh was born in Iran, in 1980. He is a PhD student in power engineering at Department of Electrical and Electronics Engineering, Shiraz University of Technology, Shiraz, Iran. He received his M.S. degree in Electrical Power Engineering from the Islamic Azad University, Saveh, Iran, in 2007. He received the B.S. degree in electronics engineering from Islamic Azad University, Tehran, in 2002. He is an expert in electrical engineering in National Iranian South Oil Company. His research interests include smart grid, Micro-grid demand side management, and renewable generation.

Mohsen Gitizadeh was born in Iran, in February 1976. He received the B.S. degree in electrical engineering from Shiraz University, Shiraz, Iran, in 1999, and the M.S. and Ph.D. degrees from the Iran University of Science and Technology, in 2001 and 2009, respectively. He is currently a Professor with the Department of Electrical and Electronics Engineering, Shiraz University of Technology, Shiraz. His current research interests include power system operation and control, voltage stability, optimization, demand side management, and FACTS devices.

Saeed Hasanvand received his BSc. degree from Shahid Chamran University of Ahvaz, Iran, in 2009, the MSc. degree from University of Isfahan, Iran, in 2012, and the PhD. from Shiraz University of Technology, Iran, in 2017. He is currently an assistant professor in electrical engineering at Firouzabad Institute of Higher Education. His research interests include power system stability and optimization, micro-grids, renewable energies, FACTS devices, and power system reliability.

Appendix A: IGDT-based optimization algorithm